

TENSILE DEFORMATION OF POLYMER NANOCOMPOSITES: HYDRODYNAMIC
EFFECT AND MECHANICAL REINFORCEMENT

By

Ruikun Sun

A DISSERTATION

Submitted to
Michigan State University
in partial fulfillment of the requirements
for the degree of

Chemical Engineering – Doctor of Philosophy

2022

ABSTRACT

TENSILE DEFORMATION OF POLYMER NANOCOMPOSITES: HYDRODYNAMIC EFFECT AND MECHANICAL REINFORCEMENT

By

Ruikun Sun

Polymer nanocomposites (PNCs) are important functional materials with various applications because of their superior nanoparticle-reinforced properties. Among these enhanced macroscopic properties, mechanical reinforcement in PNCs is the most intriguing and among the first to be considered in applications from transportation, packaging to gas separation. However, understanding the mechanical reinforcement of PNCs remains a challenging task, especially in the large deformation regime where nonlinear effects emerge.

This dissertation focuses on PNCs with well-dispersed spherical nanoparticles in the dilute and semi-dilute limit to investigate the mechanical reinforcement under large deformation at various Weissenberg number, $Wi = \dot{\epsilon}\tau_d$ with $\dot{\epsilon}$ being the Hencky strain rate and τ_d the relaxation time of the polymer. At $Wi \ll 1$, the nanoscale motion of nanoparticles first follows the macroscopic deformation. Beyond a critical elongation ratio defined by the interparticle spacing, the hydrodynamic interaction among nanoparticles leads to a strong deviation of the local spatial rearrangement of nanoparticles from the macroscopic deformation field. Further deformation leads to a deformation-induced nanoparticle network. More importantly, the elastic deformation of the network provides a strong enhancement to the mechanical strength of PNCs at large deformation.

As Wi increases, strong microstructure rearrangement of nanoparticles is observed. Remarkably, the nanoparticle rearrangement does not affect the entanglement dynamics in the leading order and does not correlate with the macroscopic stress of the PNCs. These observations

indicate that the deformation of matrix polymer plays a dominant role in the macroscopic stress of PNCs.

To decouple the stress contributions from the matrix polymer and the nanoparticles, we further perform small-angle neutron scattering experiments that capture only the structure and dynamics of polymer matrices. Interestingly, the neutron experiments show that the magnitudes of polymer anisotropy in the PNC and the neat polymer are identical under the same deformation. Moreover, the stress relaxation of PNCs follows the time evolution of the structural anisotropy of the deformed matrix polymer. Similar phenomena are also observed for PNCs with nanoparticle aggregates and high nanoparticle loadings. These observations point to the absence of strain amplification or molecular overstraining in deformed PNCs and suggest the hydrodynamic effect as the leading molecular origin of the high mechanical strength of PNCs.

To further quantify the molecular origin associated with the high polymer matrix contribution to the mechanical reinforcement, we carry out nonlinear rheology measurements for PNCs with different polymer molecular weights and nanoparticle loadings. The nonlinear rheological stress-strain curves of all these PNCs, if normalized by a constant dependent on PNC composition, are found to overlap with each other up to the stress overshoot point. This constant is directly correlated with the bulk polymer relaxation, instead of the interfacial polymers. These observations point to that the mechanical reinforcement of PNCs is controlled by the slowing down of the chain relaxation dynamics.

Copyright by
RUIKUN SUN
2022

DEDICATED TO MY PARENTS AND GRANDPA

ACKNOWLEDGMENTS

My time at Michigan State University has so far been the most challenging period of my life. Without the help and support of many individuals, I cannot be where I am today. First, I would like to thank my academic advisor, Dr. Shiwang Cheng. I feel very fortunate to become one of his first students, which allowed me to help him establish the laboratory and explore new fields. In research, he always keeps a high standard and constantly challenges my critical thinking. He pushes me to be the best researcher I can be. In life, he treats his students like his own children and truly cares for our personal development. I appreciate Dr. Cheng's teaching and caring over the years, and the time in his group will be one of the most memorable times of my life.

I would like to thank my doctoral committee. I would like to thank Dr. Andre Lee for his valuable suggestions and advice in research. I genuinely appreciate his critical questions and analytical thinking during each group meeting. I learn a lot during this process. I also appreciate Dr. Lee's generosity in letting me use his instruments. I would like to thank Dr. Krishnamurthy Jayaraman for his teaching and his valuable insights on my dissertation. I learned a lot from his classes on polymer composites and rheology, closely related to my research. I would like to thank Dr. Ramani Narayan for his insights from the engineering and industrial perspectives. He helps me see a bigger picture and widen my vision. I would like to thank Dr. Tong Gao for his teaching and suggestions and questions on my dissertation, helping me understand the research problems from different perspectives.

I also would like to thank Dr. Robert Ferrier for giving me full access to his laboratory and his instruments and the help from his students: Niloofar Safaie, Gouree Kumbhar, Shaylynn

Crum, and Mayson Whipple. I also would like to thank my colleagues, Jie Yang, Matthew Melton, Aditya Patil, Tyler Johnson, David Vogelsang, Yuelin Wu, Yang Lu, Shalin Patil, and Danielle DeJonge, for providing valuable insights from the discussions and the questions. I would like to thank Mike Rich and Robert Selden, Mike Koschmider, and Brian Wright for their awesome technical support. I would like to thank the ChEMS office staff, Tiffany Owen, Donna Fernandez, Brad Tobin, Jennifer Keddle, Heather Dainton, and Jessica Gallegos, for helping me with various issues from administration to conference travel. I would like to thank my friends Chauncey Splichal, Moh Alhaj, and Affan Malik for our adventures outside of the research. I would like to thank my advisor and peers from my undergraduate college Dr. Michael Senra, Max Ma, Sean McSherry, and Rachel Elias, for our good times in Ann Arbor.

Finally, I would like to express my love and gratitude to my family and friends in my hometown China. My grandpa influenced and motivated me to pursue science ever since I was a child. He would be so proud of me for what I have accomplished. My parents have been generously supporting me in all of my endeavors with their selfless love and care. I love you, mom, and dad. I feel lucky to have my fiancée with me in Michigan. She is such an intelligent human being and helped me in many aspects of life and research. My best friends, Shiqiao, Xingbo, and Xingyuan, have always provided me with support and encouragement. I genuinely appreciate all the things my family and friends have done for me.

TABLE OF CONTENTS

LIST OF TABLES	x
LIST OF FIGURES	xi
CHAPTER 1 A REVIEW OF MECHANICAL REINFORCEMENT IN POLYMER NANOCOMPOSITE MELTS	1
1.1 Background and Motivations	1
1.2 Experimental Techniques	4
1.2.1 Rheological Methods.....	4
1.2.2 Small-angle X-ray Scattering	8
1.2.3 Small-angle Neutron Scattering and Spherical Harmonic Expansion.....	10
1.2.3.1 Zero Average Contrast in Polymer Nanocomposites.....	11
1.2.3.2 Spherical Harmonic Expansion Analysis of Deformed Polymers	11
1.3 Hydrodynamic Effect of Nanoparticles and Strain Amplification.....	13
1.4 Polymer Nanocomposites under Uniaxial Extension.....	15
1.5 Research Objectives	18
1.6 Outline of Thesis Chapters	18
CHAPTER 2 DEFORMATION INDUCED NANOPARTICLE NETWORK IN POLYMER NANOCOMPOSITES UNDER LARGE DEFORMATION	21
2.1 Introduction	21
2.2 Materials and Methods	21
2.3 Results and Discussion	24
2.3.1 Small-angle X-ray Scattering and Linear Rheology	24
2.3.2 Nonmonotonic Strain Rate Dependence on the Strain Hardening of Polymer Nanocomposites	27
2.3.3 Double Stress Overshoots in Stress-Strain Curves.....	31
2.3.4 The Origin of Second Stress Overshoot	33
2.4 Conclusions	38
CHAPTER 3 ROLES OF MICROSTRUCTURE REARRANGEMENT TO THE MECHANICAL REINFORCEMENT OF POLYMER NANOCOMPOSITES UNDER LARGE DEFORMATION	40
3.1 Introduction	40
3.2 Materials and Methods	40
3.3 Results and Discussion.....	41
3.3.1 Linear Rheology and Small-angle X-ray Scattering (SAXS).....	41
3.3.2 One-dimensional SAXS Pattern Analysis	45
3.3.3 Two-dimensional SAXS Pattern Analysis	47
3.3.4 The Correlation between Nanoparticle Microstructure Rearrangement and the Mechanical Reinforcement in PNCs	48
3.3.5 The Entanglement Network of the Matrix Polymer	49
3.4 Conclusions	51

CHAPTER 4 MOLECULAR ORIGIN OF MECHANICAL REINFORCEMENT IN POLYMER NANOCOMPOSITES.....	52
4.1 Introduction	52
4.2 Materials and Methods	53
4.3 Results and Discussion	57
4.3.1 Poly (methyl methacrylate)/SiO ₂ with Well-dispersed Nanoparticles	57
4.3.1.1 Zero Contrast Matching	57
4.3.1.2 Rheology and Small-angle X-ray Scattering	58
4.3.1.3 Polymer Anisotropy under Uniaxial Extension	59
4.3.1.4 Polymer Anisotropy under Stress Relaxation	63
4.3.1.5 Hydrodynamic Effect in Polymer Nanocomposites	65
4.3.2 Polystyrene/SiO ₂ with Aggregated Nanoparticles.....	67
4.3.2.1 Zero Contrast Matching	67
4.3.2.2 Small-angle X-ray Scattering, Linear Rheology and Stress Relaxation	69
4.3.2.3 Neutron Scattering of Deformed Polymer Nanocomposites	72
4.3.2.4 The Molecular Mechanism of the High Stress of PNCs at Large Deformation ...	73
4.4 Conclusions	77
 CHAPTER 5 THE ROLE OF INTERFACIAL POLYMERS FOR MECHANICAL REINFORCEMENT OF POLYMER NANOCOMPOSITES AT LARGE DEFORMATION.....	 78
5.1 Introduction	78
5.2 Materials and Methods	78
5.3 Results and Discussion.....	79
5.3.1 Small-angle X-ray Scattering	79
5.3.2 Small-amplitude Oscillatory Shear.....	80
5.3.3 Uniaxial Extension	83
5.3.4 Engineering Stress Overshoot	85
5.3.5 Quantitative Understanding of Stress-strain curves with the Parameter $a(\varphi_{NP})$	87
5.4 Conclusions	90
 CHAPTER 6 CONCLUSIONS AND FUTURE OUTLOOK.....	 91
6.1 Conclusions	91
6.2 Future Outlook	92
 BIBLIOGRAPHY	 96

LIST OF TABLES

Table 3.1 Material properties and inter-particle-to particle distances.....	41
Table 4.1 Characteristics of polymers used in the study.....	53
Table 5.1 Polymer and nanoparticle information of PNC samples.....	79

LIST OF FIGURES

Figure 1.1 A schematic of cone and plate geometry (grey regions) of a rheometer filled with a sample (the blue region with red lines).....	5
Figure 1.2 The master curve of monodisperse Poly(2-vinylpyridine) (P2VP) with weight-average molecular weight of 100 kg/mol constructed by the time-temperature superposition principle. Four regions are notified: glassy, transition, rubbery plateau, and terminal region ³⁷	5
Figure 1.3 A picture of Sentmanat Extension Rheometer (SER3) mounted on an Anton Paar MCR302 Rheometer	6
Figure 1.4 Schematic of a cuboid sample before (left) and after (right) uniaxial extension in a cartesian coordinate with length L, width W, and height H. The subscript of 0 refers to the initial dimensions of the sample. Red arrows indicate the stretching direction.	7
Figure 1.5 (a) stress-strain curves of a PNC and a neat polymer and (b) elongational viscosity responses of a PNC and a neat polymer under uniaxial extension. η_0 is the zero-shear viscosity. .	8
Figure 1.6 An experimental setup for x-ray scattering	9
Figure 1.7 Demonstration of spherical harmonic expansion of a 2D SANS spectrum (Adapted from Ref. 34. Copyright 2017, Physical Review X).....	13
Figure 1.8 Filler immersed in a rubber matrix	14
Figure 2.1 Small-angle x-ray scattering of PNCs. The solid lines are the form factors, $P(Q)$, of the two types of nanoparticles (NPs). The inset shows the $S(Q)$ of the PNCs with the primary peak position Q_c	25
Figure 2.2 TEM images of P2VPR12-5v% (left) and P2VP9-8v% (right)	25
Figure 2.3 (a) The storage spectra, $G'(\omega)$ (mainframe) and the loss spectra $G''(\omega)$ (inset) $G'(\omega) \sim \omega^2$ and the $G''(\omega) \sim \omega^1$ at the low-frequency region are observed in all PNCs. (b) Shift factors a_T of the pristine P2VP and PNCs.....	26
Figure 2.4 The τ_a/τ_d of the PNCs (symbols) and an estimate of the hydrodynamic effect $H(\phi_{NP}) = 1 + 2.5\phi_{NP}$	27
Figure 2.5 Transient viscosity $\eta_E^+(t, \epsilon)$ vs t of (a) the pristine P2VP, (b) the P2VPR12-4%, (c) the P2VPR12-5%, (d) the P2VPR12-7% and (e) the P2VPR9-8% under uniaxial extension. The solid olive lines are the $3 \eta^*(1/\omega) $ vs $1/\omega$ from linear viscoelastic measurements. The number labeling are the corresponding apparent Weissenberg numbers (Wi_a).....	28

Figure 2.6 The strain hardening index $\beta_{SH}(t, \dot{\epsilon}) = \eta_E^+(t, \dot{\epsilon})/3|\eta^*(1/\omega)|$ of (a) the pristine P2VP, (b) the P2VPR12-4%, (c) the P2VPR12-5%, (d) the P2VPR12-7% and (e) the P2VPR9-8%, showing non-monotonic strain rate dependence. The purple dashed lines are a simple connection of the peak position of the $\beta_{SH}(t, \dot{\epsilon})$ at each strain rate to guide the eyes. The pink dashed lines indicate the $\beta_{SH}(t, \dot{\epsilon}) = 1$ line. The number labeling by each curve is the corresponding Wi_a ...30

Figure 2.7 Engineering stress, σ_{egr} , vs elongation ratio, λ , of (a) the pristine P2VP, (b) the P2VPR12-4%, (c) the P2VPR12-5%, (d) the P2VPR12-7% and (e) the P2VPR9-8%. The insets show the uniaxial extension results at $Wi_a > 1.0$. λ_1 and λ_2 correspond to the two stress overshoots of PNCs at $Wi_a < 1.0$. The number labeling by each line is the corresponding Wi_a 31

Figure 2.8 Scaling behaviors of the two stress overshoots: (a) The σ_1^{max} vs Wi_a (mainframe) as well as the $\ln(\lambda_1)$ (open symbols) and $\ln(\lambda_2)$ (filled symbols) vs Wi_a (inset). (b) The σ_2^{max} vs Wi_a (mainframe) and the σ_2^{max}/A_{NP} vs Wi_a (inset) of the PNCs. A_{NP} is the surface area of NPs per unit volume32

Figure 2.9 (a) A sketch of the microstructure rearrangement of PNCs at deformation. At $\lambda < \lambda_0$, the NP network has not yet formed, and the deformation of the bulk polymer matrix controls the mechanics of PNCs. At $\lambda > \lambda_0$, the deformation of the NP network triggers the strain hardening, and the yielding of the NP network leads to the second stress overshoot at $Wi_a < 1.0$. The black NPs are individually dispersed, and the red ones form networks and bear the load. The yellow shell of the NP represents the tightly bounded thin interphase polymer layer. (b) Strain hardening of PNCs of different NP loadings where PNCs with a lower ϕ_{NP} has a higher onset, λ_0 , for the strain hardening. The inset shows the $d_{cc}/(2R_{NP}\lambda_0^{1/2})$ of PNCs with different ϕ_{NP} and R_{NP}35

Figure 2.10 (a) Elongation viscosity of the P2VPR12-7% at $Wi_a = 0.092 \ll 1.0$. The inset presents the SAXS spectra at elongation ratios of $\lambda = 1.0, 2.0, 3.0, 4.0,$ and 5.0 . The z and x directions are the stretching direction and the transverse stretching direction. (b) The normalized scattering intensities of the stretched P2VPR12-7% at $\lambda = 2$ along the stretching (z-direction) direction, $I^z(Q)$ (the blue line), and transverse the stretching direction (x-direction), $I^x(Q)$ (the red line). The black line is the scattering intensity of the isotropic P2VPR12-7%. The dashed olive line represents the form factor of the NP. The inset represents the anisotropic structure factors of the stretched sample, the $S^z(Q)$ (the blue triangles) and the $S^x(Q)$ (the red circles), and the structure factor of the isotropic PNC (the black squares)36

Figure 2.11 (a) The anisotropic structure factors of the PNCs along z (filled symbols) and x (empty symbols) directions. (b) The changes of the characteristic center-to-center distance of NPs along the z (d_{cc}^z) and x (d_{cc}^x) directions. The dashed lines are the predictions of the d_{cc}^z and the d_{cc}^x by assuming ideal affine positional change of NPs. The dotted line represents the $2R_{NP}$ 37

Figure 3.1 (a) Master curves of pure polymer (lines) and PNCs (symbols) constructed from time-temperature superposition principle (TTSP). Inset: Horizontal shift factors for constructing master curves. (b) Loss factor $\tan(\delta) \equiv G''/G'$ for the same samples in (a). Inset: Plateau modulus of PNC G_p^{PNC} normalized by that of pure polymer $G_p^{polymer}$ (squares) plotted against the estimation from Einstein-Smallwood relation $G_p^{PNC}/G_p^{polymer} = 1.0 + 2.5\phi_{NP}$ where ϕ_{NP} is the volume fraction of NPs41

Figure 3.2 Engineering stress σ_{egr} versus elongation ratio λ of (a) P2VPR12-4%, (b) P2VPR12-5%, (c) P2VPR12-7%, (d) P2VPR9-8% at different extension rates $\dot{\epsilon}$ (in s^{-1}). The neat polymer data at the same rates serves as a comparison in grey lines in all plots. The stress magnitude of both P2VP and PNC increases with increasing deformation rates43

Figure 3.3 2-D SAXS patterns for P2VPR12-7% at various deformation conditions. The upper-left image is the pattern for the isotropic PNC. The 4x4 array of images are the patterns for the PNC under four different elongation rate $\dot{\epsilon} = 0.003, 0.06, 0.6, \text{ and } 3 s^{-1}$ and at different elongation ratios $\lambda = 1.5, 3.0, \text{ and } 5.0$. The images in the same row have the same λ and the images in the same column have identical $\dot{\epsilon}$. The left-down image is at deformation condition of $\dot{\epsilon} = 0.6 s^{-1}$ and $\lambda = 11$ 44

Figure 3.4. 1-D SAXS intensity curves in x and z directions at different stages of deformation for (a) extensional rate $\dot{\epsilon} = 0.06s^{-1}$, (b) $\dot{\epsilon} = 0.6s^{-1}$, (c) $\dot{\epsilon} = 3s^{-1}$ of P2VPR12-7%. (d) A summary of the average center-to-center nanoparticle distance in stretching direction (d_{cc}^z) and transverse to stretching direction (d_{cc}^x) at different deformation stages at different $\dot{\epsilon}$. The dash lines with a slope of 1 and 2 are the affine deformation predictions for d_{cc}^z and d_{cc}^x , respectively45

Figure 3.5. Engineering stress ratio between (a) P2VPR12-5% and (b) P2VPR12-7% and neat polymer to quantify the mechanical reinforcement under uniaxial extension. The stress ratio changes with both strain and strain rate49

Figure 3.6 (a) The strain at the engineering stress overshoots for all samples at different rates, where the $\lambda_{max}^{polymer}$ is associated with the polymer disentanglement and λ_{max}^{NP} is related to the yield of the nanoparticle network. (b) The engineering stress overshoot associated with the polymer $\sigma_{max}^{polymer}$ is plotted across different strain rates. A factor is multiplied to each sample to normalize their $\sigma_{max}^{polymer}$ to those of the P2VPR9-8%. A good match has been found at the high-rate regime50

Figure 4.1 Normalized scattering intensity $I(Q)/\phi_{poly}\phi_H\phi_D$ of mixtures of H⁸-PMMA and D⁸-PMMA at different H/D ratios. Here, $\phi_{poly} = 1 - \phi_{NP}$ is the volume fraction of the polymer, and ϕ_H and ϕ_D are the volume fractions of the hydrogenous and deuterated PMMAs, respectively57

Figure 4.2 Comparison of the normalized intensities of PMMA/SiO₂ and pristine PMMA with H/D = 0.59:0.4157

Figure 4.3 (a) Small-angle x-ray scattering spectrum of PMMA/SiO ₂ . Inset: TEM image of the same sample. (b) Linear viscoelastic spectra of PMMA and PMMA/SiO ₂ at 423 K. These master curves are constructed using the time-temperature superposition principle ⁷² . Here, ω is the angular frequency and a_T is the shift factor. Stars: PMMA. Circles: PMMA/SiO ₂ . Inset: loss factor $\tan\delta(\omega) \equiv G''(\omega)/G'(\omega)$	59
Figure 4.4 Stress-strain curves of PMMA and PMMA-SiO ₂ at a constant Hencky strain rate of $\dot{\epsilon} = 0.01 \text{ s}^{-1}$ at T=423 K, along with the SANS spectra taken at stretching ratios of 1.2, 1.5, 1.8, and 2.1. We point out that the stress enhancement at large strains, ca. 23%, is consistent with the hydrodynamic effect of nanoparticles from the Padé approximation.....	60
Figure 4.5 Spherical harmonic expansion coefficients. Here, $S_0^0(Q)$ and $S_2^0(Q)$ are, respectively, the isotropic and leading anisotropic expansion coefficients of the structure factor $S(Q)$. Symbols: PMMA/SiO ₂ . Lines: PMMA.....	61
Figure 4.6 Evolution of engineering stress σ_{eng} of PMMA (lines) and PMMA-SiO ₂ (symbols) during a step uniaxial extension performed with $\dot{\epsilon} = 0.01 \text{ s}^{-1}$ at T=423 K and the subsequent stress relaxation at $\lambda = 1.8$. The time t is normalized by the terminal relaxation time τ of the pristine PMMA. Inset: engineering stress during relaxation.....	63
Figure 4.7 PMMA and PMMA/SiO ₂ exhibit identical scaling behavior for anisotropy relaxation. $S_2^0(Q; 0)$ is the expansion coefficient immediately after the step deformation, whereas $S_2^0(Q; t)$ is the coefficient during the stress relaxation. Inset: spatial dependence of the normalized expansion coefficient $S_2^0(Q; t)/S_2^0(Q; 0)$ during the relaxation.....	64
Figure 4.8 Normalized scattering intensity $I(Q)/\varphi_{pol}\varphi_H\varphi_D$ of mixtures of H ⁸ -PS and D ⁸ -PS at different H/D ratios. Here, $\varphi_{pol} = 1 - \varphi_{NP}$ is the volume fraction of the polymer, and φ_H and φ_D are the volume fractions of the hydrogenous and deuterated PSs, respectively.....	67
Figure 4.9 Polymer fraction normalized intensities of neat polymer and PNCs by SANS measurement.....	68
Figure 4.10 Master curves of neat polymer, PS8.7, PS18 and PS24 with a reference temperature of 120 °C.....	69
Figure 4.11 Stress relaxation curves of neat polymer, PS8.7, PS18 and PS24 at $\lambda = 1.8$ for a relaxation time of 1τ	70
Figure 4.12 Scattering intensities of PS8.7, PS18, and PS24 by small-angle x-ray scattering.....	71
Figure 4.13 X-ray scattering intensities of PS8.7, PS18, and PS24 with isotropic state (iso), and stretched at an elongation ratio of $\lambda = 1.8$ followed with different time after relaxation ($t = 0\tau, 0.1\tau, 1\tau$ where τ is the relaxation time of the neat polymers.....	72
Figure 4.14 The 2D SANS spectra of PS8.7, PS18, and PS24 at different stages of stress relaxation.....	73

Figure 4.15 $-S_2^0(q)$ values of PNCs of different loading at different stages of relaxation: (a) $t_{relax} = 0 \tau$, (b) $t_{relax} = 0.1 \tau$ and (c) $t_{relax} = 1 \tau$	74
Figure 4.16 Normalized $S_2^0(q; t_{relax})/S_2^0(q; 0)$ of neat polymer, PS18 and PS24 at (a) $t_{relax} = 0.1 \tau$ and (b) $t_{relax} = 1.0 \tau$	76
Figure 5.1 The scattering intensity $I(Q)$ normalized by silica volume fraction φ_{NP} of (a) P2VP200k/SiO ₂ and (b) P2VP100k/SiO ₂ and P2VP400k/SiO ₂ samples obtained from small-angle x-ray scattering measurements. The insets show Kratky plots for the representative samples.....	80
Figure 5.2 Master curves of (a) P2VP200k/SiO ₂ (b) P2VP100k/SiO ₂ and (c) P2VP400k/SiO ₂ samples constructed from the small-amplitude oscillatory shear results by the time-temperature superposition principle (TTSP). The insets show comparisons between plateau moduli and quantifications of hydrodynamic effect by Guth-Gold equation	81
Figure 5.3 Shift factors used to construct the master curves of (a) P2VP100k/SiO ₂ , (b) P2VP100k/SiO ₂ , and (c) P2VP100k/SiO ₂	82
Figure 5.4 Engineering stress σ_{eng} versus elongation ratio λ curves of P2VP200k-7v%R9.5 (filled) with those of neat P2VP100k (empty) as reference.....	83
Figure 5.5 Engineering stress σ_{eng} versus elongation ratio λ curves of (a) P2VP200k-3v%R9.5, (b) P2VP200k-9v%R23, (c) P2VP400k-3v%R9.5, and (d) P2VP400k-8v%R9.5 with their neat matrices as references	84
Figure 5.6 Engineering stress σ_{eng} versus elongation ratio λ curves of P2VP200k and P2VP200k/SiO ₂ samples at two different Hencky rate $\dot{\epsilon}$ (main figure and inset), respectively....	85
Figure 5.7 The stress overshoot σ_s of P2VP200K/SiO ₂ nanocomposites and the neat polymer at different $\dot{\epsilon}$ at a reference temperature of 413K. A master curve is observed after a sample-dependent constant $a(\varphi_{NP})$ is multiplied to the $\dot{\epsilon}$ in the x-axis	86
Figure 5.8 The stress overshoot σ_s of (a) P2VP200K/SiO ₂ and (b) P2VP400k/SiO ₂ samples and the neat polymer at different $\dot{\epsilon}$ at a reference temperature of 413K	87
Figure 5.9 Engineering strain-elongation ratio curves for P2VP200k/SiO ₂ samples with two $a(\varphi_{NP})\dot{\epsilon}_{ref}$ values of 0.021 and 0.90 in the main figure and inset, respectively	88
Figure 5.10 (a) A comparison between $a(\varphi_{NP})$ and hydrodynamic reinforcing factor X for P2VP200k/SiO ₂ samples. (b) A comparison between $a(\varphi_{NP})$ and τ_{PNC}/τ_d of all P2VP/SiO ₂ samples where τ_{PNC} is the apparent terminal relaxation time of a PNC and τ_d is the terminal relaxation time of polymer. The inset shows a comparison between τ_d/τ_{PNC} the and the experimental data in Choi et al.'s work ⁷⁵	89

CHAPTER 1 A REVIEW OF MECHANICAL REINFORCEMENT IN POLYMER NANOCOMPOSITE MELTS

1.1 Background and Motivations

The inclusion of nanoparticles (NPs) in polymer matrices can significantly improve various properties of the matrices, such as mechanical, optical, and dielectric properties¹⁻³. Due to their superior properties, lightweight, and low cost, polymer nanocomposites (PNCs) have been researched and commercialized in many fields⁴⁻⁶. For instance, the utilization of PNC revolutionized the automotive industry by greatly reducing material costs and improving fuel efficiency. In 1985, Toyota first initialized commercial research on Nylon-6/clay polymer nanocomposites (PNCs)⁷. The timing belt cover made by PNC was subsequently commercialized in 1991. In the 2000s, other automotive companies like General Motors and Chevrolet also started to PNCs for car parts⁸. Car tire is another successful application of PNC in the car industry^{9, 10}. The addition of the nano-sized silica to the rubber matrix can significantly increase the mechanical property, grip, and durability of the tires^{11, 12}. In addition to their success in the automotive industry, polymer nanocomposites have applications reaching many other fields, i.e., food packaging^{13, 14}, gas separation^{15, 16}, dielectrics^{17, 18}, sports equipment, and more.

The great success in the industries has motivated the research for better PNCs with enhanced properties. To design a PNC with desired properties, the structure-property relationship cannot be ignored¹⁹. Different combinations of polymer-nanoparticle interaction, nanoparticle loading, and nanoparticle shape can lead to different polymer and nanoparticle structures and thus influencing the final properties of the PNC^{3, 20}. However, even if the material formula is fixed, different processing procedures and methods can lead to drastically different product properties^{19, 21}. For instance, shearing in the melt processing and sonication in solvent processing

of PNCs help to disperse the NPs in the polymer matrix²⁰. And the better dispersion of NPs generally leads to superior properties due to higher interfacial area^{22,23}. Another example is a comparison between car parts and airplane parts made with the same raw materials but different processing methods¹⁹. The use of PNCs as car parts is often molded from a melt state which yields a part modulus around 20 GPa. The PNCs for airplanes, on the other hand, are first extruded to sheets to introduce NP orientations. The sheets are then laid into multiple-ply laminates with hierarchical nanoparticle structures. Thus, the final product can have around 100 GPa modulus, which is about five times higher than that of the directly molded PNC with the same compositions.

The processing of PNCs is thus an indispensable linkage between the raw materials and the final properties of PNCs. It often involves large deformation and both shear and extension modes of deformation. Some common processing methods mainly involve shear are melt mixing, extrusion, etc.²⁴ On the other hand, extension is the major deformation mode in film blowing, blowing molding, and thermoforming^{25,26}. Typically, extensional deformation can introduce more effective structural rearrangement in both polymer and nanoparticles than shear deformation²⁷. Due to the presence of nanoparticles, the mechanical reinforcement shows up during melt processing. The mechanical reinforcement in the PNCs has been one of the fundamental properties in applications and an intriguing scientific problem. Many applications require strong mechanical properties from the PNCs, such as automotive parts, packaging materials, and gas separation membranes³. And the origin of mechanical reinforcement remains a challenging topic, especially in the large deformation regimes involving nonlinear responses²⁸⁻³⁰. A better understanding of the mechanical reinforcement in the large deformation regime can help to improve the processibility and study the structure-property relationship. It also aids the

development of the constitutive models of the PNCs to predict the rheological behaviors and the mechanical reinforcement³¹⁻³³.

The thesis investigates the fundamental mechanisms involved in the mechanical reinforcement in polymer nanocomposites in two important aspects: nanoparticle rearrangement and polymer deformation. Rheology is the first tool used to study the mechanical reinforcement in PNC under large uniaxial deformation. While the rheology gives a macroscopic mechanical response of PNCs, the utilization of the small-angle x-ray scattering (SAXS) and small-angle neutron scattering (SANS) allows a decoupling of the dynamics of nanoparticles and that of matrix polymers. The nanoparticle position and rearrangement under deformation can be quantitatively studied by the SAXS experiments. The utilization of SANS can selectively quantify the polymer deformation. The recently proposed spherical harmonic expansion analysis on deformed polymers³⁴ was used to unambiguously quantify the anisotropy of the polymer in the PNC. With the help of different experimental tools (rheology, SAXS, and SANS), this thesis shows how external deformation affects the nanoparticle microstructure evolution, the polymer deformation, and how they are related to the mechanical reinforcement in the PNCs. Several important dynamics were found to influence the mechanical reinforcement in the PNCs: (i) nanoparticle microstructure rearrangement does not follow the macroscopic deformation field in general, (ii) that a strong modification of the local strain field near the nanoparticles (the hydrodynamic effect), and (iii) the imposed nanoconfinement effect by nanoparticles.

Chapter 1 serves as a review of the mechanical reinforcement in the PNCs under large deformation and motivation for this study. The background and motivation have been discussed in this section. Section 1.2 reviews the experimental techniques used in this work (rheology, SAXS, and SANS). Section 1.3 discusses the hydrodynamic effect of the nanoparticles, a

fundamental reinforcing mechanism in the PNCs. Section 1.4 provides an introduction of current understandings of the nanoparticle rearrangement under large deformation. Section 1.5 raises the specific research questions to be addressed, and Section 1.6 outlines the following chapters.

1.2 Experimental Techniques

1.2.1 Rheological Methods

The linear rheological response of the polymers and polymer nanocomposites can be obtained by a rheometer through small-amplitude oscillatory shear (SAOS). **Fig. 1.1** shows a sample is filled in a cone and plate geometry. In a SAOS test, a sinusoidal strain is applied to the sample as $\gamma(\omega, t) = \gamma_0 \sin(\omega t)$ where γ_0 is a constant strain value, ω is frequency, and t is time. The shear stress of the sample can be expressed as $\sigma(\omega, t) = G' \gamma_0 \sin(\omega t) + G'' \gamma_0 \cos(\omega t)$. Here, G' is the storage modulus which represents the solid-like behavior of the sample and the loss modulus G'' represents the liquid-like behavior. While a typical frequency range accessed by a rheometer is from 100 to 0.01 rad/s, the time-temperature superposition principle (TTSP) can be used to construct a master curve. **Fig. 1.2** shows a sketch of the typical master curve of a linear entangled monodisperse polymer. The master curve usually can span a frequency range over a decade. The TTSP assumes that every relaxation mode of the polymer follows identical temperature dependence. Thus, the SAOS tests performed at different temperatures can be combined together to construct a master curve. Although TTSP works for majorities of the polymers, it might fail for PNCs with high loadings because of the emergence of the nanoparticle network^{35, 36}.

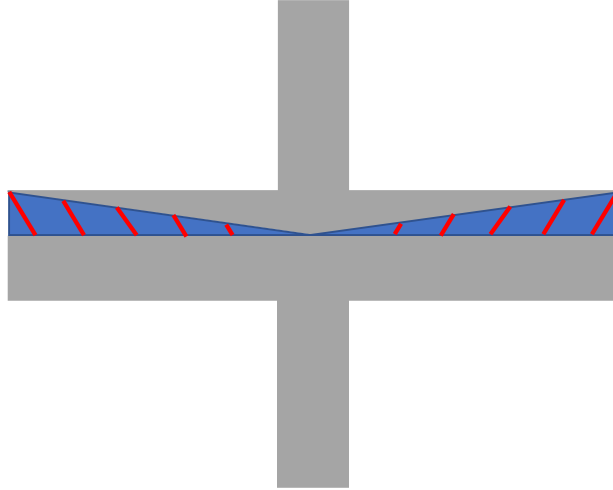


Figure 1.1 A schematic of cone and plate geometry (grey regions) of a rheometer filled with a sample (the blue region with red lines)

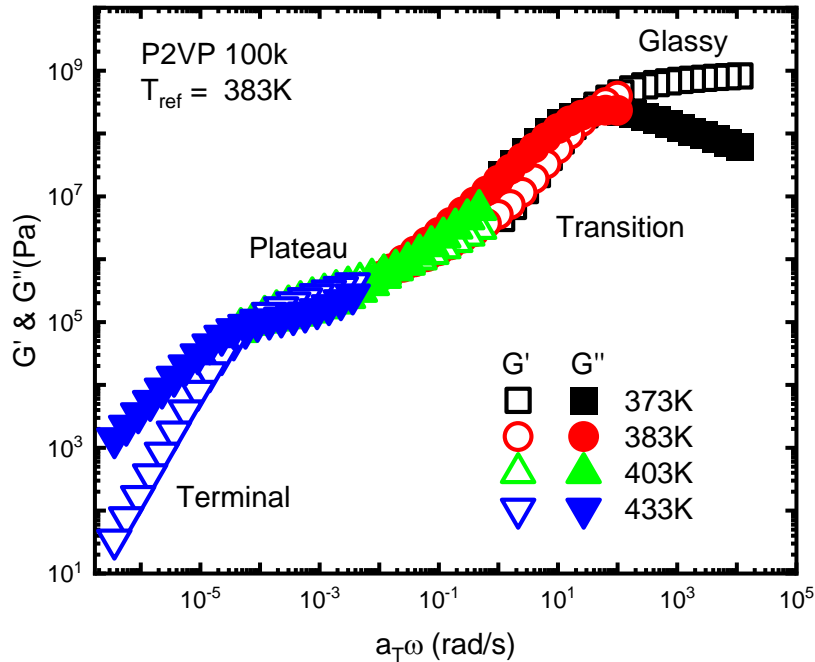


Figure 1.2 The master curve of monodisperse Poly(2-vinylpyridine) (P2VP) with weight-average molecular weight of 100 kg/mol constructed by the time-temperature superposition principle. Four regions are notified: glassy, transition, rubbery plateau, and terminal region³⁷.

Linear rheology of PNC can provide qualitative information about the nanoparticle loading and microstructure. In the rubbery plateau region, the hydrodynamic effect of the nanoparticles dominates where the plateau modulus of the PNC G_{PNC} should follow the Smallwood-Einstein relation as $G_{PNC} = G_{polymer}(1 + 2.5\phi_{NP})$ where $G_{polymer}$ is the plateau

modulus of the polymer and φ_{NP} is the volume fraction of the nanoparticles³⁸. If the G_{PNC} follows the Smallwood-Einstein relation, the nanoparticles are dispersed. On the other hand, interfacial polymer layer and nanoparticle aggregation can provide larger effective nanoparticle fraction, leading to a larger reinforcement. If an interconnected nanoparticle network is formed, the plateau modulus can be even more enhanced because of the contribution from the nanoparticles³⁹. In the terminal regime, the shift of the crossover and upturns of the G' and G'' are always seen in the PNCs compared to the polymer curves. A stronger upturn usually suggests the higher loading of the PNCs. When a critical loading is reached, the PNC can demonstrate a gelation behavior in the terminal regime, suggesting a presence of a nanoparticle network⁴⁰.



Figure 1.3 A picture of Sentmanat Extension Rheometer (SER3) mounted on an Anton Paar MCR302 Rheometer

Compared to linear rheology, nonlinear rheology is more intriguing because it involves the rearrangement of the nanoparticles and the deformation of the polymer entanglement network. Many instrumentations were invented to conduct extensional rheology, such as Filament Stretching Rheometer^{41,42}, and Meissner Extensional Rheometer⁴³. Unlike traditional instrumentation, a recent invention by Sentmanat⁴⁴ is small enough to be incorporated into the existing rheometer systems, as shown in **Fig. 1.3**. The Sentmanat Extensional Rheometer 3 (SER3) has two steel drums that can counter-rotate to uniaxially extend the sample mounted. The sample size can be as small as 0.05 mm by 1 mm by 13 mm (thickness by width by length) and can achieve an elongation ratio (final length divided by initial length) up to 148.4.

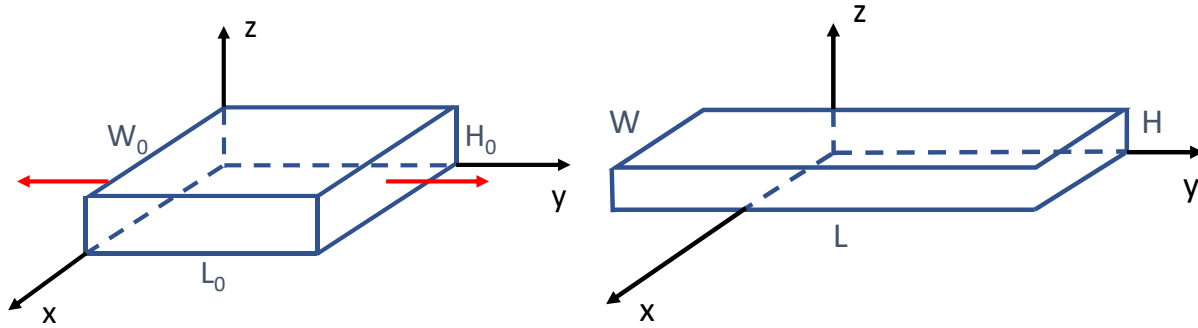


Figure 1.4 Schematic of a cuboid sample before (left) and after (right) uniaxial extension in a cartesian coordinate with length L , width W , and height H . The subscript of 0 refers to the initial dimensions of the sample. Red arrows indicate the stretching direction.

For a cuboid sample under uniaxial extension shown in **Fig. 1.4**, the elemental Hencky strain $\Delta\varepsilon$ can be given as $\Delta\varepsilon = \Delta\lambda/\lambda = (\Delta L/L_0)/(L/L_0) = \Delta L/L$ during a time interval Δt as $\Delta t = \Delta L/V$. The Hencky strain rate thus has the expression of $\dot{\varepsilon} = \lim_{\Delta t \rightarrow 0} \frac{\Delta\varepsilon}{\Delta t} = V/L$. A relationship between the elongation ratio and the Hencky strain can also be obtained: $L/L_0 = \lambda(t) = \exp\left(\int_0^t \dot{\varepsilon}(t) dt\right) \equiv \exp(\varepsilon)$. While the length of the sample increases by a factor of λ , the width and the thickness reduce by a factor of $\lambda^{0.5}$. The engineering stress $\sigma_{eng}(t)$ can be calculated by

the stretching force $F(t)$ generated by the sample divided by the initial cross-sectional area of the sample A_0 . The true stress can be calculated by the $F(t)$ divided by the instantaneous area of the sample $A(t) = \frac{A_0}{\lambda} = A_0 \exp(-\varepsilon(t))$. The transient viscosity (also referred to as elongational viscosity) can be calculated by $\eta_E^+(t) = \sigma_{tr}/\dot{\varepsilon}$.

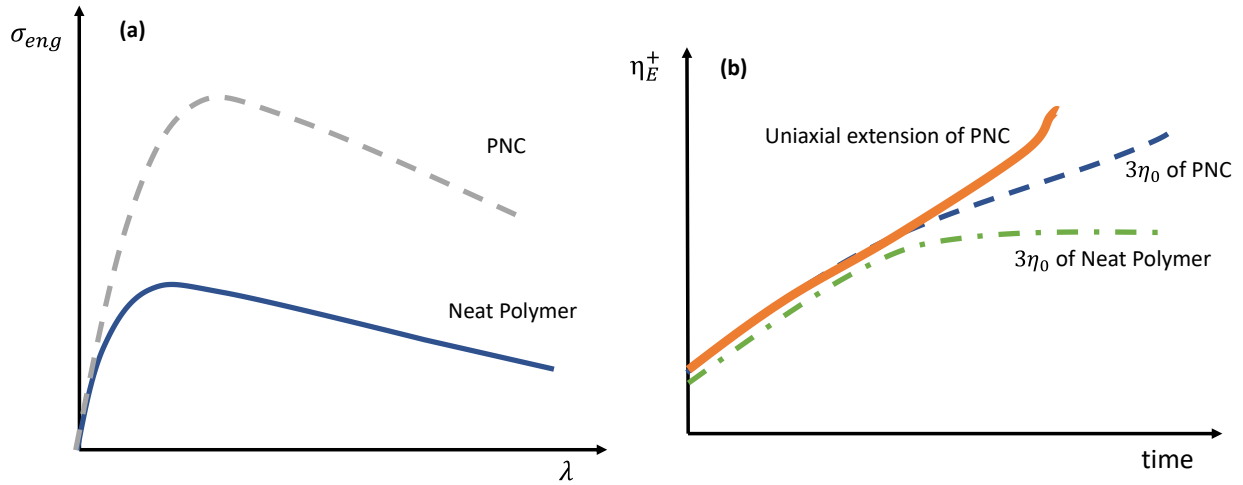


Figure 1.5 (a) stress-strain curves of a PNC and a neat polymer and (b) elongational viscosity responses of a PNC and a neat polymer under uniaxial extension. η_0 is the zero-shear viscosity.

Two types of graphical representation are usually used to compare the mechanical properties between PNCs and neat polymers. **Fig. 1.5a** shows that the stress-strain curves of the PNC have a higher magnitude than that of the neat polymer under the same extension condition. In **Fig. 1.5b**, the linear response of the PNC is higher in terms of viscosity than that of the neat polymer. PNC under extension usually shows the strain hardening behavior where the transient viscosity of the PNC shows a departure from the transient viscosity $\eta_E^+(t)$ as demonstrated in **Fig. 1.5b**. Both observations in σ_{eng} and $\eta_E^+(t)$ show the presence of mechanical reinforcement in the PNCs.

1.2.2 Small-angle X-ray Scattering

Small-angle x-ray scattering (SAXS) can access structures with 1-1,000 nm range⁴⁵, with a scattering angle less than 1° .⁴⁶ While a nanoparticle has a typical size of 1-100 nm, SAXS

becomes a commonly used method to quantify the nanoparticle size and structures in polymer nanocomposites. Although transmission electron microscope (TEM) can also be used to access such information, the sample preparation for TEM is time-consuming, and the sample size characterized by TEM is only in a length scale of micrometers. The local structure probed by TEM does not necessarily represent the bulk sample. However, SAXS can probe the nanoparticle information in the sample on a millimeter-scale, which better represents the bulk sample. In a SAXS experiment, an incident x-ray beam shoots through the sample, and the scattered x-ray is captured by a two-dimensional (2D) detector, as shown in **Fig. 1.6**.

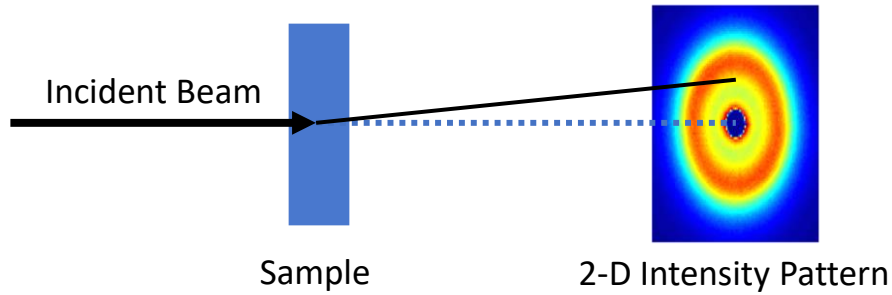


Figure 1.6 An experimental setup for x-ray scattering

The scattering intensity is dependent on the scattering wave vector $Q = 4\pi \sin(\frac{\theta}{2})/\lambda_{x-ray}$, where θ is the scattering angle and λ_{x-ray} is the wavelength of the x-ray. The obtained x-ray intensity from the detector is expressed as $I_{detector}(Q) = I_0 A \zeta \chi \Delta\Omega (v \frac{d\Sigma}{d\Omega}(Q) + B)$ where I_0 is the incoming flux, A is the illuminated section of the sample, ζ is the detector efficiency, χ is the transmission, $\Delta\Omega$ is the solid angle of the detector element, v is the sample thickness, and B is the background intensity. $\frac{d\Sigma}{d\Omega}(Q)$ denotes the scattered intensity in absolute units, which is the scattering from the sample. The scattering intensity of a PNC sample can be expressed as $I_{sample}(Q) = \frac{d\Sigma}{d\Omega}(Q) = \varphi_{NP} (\Delta\rho)^2 V P(Q) S(Q)$ where φ_{NP} is the loading of nanoparticles, $\Delta\rho$ is the scattering length density difference between the nanoparticle and the

polymer, V is the volume of a single nanoparticle, $P(Q)$ is the form factor of the nanoparticles, and $S(Q)$ is the structure factor of the NPs. $P(Q)$ is particle-shaped dependent and can be calculated by Fourier transform of the NP's density functions. $S(Q)$ contains the positional correlation between nanoparticles and is essentially the Fourier transform of the particle pair correlation function⁴⁵. $S(Q)$ can be used to quantify the microstructure of the nanoparticles in a PNC. For instance, a peak position Q^* in $S(Q)$ signifies the average center-to-center distance d_{cc} between the characteristic structures (either as dispersed nanoparticles or nanoparticle aggregates) by $d_{cc} = 2\pi/Q^*$ ^{47,48}. In a PNC with complicated multi-scale nanoparticle microstructure, $S(Q)$ can also be used to quantify the length scales of the hierarchical nanoparticle structures^{49,50}.

1.2.3 Small-angle Neutron Scattering and Spherical Harmonic Expansion

Small-angle neutron scattering (SANS) adopts the same principle as SAXS, with the x-ray replaced by neutrons. SANS is by far one of the best ways to characterize the single-chain structure factor, $S(\mathbf{Q})$, of polymers³⁴, which contains the chain packing information. Here, \mathbf{Q} is the scattering vector. From SANS, the radius of gyration of the polymer can be calculated with the aid of tube model³⁰. Recent work³⁴ utilizes spherical harmonic expansion (SHE) to extract the anisotropy of the polymer chain from $S(\mathbf{Q})$ without any model-dependent terms.

Partial deuteration is used to increase the contrast of hydrogenous polymers in SANS. However, with the addition of the nanoparticle in PNCs, it becomes challenging to obtain polymer's single-chain structure factor. For multicomponent polymeric materials, the total scattering comes from the scattering of different components as well as the interference terms between different components. Thus, zero average contrast method can be used to mute the scattering from the nanoparticles.

1.2.3.1 Zero Average Contrast in Polymer Nanocomposites

To examine the single-chain structure factor of polymers in a PNC via SANS, deuterated polymers, hydrogenous polymers and nanoparticles are present in the PNC. The volume normalized coherent scattering intensity of such PNC follows a relationship⁵¹: $I(\mathbf{Q}) = (\rho_H - \rho_D)^2 \phi(1 - \phi) \frac{\phi_p}{v_{\text{chain}}} S_{\text{intra}}(\mathbf{Q}) + [\phi \rho_H + (1 - \phi) \rho_D - \rho_0]^2 \left[\frac{\phi_p}{v_{\text{chain}}} S_{\text{intra}}(\mathbf{Q}) + V_p \phi_p S_{\text{inter}}(\mathbf{Q}) \right]$ where ρ_D , ρ_H , and ρ_{NP} are the scattering length densities (SLDs) of the deuterated monomer, the protonated monomer, and the nanoparticle, respectively, ϕ and ϕ_p are the volume fractions of the protonated chains and all polymers in the PNC, V_p is the total volume of chains, and v_{chain} is the number density of chains in the polymer phase. The normalized intrachain structure factor [$S_{\text{intra}}(\mathbf{Q})$] is defined as: $S_{\text{intra}}(\mathbf{Q}) \equiv \frac{1}{MN^2} \sum_{\alpha}^M \sum_{m,n}^N \langle e^{-i\mathbf{Q} \cdot (\mathbf{R}_{\alpha,m} - \mathbf{R}_{\alpha,n})} \rangle$. The normalized interchain structure factor follows: $S_{\text{inter}}(\mathbf{Q}) \equiv \frac{1}{M(M-1)N^2} \sum_{\alpha \neq \beta}^M \sum_{m,n}^N \langle e^{-i\mathbf{Q} \cdot (\mathbf{R}_{\alpha,m} - \mathbf{R}_{\beta,n})} \rangle \approx \frac{1}{M^2 N^2} \sum_{\alpha \neq \beta}^M \sum_{m,n}^N \langle e^{-i\mathbf{Q} \cdot (\mathbf{R}_{\alpha,m} - \mathbf{R}_{\beta,n})} \rangle$. Here, M is the total number of polymer chains, N is the number of segments per chain, and $\mathbf{R}_{\alpha,m}$ is the position vector of segment m in chain α . If the average SLD of the polymer phase is identical to that of the nanoparticle phase, $\phi_D \rho_D + \phi_H \rho_H - \rho_{NP} = 0$, the zero average contrast (ZAC) condition is fulfilled. As a result, $I(\mathbf{Q}) = (\rho_H - \rho_D)^2 \phi(1 - \phi) \frac{\phi_p}{v_{\text{chain}}} S(\mathbf{Q})$ with $S(\mathbf{Q}) \equiv S_{\text{intra}}(\mathbf{Q})$, and the $I(\mathbf{Q})$ is only proportional to the $S(\mathbf{Q})$ that contains the chain packing information. The single-chain structure factor can thus be obtained from SANS measurements.

1.2.3.2 Spherical Harmonic Expansion Analysis of Deformed Polymers

The structural anisotropy of deformed polymers can be analyzed from the anisotropy of the single-chain structure factor, $S_{\text{chain}}(\mathbf{q})$. For instance, analyzing the polymer radius of gyration,

R_g , along with ($R_{g,\parallel}$) or perpendicular to ($R_{g,\perp}$) the stretching direction offers a characterization of the chain orientation^{30, 52}. However, this analysis requires clear identification of the polymer scattering at low q . Experimentally, strong upturn emerges due to the scattering of NPs or NP clusters at low q region, introducing large uncertainties on the quantification of structural anisotropy through the classical R_g analysis.

Recently, spherical harmonic expansion (SHE) has been employed to quantify the structural anisotropy of deformed polymers, which was initially developed to investigate the structural distortion of simple liquids and colloidal suspension under deformation. The details of the SHE analysis for polymers have been published previously by Wang et al.³⁴ Specifically, the single-chain structure factor, $S_{chain}(\mathbf{q})$, on the magnitude (q) and orientation ($\mathbf{\Omega}$) of the scattering wave vector, \mathbf{q} , was expanded into a series of spherical harmonics: $S_{chain}(\mathbf{q}) = \sum_{l,m} S_l^m(q) Y_l^m(\mathbf{\Omega})$ where $S_l^m(q)$ is the expansion coefficient of the corresponding spherical harmonic function $Y_l^m(\mathbf{\Omega})$, and l and m are non-negative integers. For uniaxial deformed polymers, only terms with even l and zero m are allowed. Thus, $S(\mathbf{q}) = \sum_{l:even} S_l^0(q) Y_l^0(\theta) = \sum_{l:even} S_l^0(q) \sqrt{2l+1} P_l^0(\theta)$ with θ being the polar angle from the positive stretching direction and $P_l^0(\theta)$ the l_{th} order Legendre polynomials. **Fig. 1.7** shows the decomposition of a 2D SANS spectra of polymers. Technically, the structure factor of the polymer along and transverse to the stretching direction is: $S_{\parallel}(q) = \sum_{l:even} S_l^0(q) \sqrt{2l+1} P_l^0(\pi/2)$ and $S_{\perp}(q) = \sum_{l:even} S_l^0(q) \sqrt{2l+1} P_l^0(0)$. Therefore, analyzing the $S_{\parallel}(q)$ and $S_{\perp}(q)$ alone only provide a partial solution to the problem.

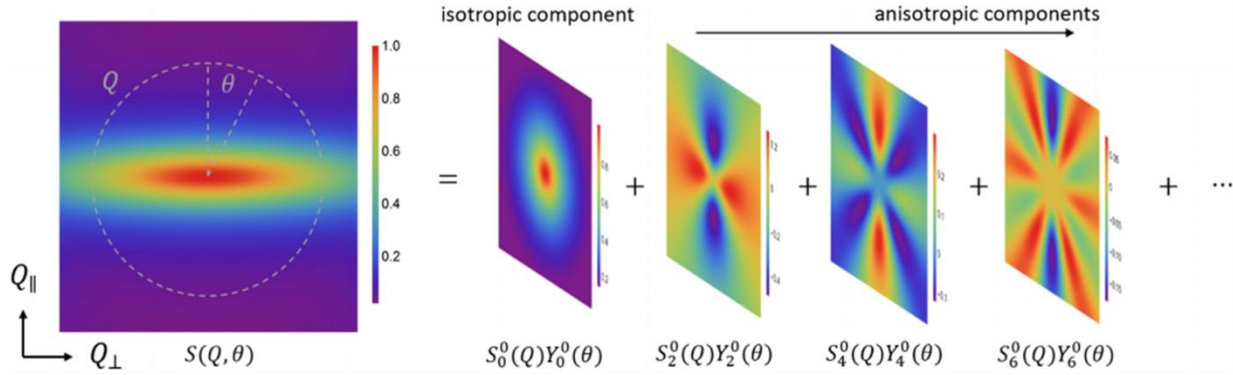


Figure 1.7 Demonstration of spherical harmonic expansion of a 2D SANS spectrum (Adapted from Ref. 34. Copyright 2017, Physical Review X)

As demonstrated in recent investigations³⁴, the expansion coefficient, $S_l^0(q)$, contains important information characterizing the structural anisotropy of deformed polymers. The $S_0^0(q)$ term is called isotropic component, and all other terms characterize different moments of structural anisotropy. Isotropic polymers only have contribution $S_0^0(q)$ and polymers with embedded anisotropy have higher-order terms. Specifically, the leading anisotropic term, $S_2^0(q)$, characterize the correlation of the polymer orientation that directly links to the macroscopic stress of the polymer. We focus on the characteristics of the $S_2^0(q)$ in the analysis and discussions below. Apparently, the SHE analysis utilizes full information of the 2D SANS spectra of a deformed polymer. More importantly, no assumptions are involved in the process of extracting the expansion coefficient, $S_l^0(q)$.

1.3 Hydrodynamic Effect of Nanoparticles and Strain Amplification

In polymer nanocomposites, one of the important reinforcing mechanisms is the hydrodynamic effect of nanoparticles. While a glassy polymer has a shear modulus G around one gigapascal (GPa), the G of the nanoparticle is often ten times more than that of the matrix. For instance, G of silica nanoparticles is 31.2 GPa, and G of titanium oxide NP is 90 GPa. When a PNC is subject to deformation, the NPs are regarded as non-deformable objects due to their

significantly larger modulus than the polymer matrix. Thus, the presence of the NPs will modify the strain field of the polymer matrix surrounding the NPs⁵³.

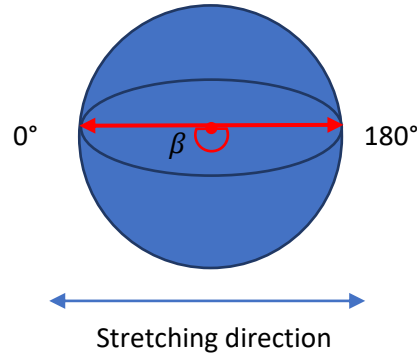


Figure 1.8 Filler immersed in a rubber matrix

In 1944, Smallwood quantified this effect by calculating the strain and stress field near a hard-sphere in a rubber matrix³⁸. Under a uniaxial deformation of the particle-filled rubber, the tension near the poles of the filler (0° and 180° shown in **Fig. 1.8**) is two times larger than that at a larger distance from the pole. Along the equatorial of the filler, from 0° to 90°, the normal stress changes from two times of the bulk rubber tension to 0 at 63° 26', and a further increase in the angle results in a transition to compression. The shear stress reaches a maximum at 45° and 135°, which is 1.25 times the rubber's tension.

The macroscopic Young's modulus of the rubber composite M^* is thus modified by the presence of the hard spheres: $M^* = M(1 + 2.5\varphi)$ where M is Young's modulus of the rubber matrix and φ is the volume fraction of the fillers. This equation is similar to Einstein's derivation of the viscosity increase of the spherical objects suspended in Newtonian fluids: $\mu^* = \mu(1 + 2.5\varphi)$ where μ and μ^* are the viscosities of the Newtonian fluid and the colloidal suspension, respectively^{54, 55}. The similarity originates from the mathematical analogy where the two equations take the same mathematical format. In Einstein's case, the equation was used to solve the velocity field, while Smallwood was trying to solve the displacement field. Because of this

mathematical analogy, the modulus amplification by $(1 + 2.5\phi)$ derived by Smallwood is often referred to as hydrodynamic amplification, although there is no hydrodynamics in solids⁵⁶. Note that both derivations assume a dilute filler system where a filler is in an infinite matrix.

Mullins and Tobin⁵⁷ first gave a physical meaning to hydrodynamic amplification in 1965. They argued the modulus reinforcement is from the overstraining on the polymer matrix. Because of the non-deformable nature of the hard fillers, the matrix has to deform more to compensate for the deformation of the filler. The proposal of the amplified strain of the matrix has become an active debate since then. Theoretical derivations show violations of the energy conservation laws by assuming an amplified strain⁵⁸. Different experimental evidence observed a completely opposite phenomenon. In an NMR study⁵⁹, molecular overstraining was observed in a rubber composite. A small-angle neutron scattering (SANS) study⁶⁰ also observed in a polystyrene-polyisoprene-polystyrene (PS-PI-PS) system where the PI is regarded as a filler due to microphase separation. However, later SANS studies show no sign of molecular overstraining in rubber/silica²⁹ and polystyrene/silica nanocomposites⁵². The nanoparticle-nanoparticle interactions are attributed to the mechanical reinforcement of PNCs. While the contradictory results from different research work do not prove an answer to the origin of the hydrodynamic effect, how the presence of nanoparticles affects the polymer deformation and the mechanical reinforcement still remains a complicated yet important question.

1.4 Polymer Nanocomposites under Uniaxial Extension

Abundant experimental works focus on the nanoparticle (NP) rearrangement of the PNCs under deformation^{25, 28, 61-63}. Indeed, the structural rearrangement of the NP network can contribute to mechanical behaviors. However, the correlation between the local organization of the NPs and the macroscopic mechanical reinforcement remains a challenge in the field of

polymer nanocomposites. Different PNC systems have specific interactions between polymer-NP and NP microstructures, and a leading parameter for mechanical reinforcement is still under research²⁸. This section summarizes the NP structure rearrangement under large deformation and how the mechanical reinforcement is affected.

Under the uniaxial extension, the macroscopic sample elongates in the stretching direction and shrinks in the transverse-to-stretching directions. The sample follows the affine deformation that its length increases as a factor of elongation ratio λ while its width and thickness shrink as a factor of $\lambda^{0.5}$. The macroscopic deformation field can thus change the NP microstructures. Ideally, a PNC system with well-dispersed spherical NPs is the most straightforward system to study the correlation between NP microstructure rearrangement and mechanical reinforcement because of their well-defined structures. This system reduces the complications of the microstructure orientation and inter-aggregate rearrangement in an aggregated NP system or system with other NP shapes. In the case of well-dispersed spherical NPs, the NPs should follow the affine deformation with the polymer matrix, assuming the Brownian motion of the NPs is negligibly small during the macroscopic deformation. The average center-to-center distance d_{cc} of NPs thus becomes $d_{cc}\lambda$ in the stretching direction and $d_{cc}/\lambda^{0.5}$ in the transverse-to-stretching directions at an elongation ratio λ . Even though this is the simplest system, complications can still arise at larger deformation. As the NPs come close in the transverse-to-stretching directions, there exists a critical point where the NPs can collide. In the small deformation regime where the NPs remain well-dispersed, the hydrodynamic effect should be the dominant mechanical reinforcement mechanism, as discussed in the previous section. When the NPs collide at larger deformation, potential NP-NP interactions and their contributions to the mechanical reinforcement should be considered. However, studies on the mechanical

reinforcement in PNCs at large deformations with well-dispersed nanoparticle system is not found in the literature due to early difficulties in controlling the dispersion state of the nanoparticles.

The closest study we found to the ideal system focuses on polymethylmethacrylate/silica nanocomposites systems with NP aggregates with controlled sizes by Jouault et al.²⁸. At low loadings of NPs, the aggregates are well-separated, and no significant reinforcement is observed under uniaxial deformation. As the loading increases, a connected NP network is present throughout the sample. A strong mechanical reinforcement is seen at the beginning of deformation due to the resistance from the NP network to the deformation. After the breakdown of the NP network upon further deformation, affine and non-affine deformations of the NP aggregates were observed in two PNC systems with different NP-polymer interactions. The PNC with affine deformation of NPs after network breakdown shows less mechanical reinforcement than the ones with non-affine deformation. The authors argued that the non-affine deformation system is from the further breakdown of the non-uniform aggregates. Although this work thoroughly studies the NP microstructure rearrangement, a clear bridge between the NP microstructure rearrangement and the mechanical reinforcement observed in the PNC is not yet established.

In Jouault et al.'s work, both NP loading and NP-polymer interaction were varied to study the NP aggregate motions under deformation, but the rate effect was still left for investigation. Many works show the deformation rate can significantly influence the NP rearrangement and the mechanical reinforcement in the PNC^{25, 61}. Okamoto et al. observed strain hardening in polypropylene (PP)/clay nanocomposites under deformation at a slow rate⁶². From the transmission electron microscope (TEM) images of the stretched PNCs, the authors observed a

'house of cards' structure formed by the clay NPs under deformation. They believe the aggregation of the layered clays occurs through the attraction between the negatively charged faces and the positively charged edges of each layer, leading to a gelation state in the PNC and thus the strain hardening. However, for higher rate tests where no nanoparticle aggregation is present, the mechanical reinforcement was not explained.

1.5 Research Objectives

The mechanical reinforcement in polymer nanocomposites under large deformation remains a complex and controversial problem. The polymer and nanoparticle contributions are not clearly understood in the current literature. By utilizing powerful experimental tools (rheology, SAXS, and SANS) and a model polymer nanocomposite system with well-dispersed spherical nanoparticles, this thesis aims to understand the mechanical reinforcement in polymer nanocomposites under large uniaxial extension.

The specific questions to address are: (a) What is the role of NP microstructure evolution? (b) How does the presence of NPs influence polymer deformation? (c) What is the leading order effect in mechanical reinforcement? By answering these important questions, this thesis can help the design, processibility, and constitutive equation development of polymer nanocomposites.

1.6 Outline of Thesis Chapters

Chapters 2 and 3 aim to understand the correlation between nanoparticle microstructure rearrangement and mechanical reinforcement in PNCs. Chapter 4 utilizes the small-angle neutron scattering (SANS) technique to obtain the polymer deformation in PNCs and its relation to mechanical reinforcement. Chapter 5 discovers the relation between effective Weissenberg number and the mechanical reinforcement in PNCs.

In Chapter 2, a deformation-induced nanoparticles network is found in a PNC with initially well-dispersed nanoparticles. This network only occurs at Weissenberg number $Wi = \dot{\epsilon}\tau \ll 1$ where $\dot{\epsilon}$ is the extension rate, and τ is the terminal relaxation time determined in the linear rheology. The NP rearrangement is characterized by small-angle x-ray scattering (SAXS), and the yield of the network is concluded to cause the strain hardening in the PNC.

Chapter 3 extends the NP microstructure analysis to different extension rates and elongation ratios. The dynamics of NP rearrangement is investigated. The spherically harmonic expansion (SHE) analysis of SAXS gives the leading anisotropic factor S_2^0 of the nanoparticles, which is hardly correlated with the stress in PNCs. Thus, the evolution of NP contribution to the macroscopic stress decouples from the evolution of macroscopic stress, supporting the polymer dominated stress in PNCs except for PNC deformation at a very low Wi discussed in Chapter 2.

Chapter 4 shifts the focus to polymer deformation in the PNC since the NPs are proven to be decoupled from the mechanical reinforcement. SANS combined with SHE analysis shows identical polymer deformation in PNC and in neat polymer under the same stretching conditions. This result supports the hydrodynamic effect of the nanoparticles as the leading order effect for the mechanical reinforcement. In observation of the stress relaxation in PNCs with aggregated NPs, the polymer anisotropy in the PNC is found to be negligible, and the relaxation of PNC is found to be faster than the neat polymer reference at the same condition. The faster relaxation can be understood by the more nonlinear deformation regimes in the PNC. The smaller polymer deformation might be from the less deformed regimes of the interfacial layer or the occluded polymer inside the aggregates.

Chapter 5 shows that the slowing down of polymer chain dynamics determines the stress-strain behaviors in PNCs. By normalizing the performed extension rate by a sample-dependent

constant, the stress-strain behaviors of PNC are found to be almost identical to those of the neat polymers. This constant strongly correlates with the bulk polymer chain relaxation, suggesting the mechanical reinforcement of PNCs at large deformation is dominated by the polymer chain dynamics. Although the presence of NPs introduces interfacial polymers, they only contribute negligibly to the mechanical reinforcement in PNCs.

Chapter 6 summarizes the work done in Chapters 2-5, point out the key issues and findings in the investigations of the mechanical reinforcement in PNCs, and gives an outlook for future research.

CHAPTER 2 DEFORMATION INDUCED NANOPARTICLE NETWORK IN POLYMER NANOCOMPOSITES UNDER LARGE DEFORMATION

The content of this chapter is modified from a published work (*ACS Macro Lett.* 2020, 9, 9, 1224–1229). The authors of this work are Ruikun Sun, Matthew Melton, Xiaobing Zuo, and Shiwang Cheng.

2.1 Introduction

The mechanical reinforcement in polymer nanocomposites (PNCs) under large deformation remains a challenge, and a clear relationship is yet established between the nanoparticle rearrangement and the mechanical behaviors. In this chapter, uniaxial extension at different strain rates was first conducted to gain a phenomenological understanding of the nonlinear rheology and mechanical reinforcement in the PNCs. While an unexpected strain hardening of PNC was discovered in the flow regime, small-angle x-ray scattering was used to probe the motion of the nanoparticles, which is correlated with the unexpected strain hardening phenomenon.

2.2 Materials and Methods

Materials: Poly (2-vinyl pyridine) (P2VP) with a molecular weight of 100 kg/mol and polydispersity index of 1.07 was purchased from Scientific Polymer Products, Inc. and was used as received. Silica nanoparticles (NPs) were synthesized by a modified Stöber method in ethanol at a concentration of 15 mg/mL^{64, 65}. According to the small-angle x-ray scattering (SAXS), the NP sizes followed a log-normal distribution with the mean radius of NP, $R_{NP} = 12.0 \text{ nm}$, and polydispersity $\sigma = 0.16$ for the first batch, and $R_{NP} = 9.3 \text{ nm}$ and $\sigma = 0.18$ for the second batch. The P2VP/SiO₂ nanocomposites with the volume fraction of $\varphi_{NP} = 4 \%$, 5% , and 7% were prepared by using the NPs from the first batch, and the $\varphi_{NP} = 8 \%$ one was prepared from

the second batch of the NPs. The preparation of polymer nanocomposites (PNCs) followed a previous protocol^{23, 66}. First, the pristine P2VP polymer was dissolved in ethanol (ACS 200 proof, Sigma-Aldrich) at a concentration of 0.015 g/mL in a 20 mL vial at 293 K. Then, the NP/ethanol suspension was drop-wise added into the P2VP/ethanol solution with the desired amount. After a two-hour mixing, 100 ppm of the Irganox®1010 (antioxidant) was added into the P2VP/NP/ethanol solution. Lastly, the PNC solution was transferred to a 50 mL Teflon dish to dry under a fume hood for 24 hours before drying in a vacuum oven at 10^{-3} - 10^{-5} torr and 313 K for 24 hours and at 423 K for another 48 hours. The pristine polymer was prepared by following the same protocol without adding NPs. After drying, the samples were melt-pressed at 453 K into thin films of around 0.1 mm in thickness in a Carver press. The thin films were then cut into rectangular strips with dimensions of 4 mm \times 18 mm (width \times length) for the uniaxial extension test. For small amplitude oscillatory shear measurements, the sample was molded into a thin disk with 4 mm in diameter and 1 mm in thickness. All the samples were stored in a desiccator under a vacuum before testing.

Rheology: Both linear and nonlinear rheological measurements were performed on an Anton Paar MCR302 Rheometer with a CTD 600 oven. The accuracy of the temperature control was ± 0.1 K. Small amplitude oscillatory shear (SAOS) tests were performed on a pair of 4 mm diameter parallel plates at a temperature range from 373 K to 453 K. The strain amplitude was 0.1% for temperatures close to the glass transition temperature of the PNCs and gradually increased to 1% at temperatures close to 453 K. The testing frequency was set as 10^2 - 10^{-2} rad/s. Uniaxial extension at constant Hencky strain rates from 10^{-3} - 6 s⁻¹ was performed at 413 K on the third generation of Sentmanat Extensional Rheometer fixture (SER-3) that mounted onto the Anton Paar MCR302. P2VPR12-7% samples for small-angle x-ray scattering (SAXS) were

prepared on SER-3 at $T = 413$ K with a constant Hencky strain rate $\dot{\epsilon} = 0.003$ s⁻¹ and $\lambda = 1.0, 2.0, 3.0, 4.0,$ and 5.0 . A fast quenching with cool air was applied to the stretched sample below their glass transition temperature to freeze the microstructure of the NPs. The SAXS measurements were then performed ex-situ at Argonne National Laboratory.

Thermogravimetric Analyzer (TGA): The mass fraction of nanoparticles of PNCs was identified on a TGA Q50 (TA instruments). For each PNC, about 10 mg of dry sample was loaded on a platinum pan in the furnace before the temperature was ramped from 293 K to 1073 K at a rate of 20 K/min in air. The mass of the NPs, m_{NP} , was obtained at the end of the test and the volume fraction of NP, φ_{NP} , was calculated through $\varphi_{NP} = \frac{m_{NP}/\rho_{NP}}{m_{NP}/\rho_{NP} + (1 - m_{NP})/\rho_P}$ with the mass density of the NP, $\rho_{NP} = 2.2$ g/cm³, and the pristine P2VP, $\rho_P = 1.20$ g/cm³.

Transmission electron microscope (TEM): JEOL 100CX was used to confirm the dispersion state of NPs and their size distribution with an accelerating voltage of 120 kV and a beam current of 100 μ A. The PNC film slices with a thickness of 100 to 150 nm were microtomed with a glass knife on RMC Boeckeler PowerTome XL at room temperature.

Small-angle x-ray diffraction (SAXS): SAXS measurements were performed at the beamline 12-ID-B at Advanced Photon Source of Argonne National Laboratory with the x-ray energy of 13.3 keV ($\lambda_{x-ray} = 0.9347$ Å). The scattered x-ray intensities were measured using a two-dimensional (2-D) Pilatus 2M detector. The sample to detector distance was set to 2.0 m, and the detecting range of the scattering wave vector, $Q = 4\pi \sin \theta / \lambda_{x-ray}$, covers from 0.0035 to 0.9 Å⁻¹, where 2θ is the scattering angle. In all measurements, we kept the sample thickness (solid thin film at 293 K) $t = 0.2$ mm and the exposure time 0.05 s. The x-ray scattering absolute intensity was calibrated using glassy carbon, and the Q values of detector pixels were calibrated using silver behenate. The 2-D isotropic scattering images were converted to 1-D

SAXS intensity curves ($I(Q)$ vs Q) through azimuthally average after solid angle correction and then normalizing with the intensity of the transmitted x-ray beam flux, using the beamline software.

To obtain the absolute scattering of NP alone, we measured the scattering signals of PNCs, $I_s(Q)$, and the background, $I_{bcg}(Q)$, with the same thickness of $t = 0.2$ mm at an exposure time of 0.05 s. The concentration-normalized scattering intensity, $I(Q)/\varphi_{NP}$, of PNCs is obtained through $I(Q)/\varphi_{NP} = (I_s(Q) - I_{bcg}(Q))/\varphi_{NP}$ which is connected with the microstructure of the NPs or assembly⁶⁷: $I(Q)/\varphi_{NP} = V(\Delta\rho)^2 S(Q) \int_0^\infty n(r_{NP})P(Q, r_{NP})dr_{NP}$. Here, V is the volume of one NP, $\Delta\rho$ is the scattering length density difference between the NP and the polymer matrix, $S(Q)$ is the structure factor of the NP assembly, $n(r_{NP})$ is the number density distribution of the NP that follows the log-normal distribution with a mean $\overline{r_{NP}} = R_{NP}$ and polydispersity σ , $P(Q, r_{NP}) = \left(\frac{3(\sin(Qr_{NP}) - Qr_{NP}\cos(Qr_{NP}))}{(Qr_{NP})^3} \right)^2$ is the form factor of the spherical NP of radius r_{NP} .

2.3 Results and Discussion

2.3.1 Small-angle X-ray Scattering and Linear Rheology

Fig. 2.1 shows the small-angle x-ray scattering (SAXS) of the PNCs, where the solid lines are the shifted form factors, $P(Q)$, of the NP. The scattering intensity, $I(Q)$, levels off at the low Q region ($Q < 1/R_{NP}$), indicating a good dispersion of nanoparticles in the PNCs^{67, 68}.

Fig. 2.2 presents the TEM images of other PNCs, as enlarged images, where nanoparticles are all individually seen and well-separated, consistent with the SAXS measurements^{23, 66, 69, 70}. The inset of **Fig. 2.1** presents the structure factors of the PNCs, $S(Q)$. The characteristic peak position, Q_c , of the $S(Q)$ provides the average center-to-center distance of NPs⁷¹, $d_{cc} =$

$2\pi/Q_c = 36.2 \text{ nm}$, 35.2 nm , 33.9 nm , and 27.2 nm . Accordingly, the average inter-particle surface-to-surface distance, $d_{IPS} = d_{cc} - 2R_{NP} = 12.2 \text{ nm}$, 11.2 nm , 9.9 nm , and 8.6 nm for P2VPR12-4%, P2VPR12-5%, P2VPR12-7%, and P2VPR9-8% respectively.

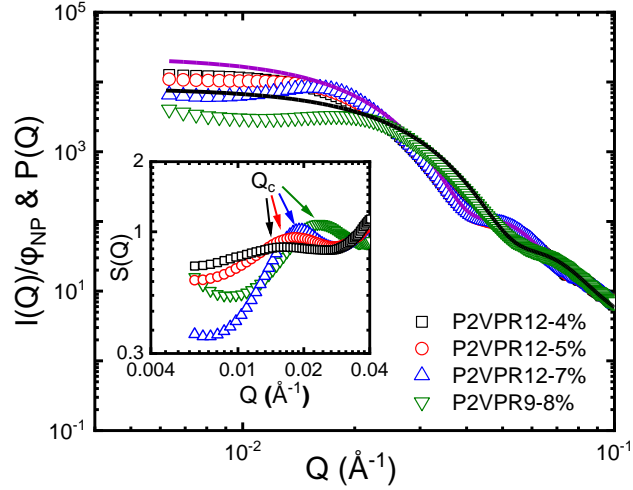


Figure 2.1 Small-angle x-ray scattering of PNCs. The solid lines are the form factors, $P(Q)$, of the two types of nanoparticles (NPs). The inset shows the $S(Q)$ of the PNCs with the primary peak position Q_c .

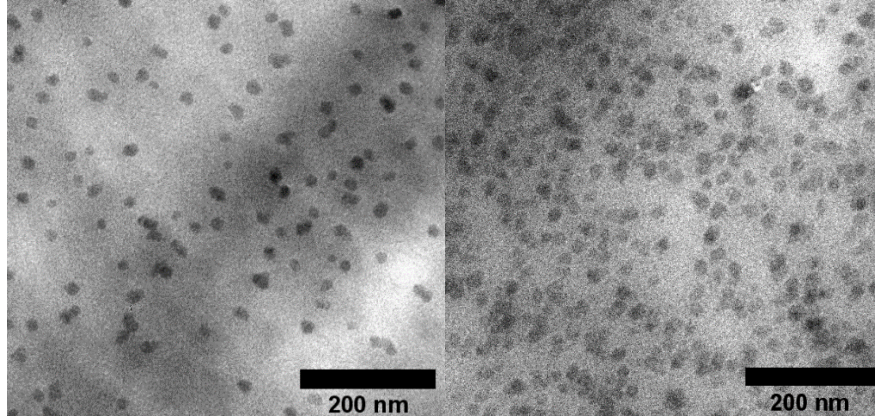


Figure 2.2 TEM images of P2VPR12-5v% (left) and P2VPR9-8v% (right).

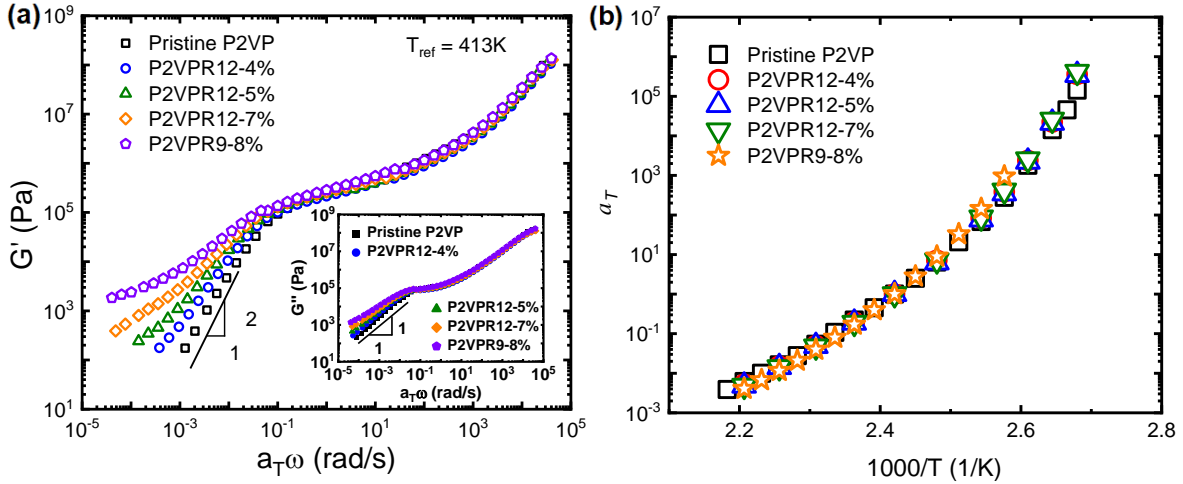


Figure 2.3 (a) The storage spectra, $G'(\omega)$ (mainframe) and the loss spectra $G''(\omega)$ (inset) $G'(\omega) \sim \omega^2$ and the $G''(\omega) \sim \omega^1$ at the low-frequency region are observed in all PNCs. **(b)** Shift factors a_T of the pristine P2VP and PNCs.

The time-temperature superposition holds for PNCs with dilute NP loadings⁷². **Fig. 2.3a** shows the linear viscoelastic spectra of the PNCs constructed through the time-temperature superposition at a reference temperature $T_{ref} = 413\text{ K}$. The shift factors a_T are almost identical across neat polymer and PNCs, as shown in **Figure 2.4 (b)**. As expected, very little mechanical enhancement is observed in the rubbery plateau region due to the low NP loadings. However, deviations of the storage modulus spectra, $G'(\omega)$, and the loss modulus spectra, $G''(\omega)$, of PNCs from the $G'(\omega) \sim \omega^2$ and $G''(\omega) \sim \omega^1$ are observed, mainly signifying the slow dynamics of the adsorbed polymers³¹. For pristine P2VP, the crossover between the $G'(\omega)$ and $G''(\omega)$ offers a good estimate of the terminal relaxation time, $\tau_d = 1/\omega_c$. The NPs introduce the hydrodynamic effect⁷³ as well as nanoconfinement effect^{74, 75} that shifts the ω_c of PNCs to lower values, leading to a higher apparent relaxation time of the polymer matrix, $\tau_a = 1/\omega_c$. The values of τ_a/τ_d of PNCs are presented in the **Fig. 2.4b**.

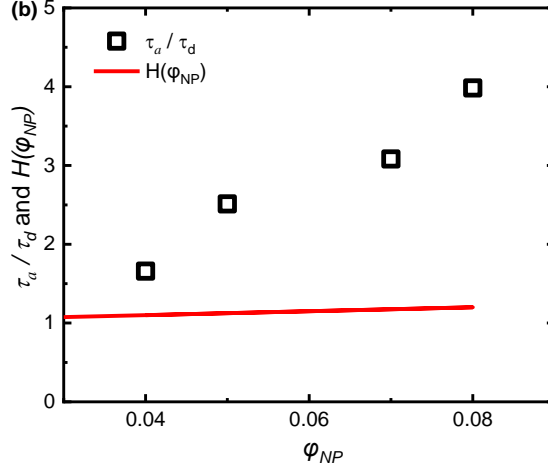


Figure 2.4 The τ_a / τ_d of the PNCs (symbols) and an estimate of the hydrodynamic effect $H(\varphi_{NP}) = 1 + 2.5\varphi_{NP}$.

2.3.2 Nonmonotonic Strain Rate Dependence on the Strain Hardening of Polymer Nanocomposites

Mechanical properties of PNCs at large deformation can provide important insights on the characteristics of the polymer-NP and NP-NP interactions not accessible in the linear viscoelastic measurements. In uniaxial extension, the apparent Weissenberg number at Hencky strain rate $\dot{\epsilon}$, $Wi_a = \dot{\epsilon}\tau_a$, represents the effective deformation rate of the polymer matrix for PNCs and $Wi_a = \dot{\epsilon}\tau_d$ for pristine P2VP. **Fig. 2.5** shows the elongation viscosity, $\eta_E^+(t, \dot{\epsilon}) = \sigma_{true}(t) / \dot{\epsilon}$, of the pristine P2VP and all PNCs under uniaxial extension. Here, $\sigma_{true}(t)$ is the true stress. The solid lines are the envelopes of the $3|\eta^*(1/\omega)|$ vs $1/\omega$ from linear viscoelastic

measurements with $|\eta^*(1/\omega)| = \sqrt{(G'(\omega))^2 + (G''(\omega))^2} / \omega$. As expected for the pristine polymers (**Fig. 2.5a**), $\eta_E^+(t, \dot{\epsilon} \rightarrow 0)$ agrees well with the $3|\eta^*(1/\omega)|$ and a strong upturn in $\eta_E^+(t, \dot{\epsilon})$ has been observed at $Wi_a > 1.0$ exhibiting the well-known strain hardening in the uniaxial extension of polymers^{76, 77}.

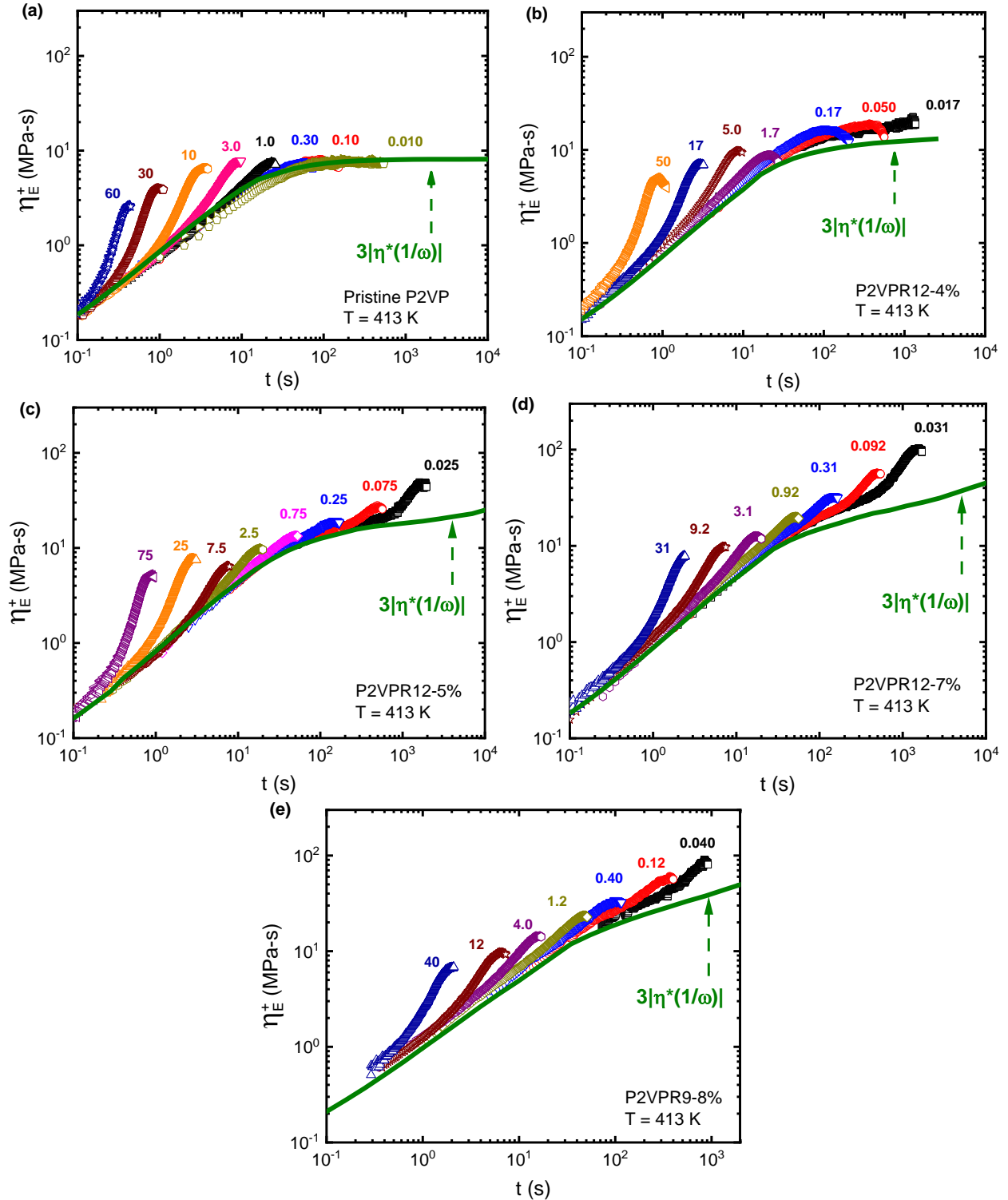


Figure 2.5 Transient viscosity $\eta_E^+(t, \varepsilon)$ vs t of (a) the pristine P2VP, (b) the P2VPR12-4%, (c) the P2VPR12-5%, (d) the P2VPR12-7% and (e) the P2VPR9-8% under uniaxial extension. The solid olive lines are the $3|\eta^*(1/\omega)|$ vs $1/\omega$ from linear viscoelastic measurements. The number labeling are the corresponding apparent Weissenberg numbers (Wi_a).

The inclusion of nanoparticles significantly modifies the mechanical responses of PNCs. For P2VPR12-4% (**Fig. 2.5b**), deviations of $\eta_E^+(t, \dot{\epsilon})$ from the linear viscoelastic envelope show up at very small $Wi_a = 0.017$. This strain hardening at the extremely small Wi_a becomes more significant as loading increases. Strong upturns of the $\eta_E^+(t, \dot{\epsilon})$ can be seen for PNCs with higher loadings (**Figs. 2.5c-e**) at Wi_a as low as 0.025. In contrast to the pristine polymer, the PNCs demonstrate a strong increase in $\eta_E^+(t, \dot{\epsilon})$ with deformation emerges both at $Wi_a > 1.0$ and at $Wi_a \ll 1.0$. Hence, the strain hardening of the PNC exhibits a nonmonotonic strain rate dependence, a phenomenon that has not been observed before in the tensile deformation of polymers²⁷.

To be quantitative, we define the strain hardening index, $\beta_{SH}(t, \dot{\epsilon}) \equiv \eta_E^+(t, \dot{\epsilon}) / (3|\eta^*(t = 1/\omega)|)$. As shown in **Fig. 2.6a**, the largest values of the β_{SH} at each $\dot{\epsilon}$ of the neat polymer (the grey lines) reduce to 1.0 with decreasing Wi_a . A similar trend in the largest values of the β_{SH} at each $\dot{\epsilon}$ approaching 1.0 is observed in the PNC (colored symbols) at $Wi_a > 1.0$ (**Figs. 2.5b-e**). However, the β_{SH} of the PNC stops declining at $Wi_a < 1.0$. A surge in β_{SH} emerges upon further reducing the strain rates, especially at higher loadings. We note that although the strain hardening of PNCs had been observed before, fundamental differences exist between the current study and previous works: (i) Strain hardening in previous works all exhibited a monotonic strain rate dependence^{62, 78, 79}, while the current work shows a nonmonotonic rate dependence. (ii) PNCs involved in previous studies were mostly composed of physical NP network that contributes strongly to the stress. However, such a percolated NP network is absent in the current study. Thus, the observed nonmonotonic rate dependence on the strain hardening of well-dispersed PNCs is unexpected and distinguishes the current study from previous studies.

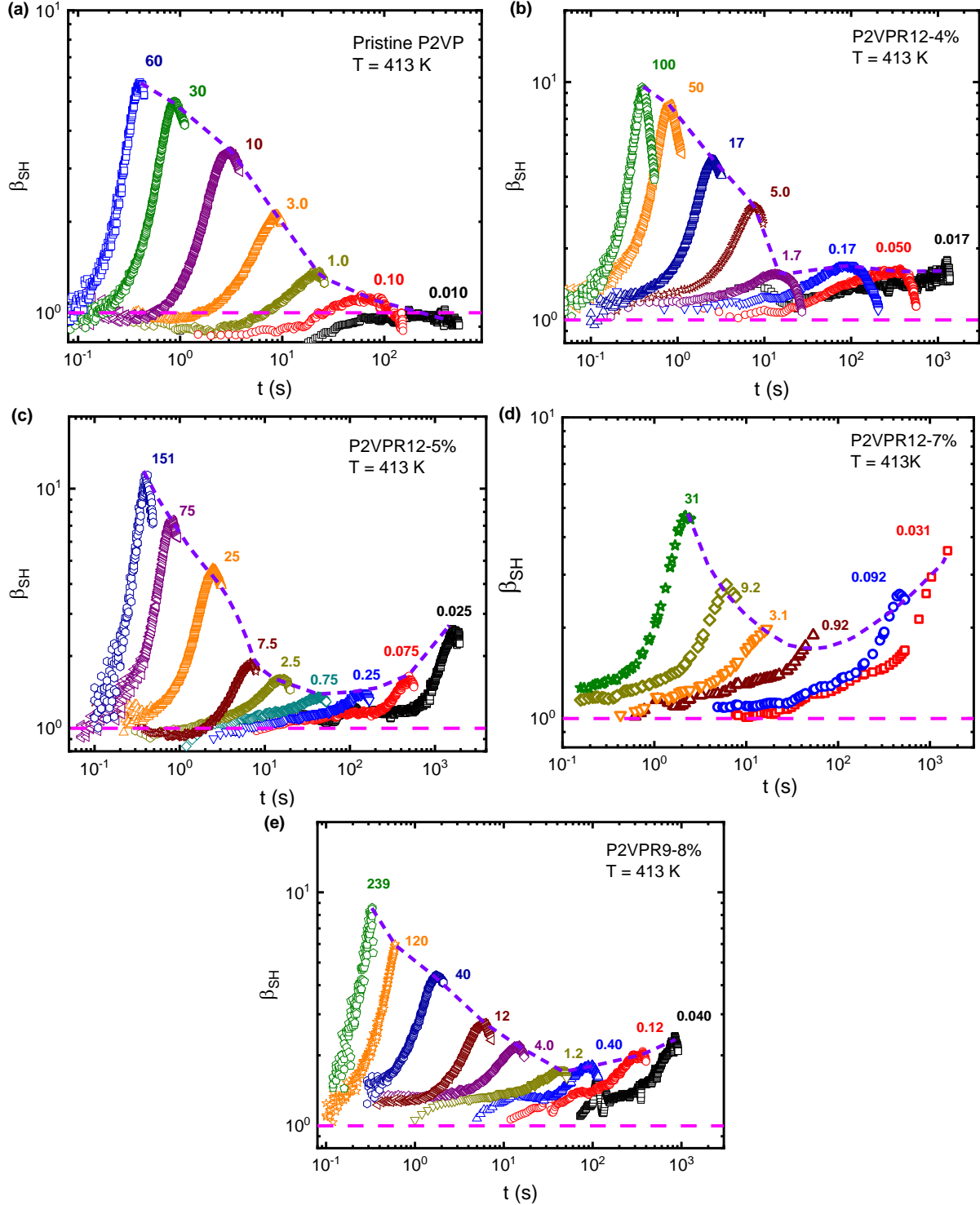


Figure 2.6 The strain hardening index $\beta_{SH}(t, \dot{\epsilon}) = \eta_E^+(t, \dot{\epsilon})/3|\eta^*(1/\omega)|$ of (a) the pristine P2VP, (b) the P2VPR12-4%, (c) the P2VPR12-5%, (d) the P2VPR12-7% and (e) the P2VPR9-8%, showing non-monotonic strain rate dependence. The purple dashed lines are a simple connection of the peak position of the $\beta_{SH}(t, \dot{\epsilon})$ at each strain rate to guide the eyes. The pink dashed lines indicate the $\beta_{SH}(t, \dot{\epsilon}) = 1$ line. The number labeling by each curve is the corresponding Wi_a .

2.3.3 Double Stress Overshoots in Stress-Strain Curves

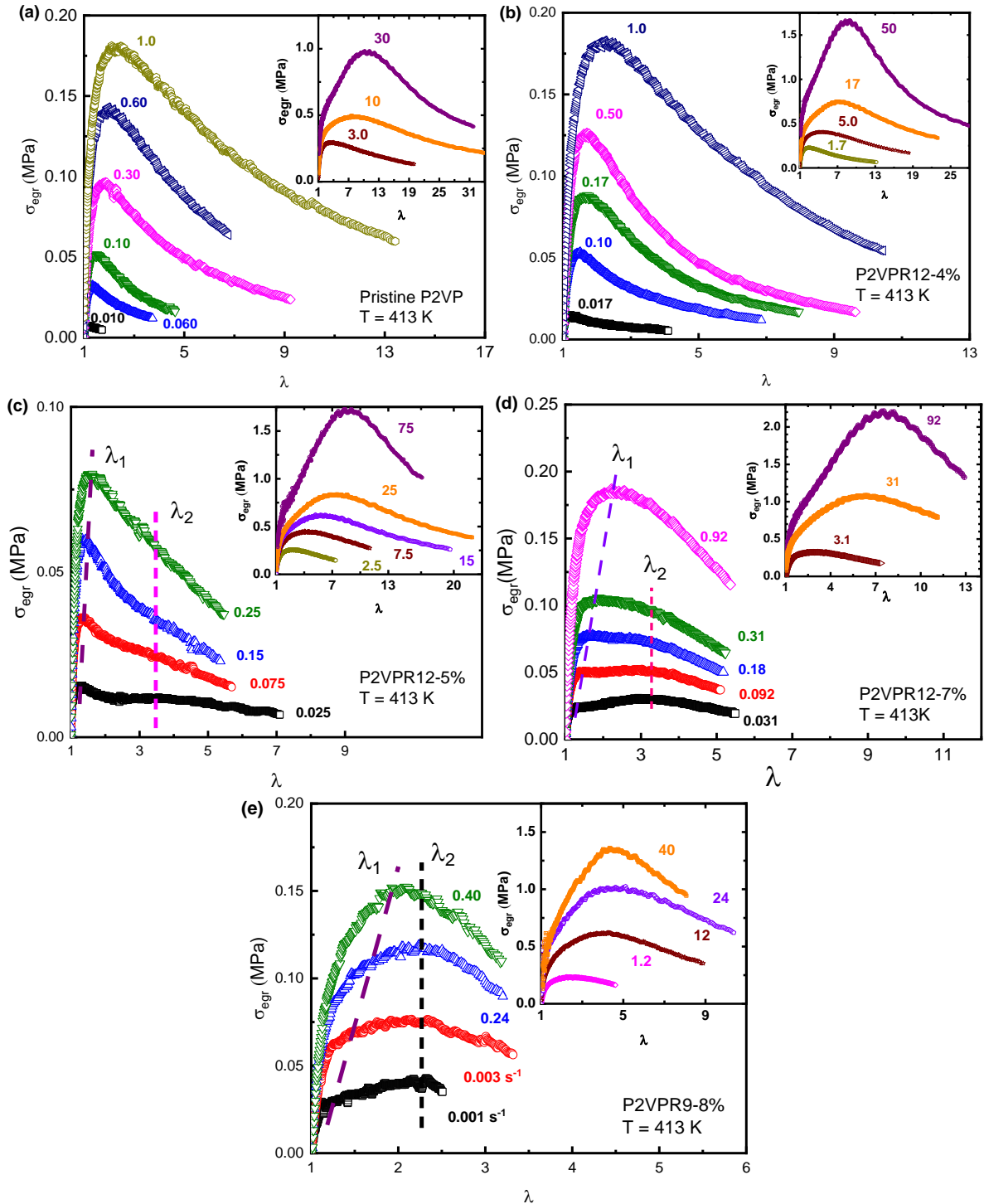


Figure 2.7 Engineering stress, σ_{egr} , vs elongation ratio, λ , of (a) the pristine P2VP, (b) the P2VPR12-4%, (c) the P2VPR12-5%, (d) the P2VPR12-7% and (e) the P2VPR9-8%. The insets show the uniaxial extension results at $Wi_a > 1.0$. λ_1 and λ_2 correspond to the two stress overshoots of PNCs at $Wi_a < 1.0$. The number labeling by each line is the corresponding Wi_a .

The observation of the unexpected nonmonotonic rate dependence of the strain hardening inspires further investigation. In the next step, we extend the scaling analysis of the uniaxial extension of pristine polymers⁸⁰ and convert the $\eta_E^+(t, \dot{\epsilon})$ vs t to the engineering stress $\sigma_{egr}(\lambda) = \sigma_{true}(\lambda)/\lambda$ vs λ representation, with $\lambda = \exp(\dot{\epsilon}t)$. In **Fig. 2.7**, the strain hardening behaviors turn into engineering stress overshoots. For pristine P2VP (**Fig. 2.7a**), one stress overshoot is observed with the characteristic elongation ratio, λ_1 , and stress, σ_1^{max} , consistent with previous reports^{80, 81}. For P2VPR12-5%, P2VPR12-7%, and P2VPR9-8% in **Figs. 2.7c-d**, there is only one stress overshoot at λ_1 at $Wi_a > 1.0$, whereas there are two stress overshoots at $Wi_a < 1.0$ with a second one showing up at λ_2 with $\lambda_2 > \lambda_1$. Note that the stress overshoots at λ_2 are associated with the strain hardening of PNCs at $Wi_a < 1.0$. However, such phenomenon is not seen in P2VPR12-4% (**Fig. 3.8b**), due to a lower amount of NP presence, which we will discuss later.

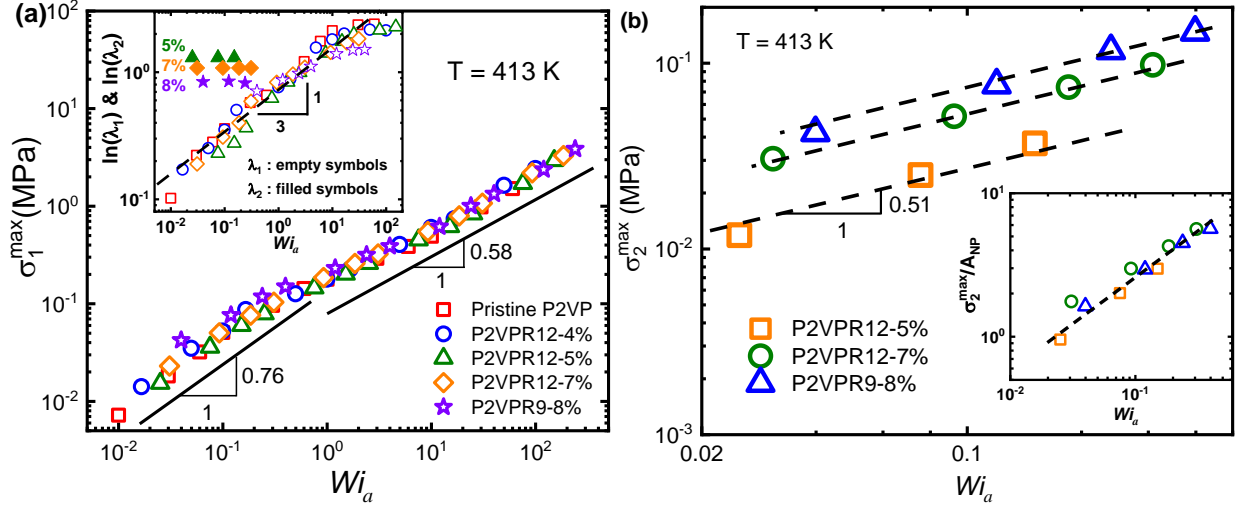


Figure 2.8 Scaling behaviors of the two stress overshoots: **(a)** The σ_1^{max} vs Wi_a (mainframe) as well as the $\ln(\lambda_1)$ (open symbols) and $\ln(\lambda_2)$ (filled symbols) vs Wi_a (inset). **(b)** The σ_2^{max} vs Wi_a (mainframe) and the σ_2^{max}/A_{NP} vs Wi_a (inset) of the PNCs. A_{NP} is the surface area of NPs per unit volume.

To quantify the characteristics of the strain hardening of PNCs, we summarize the σ_1^{max} and the σ_2^{max} in **Figs. 2.8a-b**. As shown in **Fig. 2.8a**, the σ_1^{max} vs Wi_a of PNCs of different

loadings almost fall onto the same curve as the neat polymer. A master curve of $\ln(\lambda_1)$ vs Wi_a is observed (inset **Fig. 2.8a**). According to recent development⁸⁰⁻⁸², the stress overshoot at λ_1 originates from the polymer disentanglement at large deformation. The identical scaling behaviors of $\sigma_1^{max} \sim Wi_a^{0.76}$ at $Wi_a < 1.0$, $\sigma_1^{max} \sim Wi_a^{0.58}$ and $\ln\lambda_1 \sim Wi_a^{1/3}$ at $Wi_a > 1.0$ suggests the PNCs and the neat polymer share the same molecular origin of the polymer disentanglement at the first stress overshoot. Thus, the strain hardening of the PNCs at high deformation rates ($Wi_a > 1.0$) can be attributed to the orientation and stretching of the bulk polymer. Moreover, the almost identical values of the σ_1^{max} of PNCs with different φ_{NP} also suggest a negligible contribution from the deformation of the interphase polymer at intermediate strains.

2.3.4 The Origin of Second Stress Overshoot

We now proceed to discuss the origin of the strain hardening at low deformation rates ($Wi_a < 1.0$) that is absent in the pristine polymer. Two features can be identified: (i) In contrast to the strong rate dependence of the λ_1 , the absolute values of the λ_2 do not change with Wi_a with $\lambda_2 \sim Wi_a^0$ (**Figs. 2.7c-e** and the inset of **Fig. 2.8a**) (ii) The stress values at the second stress overshoot, σ_2^{max} , scales with Wi_a as $\sigma_2^{max} \sim Wi_a^{0.51}$ (**Fig. 2.8b**). These two unique characteristics narrow down the deformation mechanism associated with the second stress overshoot. If the second stress overshoot is from the deformation of the adsorbed polymers, the entanglements dynamics require the λ_2 increases with the deformation rates^{80, 83, 84}, which cannot reconcile with the observation of $\lambda_2 \sim Wi_a^0$. If the second stress overshoot is due to the deformation of the polymer bridges between adjacent nanoparticles, the σ_2^{max} should remain unchanged with deformation rates since the strength of the polymer bridge network depends mainly on the polymer-NP interactions. However, we observed a strong rate dependence in the σ_2^{max} for all PNCs (**Fig. 2.8b**). Moreover, the stress from the polymer bridges should not exceed the

prediction of the ideal rubber law with $\sigma(\lambda) = G_b(\lambda - \lambda^{-2})$, where G_b is the modulus of the polymer-bridging network. For P2VPR12-7%, the $\sigma \approx 0.03 \text{ MPa}$ and $\lambda \approx 3.0$ at the second stress overshoot at $Wi_a = 0.031$, which leads to an estimate of $G_b \approx 10^4 \text{ Pa}$. This indicates the polymer bridge has to have a modulus at least 10^4 Pa to produce a similar level of the stress observed in experiment, which is more than 10 times larger than the modulus of P2VPR12-7% at low-frequency (**Fig. 2.3a**). Thus, the polymer bridge cannot be the major contributor to the observed second stress overshoot at low deformation rates. To the best of our knowledge, this is the first time such scaling analyses in **Figs. 2.8a-b** are applied to quantify the molecular mechanisms of PNCs at different stages of deformation.

The interesting scaling behaviors of the $\sigma_2^{max} \sim Wi_a^{0.51}$ and the $\varepsilon_2 \sim Wi_a^0$ are reminiscent of the yielding behavior of soft glassy materials^{85,86}. Although the analogy between soft glassy materials and the PNCs has been made in the past⁸⁷, the absence of an NP network in the PNCs under the study makes the analogy difficult to perceive. Is it possible that the external deformation can help percolate the NPs? According to the Stokes-Einstein equation in the absence of any polymer-NP interactions $\tau_{NP} \sim 6\pi\eta R_{NP}^3/k_B T \sim 10^4 \text{ s}$ that is much longer than the longest time of our experiments, where $\eta = 2.6 \text{ MPa} \cdot \text{s}$ is the zero-shear viscosity of the pristine polymer at $T = 413 \text{ K}$, k_B is the Boltzmann constant, and $R_{NP} = 12.0 \text{ nm}$. We emphasize that the estimate from Stokes-Einstein can be very rough since the sizes of NP should be sufficiently large in order for the Stokes-Einstein relation to be valid⁸⁸. For a similar P2VP/SiO2 nanocomposites, previous experiment have demonstrated at least two times slower of the NP diffusion than the predictions of the Stokes-Einstein⁸⁹. Therefore, there should be a negligible positional drift of NPs due to the thermal motion. Under the uniaxial extension of λ , the NP should separate apart by a factor of λ along the stretching direction (z-direction) and

come close to each other at the transverse direction (x-direction) by a factor of $\sqrt{\lambda}$.

Consequently, the inter-nanoparticle distance transverse stretching direction changes from the d_{cc} to $d_{cc}^x = d_{cc}/\sqrt{\lambda}$, promoting the formation of NP network (**Fig. 2.9a**). The strain hardening in the $\eta_E^+(t)$ vs t representation emerges at $\lambda_0 \approx 1.8$ for P2VPR12-7% (**Fig. 2.9b**). As a result, $d_{cc}^x = d_{cc}/\sqrt{\lambda_0} \approx 33.9 \text{ nm}/\sqrt{1.8} = 25.3 \text{ nm}$ that is only slightly larger than the $2R_{NP} = 24 \text{ nm}$, which may be attributed to the thin layer of the tightly bounded polymers on the surface⁹⁰.

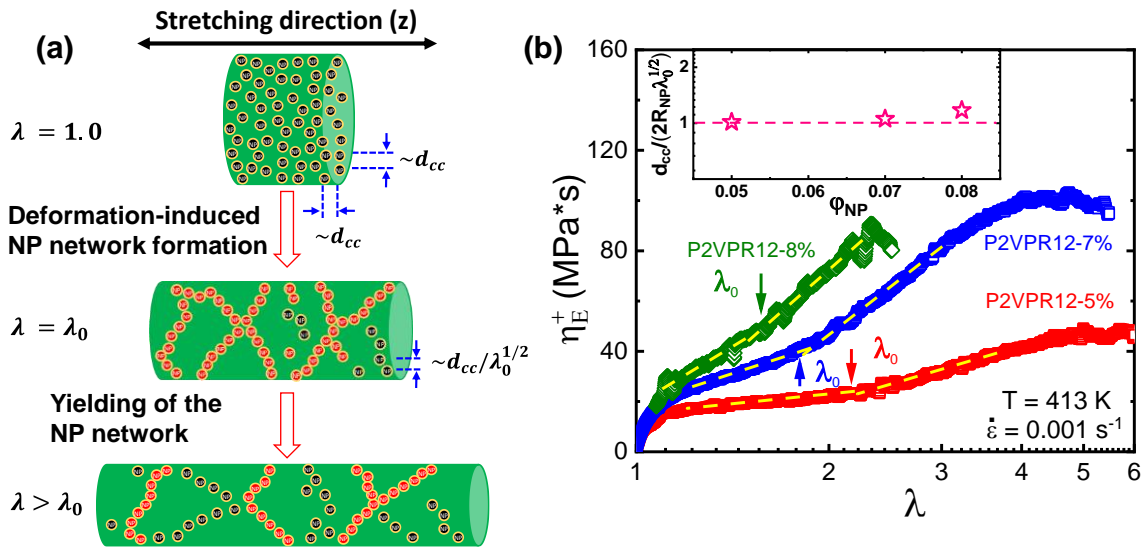


Figure 2.9 (a) A sketch of the microstructure rearrangement of PNCs at deformation. At $\lambda < \lambda_0$, the NP network has not yet formed, and the deformation of the bulk polymer matrix controls the mechanics of PNCs. At $\lambda > \lambda_0$, the deformation of the NP network triggers the strain hardening, and the yielding of the NP network leads to the second stress overshoot at $Wi_a < 1.0$. The black NPs are individually dispersed, and the red ones form networks and bear the load. The yellow shell of the NP represents the tightly bounded thin interphase polymer layer. (b) Strain hardening of PNCs of different NP loadings where PNCs with a lower ϕ_{NP} has a higher onset, λ_0 , for the strain hardening. The inset shows the $d_{cc}/(2R_{NP}\lambda_0^{1/2})$ of PNCs with different ϕ_{NP} and R_{NP} .

To understand the positional change of NPs, we turned to SAXS for PNCs at different stages of the deformation. **Fig. 2.10a** presents the mechanical response of the P2VPR12-7% at deformation, where strong strain hardening has been observed at $Wi_a = 0.092 \ll 1.0$. The inset of **Fig. 2.10a** shows the corresponding two-dimensional SAXS (2D-SAXS) pattern at different

elongation ratios. Strong anisotropy of the distribution of NPs emerges, highlighting the non-trivial influence of deformation on the positional change of NPs. The 2-D anisotropy scattering intensity of the stretched P2VPR12-7% at $\lambda = 2$ along the stretching direction (z-direction), $I^z(Q)$, and transverse the stretching direction (x-direction), $I^x(Q)$, were obtained through a line-cut analysis as demonstrated in **Fig. 2.10b** at $Q^x = 0$ (for $I^z(Q)$) and $Q^z = 0$ (for $I^x(Q)$) after solid angle correction and then normalizing with the intensity of the transmitted x-ray beam flux. The corresponding anisotropic structure factor $S^z(Q) = I^z(Q)/(\varphi_{NP}P(Q))$ and $S^x(Q) = I^x(Q)/(\varphi_{NP}P(Q))$ that are shown in the inset of the **Fig. 2.10b**.

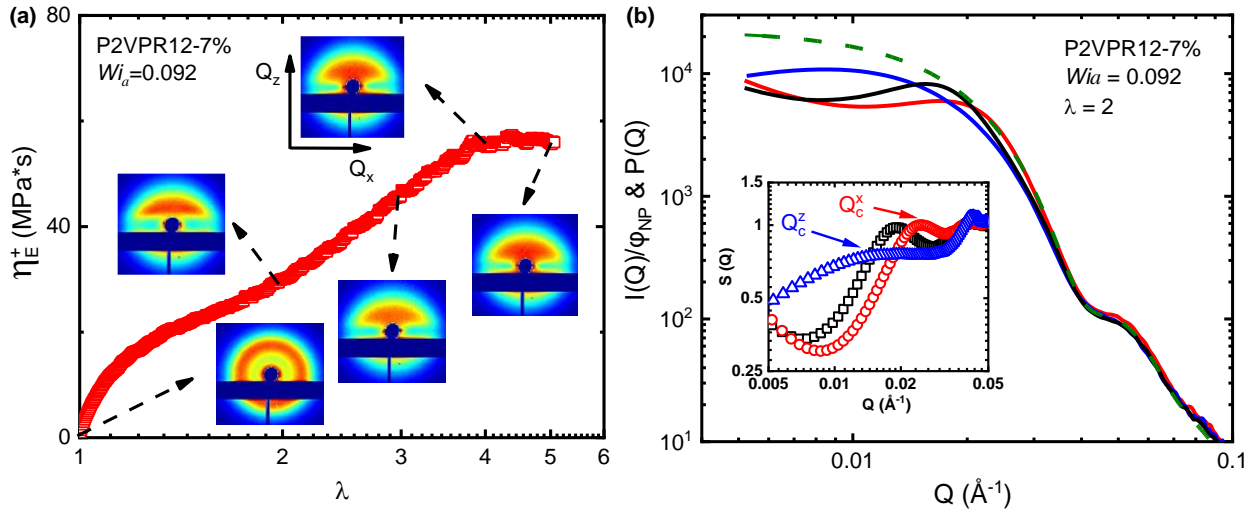


Figure 2.10 (a) Elongation viscosity of the P2VPR12-7% at $Wi_a = 0.092 \ll 1.0$. The inset presents the SAXS spectra at elongation ratios of $\lambda = 1.0, 2.0, 3.0, 4.0,$ and 5.0 . The z and x directions are the stretching direction and the transverse stretching direction. (b) The normalized scattering intensities of the stretched P2VPR12-7% at $\lambda = 2$ along the stretching (z-direction) direction, $I^z(Q)$ (the blue line), and transverse the stretching direction (x-direction), $I^x(Q)$ (the red line). The black line is the scattering intensity of the isotropic P2VPR12-7%. The dashed olive line represents the form factor of the NP. The inset represents the anisotropic structure factors of the stretched sample, the $S^z(Q)$ (the blue triangles) and the $S^x(Q)$ (the red circles), and the structure factor of the isotropic PNC (the black squares).

Fig. 2.11a summarizes the $S^z(Q)$ and $S^x(Q)$ at different elongation ratios, where the characteristic peaks offer the average interparticle distance (**Fig. 2.11b**) at z (d_{cc}^z) and x (d_{cc}^x) directions. The d_{cc}^x follows closely the affine deformation prediction (the red dashed-line in **Fig.**

2.11b) at $\lambda < 2.0$ which agrees well with the $\lambda_0 \approx 1.8$ for P2VPR12-7% from the rheology. Interestingly, the d_{cc}^x remains at around $2R_{NP}$ beyond $\lambda \approx 2.0$ suggesting the presence of interparticle collision at $\lambda \geq 2.0$. Such observations are consistent with the idea of the deformation-induced NP network formation. For the spatial rearrangement of NPs along the stretching direction, the Q_c^z peak becomes very broad with shift to the low Q region, implying a very broad distribution of d_{cc}^z at deformation. Moreover, the d_{cc}^z deviates strongly from the affine prediction (the blue dashed-line), suggesting very complex interplay between the structure rearrangement of NPs and the external deformation along the stretching direction. Previous SAXS studies on PNCs subjected to uniaxial elongation also showed similar scattering patterns of PNCs at deformation^{28,91}. Although the lack of affine positional change of NP in the stretching direction requires further investigation, the very broad distribution of d_{cc}^z facilitates the percolation of the NP network. Thus, the SAXS observation favors the above proposed mechanism on the deformation-induced NP network formation in PNCs (**Fig. 2.9a**).

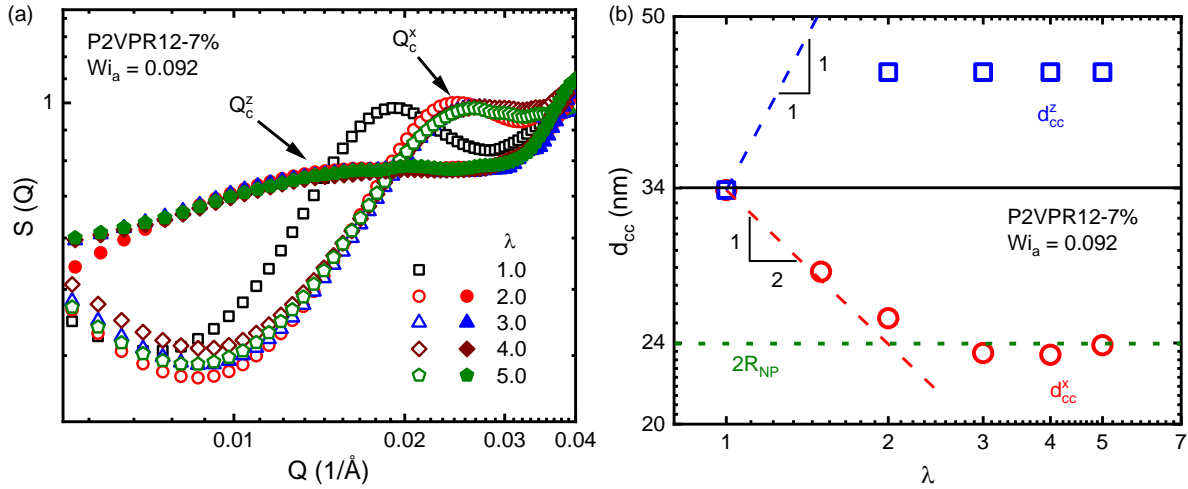


Figure 2.11 (a) The anisotropic structure factors of the PNCs along z (filled symbols) and x (empty symbols) directions. (b) The changes of the characteristic center-to-center distance of NPs along the z (d_{cc}^z) and x (d_{cc}^x) directions. The dashed lines are the predictions of the d_{cc}^z and the d_{cc}^x by assuming ideal affine positional change of NPs. The dotted line represents the $2R_{NP}$.

Moreover, the deformation-induced NP network formation depend on φ_{NP} and λ , which

explains the observed larger λ_0 for the PNC with a smaller φ_{NP} (**Fig. 2.9b**) and the almost constant λ_2 with Wi_a for a given PNC (**Figs. 2.7c-e**). Although the external deformation promotes the NP network formation, there must be a critical φ_c below which the NP network can no longer be accessible. Given the very weak strain hardening and the lack of the second stress overshoot of the P2VPR12-4% at $Wi_a < 1.0$, it is possible that φ_c is very close to 4% for $R_{NP} = 12 \text{ nm}$. Moreover, an in-depth analysis of the PNCs of different loadings shows the following relationship as $d_{cc}(\varphi_{NP})/(2R_{NP}\sqrt{\lambda_0}) \sim 1.0$ (inset **Fig. 2.9b**) for PNCs with different NP sizes, indicating the generic features of the deformation-induced NP percolation. Besides, the deformation beyond λ_0 has to involve the deformation of the NP network that is analogous to the yielding of the soft glassy materials, which also explains the observed scaling behavior of the $\sigma_2^{max} \sim Wi_a^{0.51}$ and the $\ln(\lambda_2) \sim Wi_a^0$.

Interestingly, even though the yielding of the NP network dominates beyond λ_0 , no sign of macroscopic instabilities was observed at the second stress overshoot, suggesting an intriguing translation from the nanoscale deformation to the macroscopic strain field. Another interesting feature is that the σ_2^{max}/A_{NP} of different PNCs all fall onto the same master curve against the Wi_a (inset of **Fig. 2.8b**) where A_{NP} is the surface area of NPs per unit volume of PNCs, indicating the surface characteristics of the second stress overshoot. Since the surface friction between NPs has to emerge at the yielding of the NP network, the master curve σ_2^{max}/A_{NP} offers additional support of the above-proposed NP network yielding at the second stress overshoot. Therefore, the deformation-induced percolation of the NPs initiates the onset of the strain hardening and the yielding of the NP network leads to the second stress overshoot.

2.4 Conclusions

We have reported an unusual non-monotonic rate dependence on the strain hardening of

PNCs. Scaling analyses suggest that the strain hardening at $Wi_a > 1.0$ is mainly attributed to the orientation and stretching of the bulk polymer chain, and that at $Wi_a \ll 1.0$ is ascribed to the deformation-induced NP network formation. The unexpected strain hardening in the flow regime highlight the importance of the nanoparticle rearrangement to the mechanical reinforcement in the polymer nanocomposites.

CHAPTER 3 ROLES OF MICROSTRUCTURE REARRANGEMENT TO THE MECHANICAL REINFORCEMENT OF POLYMER NANOCOMPOSITES UNDER LARGE DEFORMATION

3.1. Introduction

The previous chapter shows the deformation-induced nanoparticle network formation in the flow regime (where $Wi \ll 1$) and its elastic yield can contribute significantly to the mechanical reinforcement in the PNCs. This chapter extends the focus to investigate the influence of nanoparticle rearrangement on the mechanical reinforcement at high $Wi \gg 1$. The nanoparticle microstructures are probed by small-angle x-ray scattering at different stages of deformation under different strain rates. The average NP-NP distances in the stretching and transverse-to-stretching directions are obtained to compare with the nonlinear rheological results.

3.2 Materials and Methods

The materials and characterization methods of this chapter are the same as that of Chapter 2. This chapter added more small-angle x-ray scattering (SAXS) experiments on the pre-stretched PNCs at different elongation ratios and rates. A summary is presented here, and the details can be referred to in Chapter 2. Four nanocomposites were prepared and studied. Monodisperse poly (2-vinyl pyridine) with 100 kg/mol and two batches of synthesized silica particles were used with nanoparticle radii of 12.0 nm and 9.3 nm, respectively. Linear rheology and nonlinear rheology were conducted in an Anton Paar MCR 302 rheometer to quantify the mechanical reinforcement in the PNCs. SAXS was used to quantify the nanoparticle microstructures under different deformation conditions. **Table 3.1** summarizes the important physical parameters of the four isotropic PNC samples: average radius of nanoparticles R_{NP} determined by SAXS and confirmed by transmission electron microscope, the volume fraction of NPs φ_{NP} determined from the

thermogravimetric analyzer, and center-to-center distance of nanoparticles d_{cc} determined by SAXS.

Table 3.1 Material properties and inter-particle-to particle distances

Sample Name	R_{NP} (nm)	ϕ_{NP}	d_{cc} (nm)
P2VPR12-4v%	12.0	4.0%	36.2
P2VPR12-5v%	12.0	5.0%	35.2
P2VPR12-7v%	12.0	7.0%	33.9
P2VPR9-8v%	9.3	8.0%	27.2

3.3 Results and Discussion

3.3.1 Linear Rheology and Small-angle X-ray Scattering (SAXS)

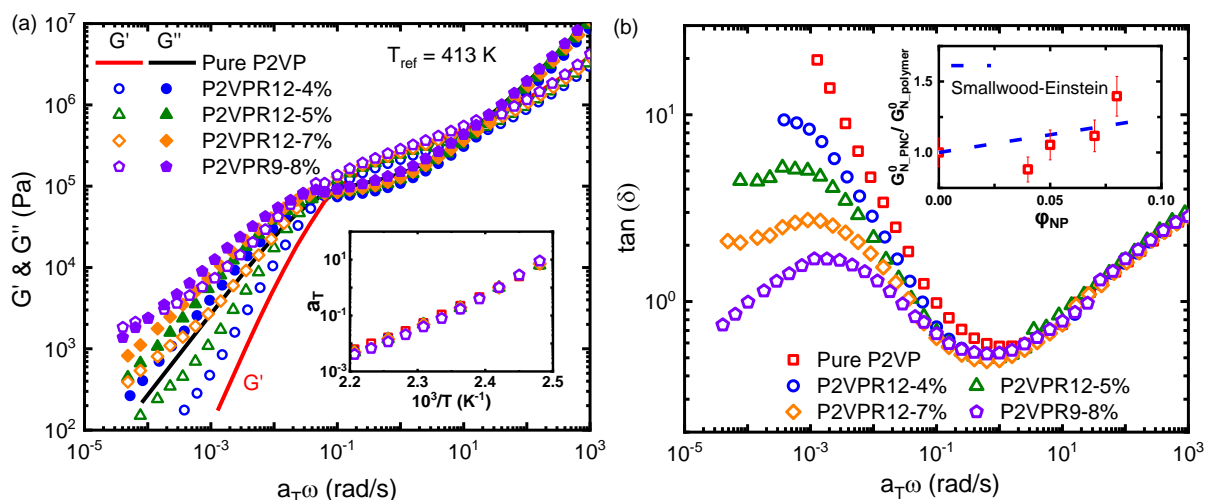


Figure 3.1 (a) Master curves of pure polymer (lines) and PNCs (symbols) constructed from time-temperature superposition principle (TTSP). Inset: Horizontal shift factors for constructing master curves. (b) Loss factor $\tan(\delta) \equiv G''/G'$ for the same samples in (a). Inset: Plateau modulus of PNC G_p^{PNC} normalized by that of pure polymer $G_p^{polymer}$ (squares) plotted against the estimation from Einstein-Smallwood relation $G_p^{PNC}/G_p^{polymer} = 1.0 + 2.5\phi_{NP}$ where ϕ_{NP} is the volume fraction of NPs.

Master curves of pure P2VP and polymer nanocomposites (PNCs) are presented in **Fig. 3.1a**. Only horizontal shifting is required to construct master curves, and the shift factors are almost identical across all samples (inset of **Fig. 3.1a**). No significant difference has been observed between the PNC and the neat polymer in the transition and rubbery plateau regimes. The reinforcement in the rubbery plateau regime is comparable to reinforcement from the

hydrodynamic effect predicted by the Einstein-Smallwood relation shown in the inset of **Fig. 3.1b**. Additionally, the loss factors presented in **Fig. 3.1b** are similar across these two regimes for all samples. These rheological results suggest the absence of nanoparticle agglomeration. The SAXS and TEM measurements in our previous work on the same set of PNCs confirm the good dispersion of nanoparticles⁹². More significant reinforcement in the linear viscoelastic spectra occurs at the low-frequency regimes where G' and G'' show upturns for all the PNCs. The extent of the upturn increases as the nanoparticle volume fraction φ_{NP} increases. As the NP loading increases, a low-frequency plateau emerges for P2VPR9-8v%, possibly due to the contributions from adsorbed and bridged chains as the NPs are well-dispersed. In the terminal regime of the neat polymer, the terminal relaxation time of the neat polymer is estimated to be 10 s at 413 K from the crossover between G' and G'' .

Uniaxial extension results on both neat polymer and PNCs are presented in **Fig. 3.2**. In our previous work⁹², we observed and thoroughly discussed the double stress maximums for PNCs at Weissenberg number $W_i \ll 1$. For instance, both P2VPR12-5% and P2VPR12-7% demonstrate the double peaks at $\dot{\epsilon} = 0.006 \text{ s}^{-1}$ in **Fig. 2b** and **2c**. However, due to the larger scale to include the $W_i > 1$ cases, the double peaks are not visible in **Fig. 3.2** for $W_i \ll 1$. When the W_i increases, only one stress peak is observed for the PNC, similar to the neat polymer. However, significant difference can be seen in the stress magnitude and the stress peak positions. Additionally, stress magnitude and the peak positions of both PNC and neat polymer clearly show a deformation rates dependence.

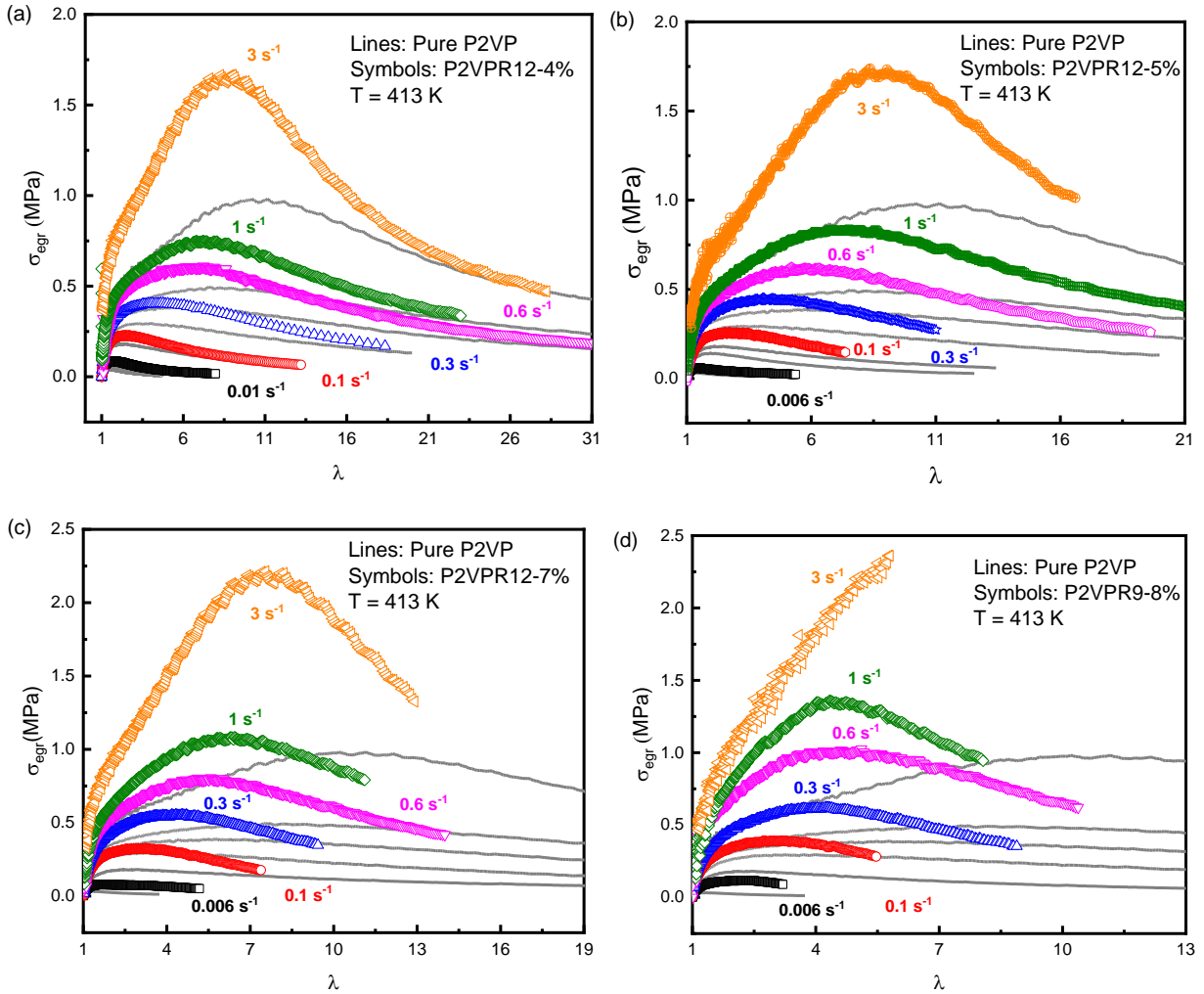


Figure 3.2 Engineering stress σ_{egr} versus elongation ratio λ of (a) P2VPR12-4%, (b) P2VPR12-5%, (c) P2VPR12-7%, (d) P2VPR9-8% at different extension rates $\dot{\epsilon}$ (in s $^{-1}$). The neat polymer data at the same rates serves as a comparison in grey lines in all plots. The stress magnitude of both P2VP and PNC increases with increasing deformation rates.

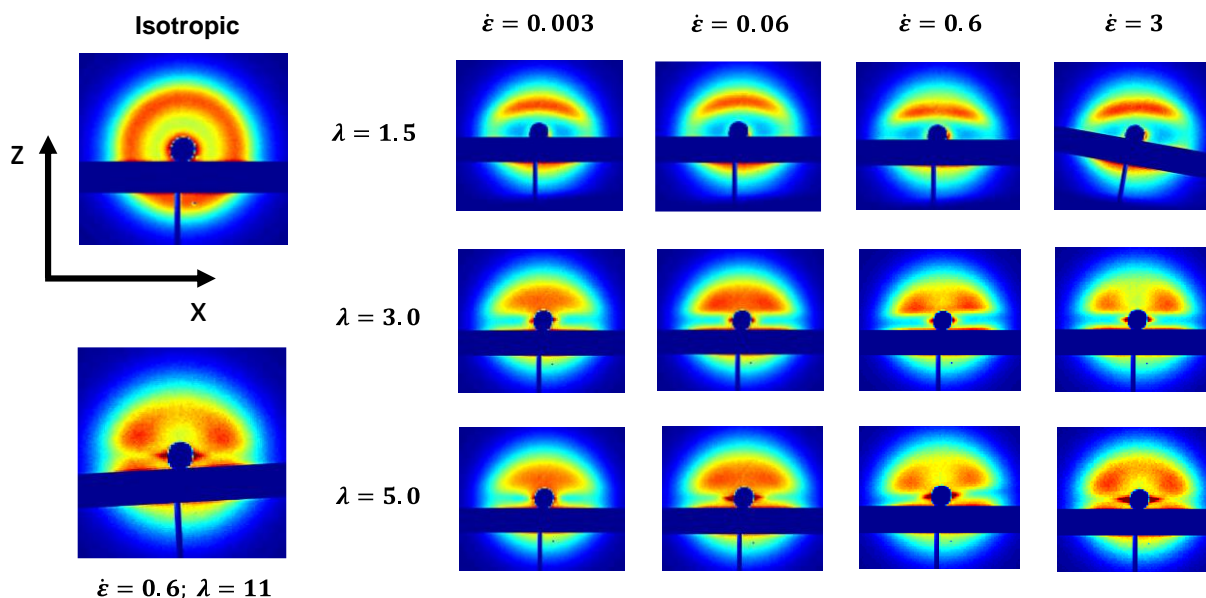


Figure 3.3 2-D SAXS patterns for P2VPR12-7% at various deformation conditions. The upper-left image is the pattern for the isotropic PNC. The 4x4 array of images are the patterns for the PNC under four different elongation rate $\dot{\epsilon} = 0.003, 0.06, 0.6,$ and 3 s^{-1} and at different elongation ratios $\lambda = 1.5, 3.0,$ and 5.0 . The images in the same row have the same λ and the images in the same column have identical $\dot{\epsilon}$. The left-down image is at deformation condition of $\dot{\epsilon} = 0.6 \text{ s}^{-1}$ and $\lambda = 11$.

In addition to confirm the nanoparticle dispersion, previous SAXS results on the isotropic samples determine the average nanoparticle surface-to-surface distance d_{IPS} to be 12.2, 11.2, 9.9, and 8.6 nm for P2VPR12-4%, P2VPR12-5%, P2VPR12-7% and P2VPR9-8%, respectively. SAXS experiments were also performed on pre-stretched PNCs with different deformation rates $\dot{\epsilon}$ at different elongation ratios, to probe the evolution of NP dispersion. In **Fig. 3.3**, the 2-D SAXS patterns of the isotropic and pre-stretched P2VPR12-7% are presented. The pattern of the isotropic PNC shows a series of symmetrical diffraction rings. Upon stretching, the scattering intensity maximum diminishes in the transverse-to-stretching (x) direction and concentrates on the stretching (z) direction. This is consistent with the literature observation, which is often referred to as the two-sided pattern. With a further increase in strain or strain rate, the two-sided pattern evolves to a butterfly pattern. The change in 2-D SAXS patterns with the increasing strain and

strain rate clearly suggests the evolution in the NP dispersion states.

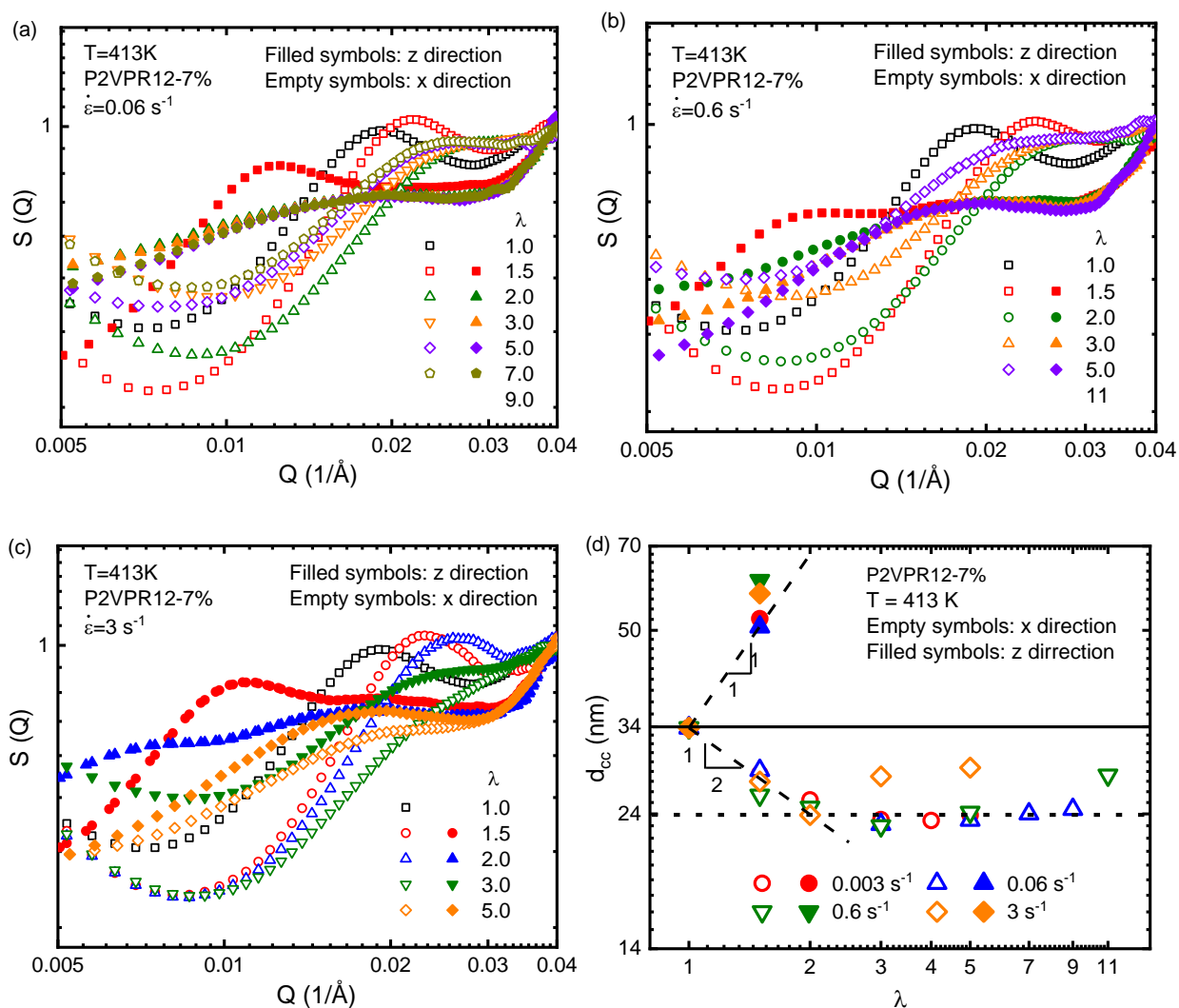


Figure 3.4. 1-D SAXS intensity curves in x and z directions at different stages of deformation for (a) extensional rate $\dot{\epsilon} = 0.06 \text{ s}^{-1}$, (b) $\dot{\epsilon} = 0.6 \text{ s}^{-1}$, (c) $\dot{\epsilon} = 3 \text{ s}^{-1}$ of P2VPR12-7%. (d) A summary of the average center-to-center nanoparticle distance in stretching direction (d_{cc}^z) and transverse to stretching direction (d_{cc}^x) at different deformation stages at different $\dot{\epsilon}$. The dash lines with a slope of 1 and 2 are the affine deformation predictions for d_{cc}^z and d_{cc}^x , respectively.

3.3.2 One-dimensional SAXS Pattern Analysis

To quantitatively understand the 2-D anisotropic patterns in **Fig. 3.4**, 1-D analysis is performed on a series of stretched P2VPR12-7% samples. In **Figs. 3.4a-c**, the NP dispersion information (structure factor $S(Q)$) is extracted from the 2-D SAXS in both stretching (z) and transverse-to-stretching (x) directions. The details of the calculation and analysis methods are

presented in our previous work⁹². On the $S(Q)$ curve, a characteristic peak at $Q = Q^*$ can be identified in the low- Q regime, which is associated with the average center-to-center interparticle distance d_{cc} by $d_{cc} = 2\pi/Q^*$. **Fig. 3.4a** shows the evolution of the structure factor $S(Q)$ in both x and z directions with deformation under an extension rate $\dot{\epsilon} = 0.06s^{-1}$. In the x direction, as λ increases, the Q^* first increases up to $\lambda = 2$ and then decreases. NP dispersion can thus be extracted from the change of the characteristic peak: the d_{cc} in x direction d_{cc}^x decreases upon stretching and then increases after λ approaches 2. As λ increases to larger than 2, the characteristic peak broadens significantly, but the broadening becomes less dramatic when $\lambda > 2$. The same behaviors are also observed in **Figs. 3.4b-c** at $\dot{\epsilon} = 0.6s^{-1}$ and $3s^{-1}$. Particularly, the broadening of the characteristic peak at $\lambda > 2$ is more significant for $\dot{\epsilon} = 3s^{-1}$ and the Q^* decreases more significantly with increasing strain than those at smaller $\dot{\epsilon}$.

On the other hand, the evolution of the characteristic peaks in z direction is very similar for all three deformation rates in **Figs. 3.4a-c**. For $\lambda > 2$, the characteristic peaks are very broad and almost identical across different strain and strain rates. While the broad peak is also seen in the case of $\lambda \leq 2$, a more significant peak is observed at a smaller Q . This major peak shifts to lower Q and becomes less significant as λ increases.

Fig. 3.4d summarizes the d_{cc} changes across different deformation rates and elongation ratios for P2VPR12-7%. Because the peak positions are difficult to obtain for peaks with significant broadening, the d_{cc}^z values for $\lambda > 2$ are not shown in this plot. Starting from the lowest rate $\dot{\epsilon} = 0.003s^{-1}$, the evolution of d_{cc}^x and d_{cc}^z with strain follows the affine deformation prediction up to $\lambda = 2$. Further deformation only slightly changes the d_{cc}^x values and the $S(Q)$ in z -direction stays almost identical. This suggests the NP motion follows the affine deformation in both x - and z - directions until the NP collisions in the x -direction ($d_{cc}^x = 2R_{NP}$). A percolating

network of NPs is induced upon deformation, and thus the NP dispersion is unchanged from SAXS results⁹².

The increase of deformation rate does not change the affine deformation of the NPs before the collision of NPs at $\lambda \approx 2$. The NPs follow the affine deformation lines at all rates. While the d_{cc}^x of $\dot{\epsilon} = 0.003 \text{ s}^{-1}$ stays constant for $\lambda \geq 2.0$, the d_{cc}^x shows an increasing trend with strain for $\dot{\epsilon} = 0.06 \text{ s}^{-1}$. Such an increase in the d_{cc}^x is more significant as the rate increases to 0.6 s^{-1} . When the $\dot{\epsilon}$ further increases to 3 s^{-1} , the d_{cc}^x shows a significant increase at a small strain ($\lambda = 3$). The deviation of the d_{cc}^x from the NP collision line suggests the breakdown of the NP network. The fact that the larger strain rate shows a deviation at a smaller strain suggest that the NP network breakdown can be accelerated by the deformation rate. On the other hand, deformation can also induce the NP network breakdown. For a single deformation rate, the deviation from the d_{cc}^x occurs as the deformation increases. Thus, the increase in either strain or strain rate can foster the NP network breakdown. Note that the induced NP network is held by the frictional forces between the adsorbed chains on the NPs. As the deformation or deformation rate increases, the polymer matrix forces increase. When the matrix force is greater than the frictional forces holding the NP network, the network can be deformed and broken down.

3.3.3 Two-dimensional SAXS Pattern Analysis

The 1-D SAXS analysis is also supported by the 2-D SAXS patterns presented in **Fig. 3.3**. At $\lambda = 1.5$ for all strain rates, the scattering maximum diminishes in the x -direction suggests the NPs come close in the x -direction and separate in z -direction³⁰. Additionally, the 2-D SAXS patterns at $\lambda=1.5$ show similar crescent-shaped scattering pattern at all rates. Both observations are consistent with the 1-D analysis that the NPs follow affine deformation at all rates before the NP collision in the x -direction near $\lambda = 2$. As λ increases to 3, the two-sided pattern still retains

at for $\dot{\epsilon} = 0.003s^{-1}$, but the scattering intensity maximum regions expand to lower Q range. As the strain rate increases, the two-sided patterns to four-point patterns at $\lambda = 3$. According to Rharbi et al., the butterfly pattern originate from the shear yielding of the NPs³⁰. Combined with the previous 1-D SAXS analysis, the change from the two-sided to four-point pattern marks the breakdown of the NP network.

Upon further deformation at $\lambda = 5$, while the $\dot{\epsilon} = 0.003s^{-1}$ patterns do not change, the intensity maximum of $\dot{\epsilon} = 0.06s^{-1}$ the pattern starts to separate into two maximums, which is more significant in $\dot{\epsilon} = 0.6s^{-1}$. In the case of $\dot{\epsilon} = 3s^{-1}$, because the NP shear yielding was achieved at $\lambda = 3$, further deformation shows a tendency to go back to the two-sided pattern. A similar pattern is seen for a smaller strain rate $\dot{\epsilon} = 0.6s^{-1}$ at a higher $\lambda = 11$ in the left-down image of **Fig. 3.3**. The d_{cc}^x values in the 1-D analysis are also similar across these two conditions. In summary, both increment in strain and strain rate can leads to the matrix stress buildup, leading to the rearrangement of the NPs. First, an NP network can be induced upon a small strain until the collision of the NPs. Further increase in the deformation and deformation rate can potentially break the network structure, where competition between the NP network modulus and the matrix modulus occurs.

3.3.4 The Correlation between Nanoparticle Microstructure Rearrangement and the Mechanical Reinforcement in PNCs

To quantify the mechanical reinforcement of PNC, we propose the stress ratio analysis of the uniaxial extension between PNC and pure polymer. The engineering stress of PNC σ_{egr}^{PNC} is normalized by that of the pure polymer σ_{egr}^{neat} across the same strain and at the same Hencky rate $\dot{\epsilon}$. **Fig. 3.5** shows the engineering stress ratios at different Hencky rates $\dot{\epsilon}$ versus the elongation ratio λ for P2VPR12-5% and P2VPR12-7%. At strain rate of $0.003 s^{-1}$, the stress ratio increases

with the deformation extent. As the rate increases, the stress ratio magnitude decreases. A clear change in the strain-dependence happens at high rates: the stress magnitude stays relatively constant until an overshoot occurs at a larger strain.

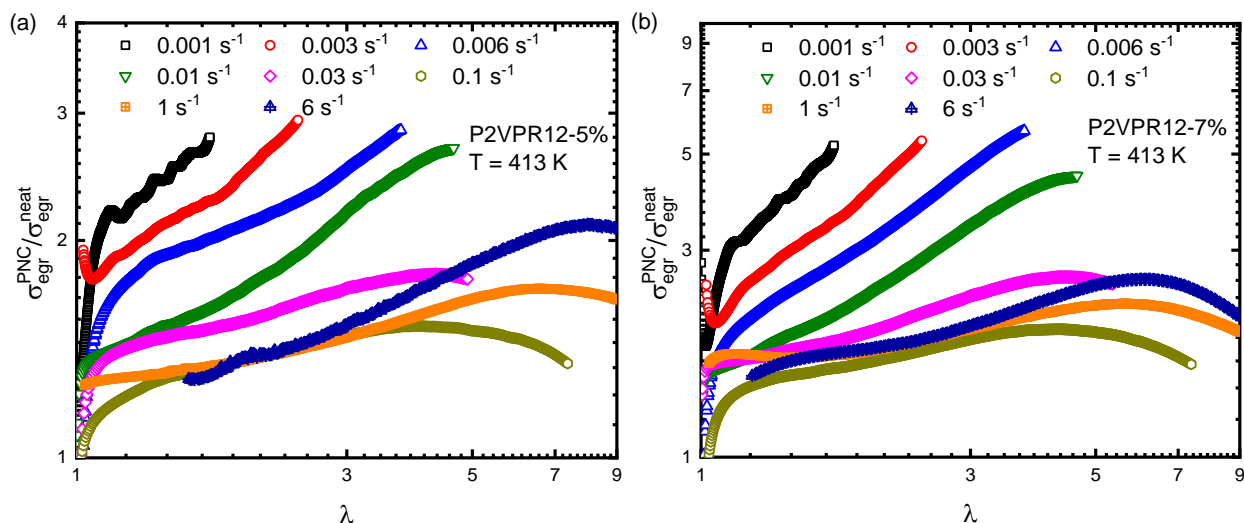


Figure 3.5. Engineering stress ratio between (a) P2VPR12-5% and (b) P2VPR12-7% and neat polymer to quantify the mechanical reinforcement under uniaxial extension. The stress ratio changes with both strain and strain rate.

Fig. 3.5 demonstrates the nonlinear rheology of the PNC is heavily dependent on both strain and strain rate. However, the SAXS analysis in **Fig. 3.4d** clearly demonstrates the nanoparticle positions are barely changed for a large strain window. The sharp contrast points the nanoparticle microstructure arrangement is not the leading order reinforcement mechanism in the PNCs at high Wi .

3.3.5 The Entanglement Network of the Matrix Polymer

In neat polymers, the engineering stress overshoot has been associated with the disentanglement process⁹³⁻⁹⁵. For a PNC stretched under the same condition as the neat polymer, a stress overshoot can also be found near the strain where the stress overshoot for the polymer occurs. However, an additional stress overshoot is found for the PNCs under uniaxial extension at a larger strain than the first stress overshoot. It has been proved that the first stress overshoot is

associated with the polymer disentanglement and the second one at a larger strain is related to the yield of the nanoparticle network. To better differentiate these two peaks in the following discussion, we name the stress and strain of the first stress overshoot as $\sigma_{max}^{polymer}$ and $\lambda_{max}^{polymer}$ and name those of the 2nd stress overshoot as σ_{max}^{NP} and λ_{max}^{NP} .

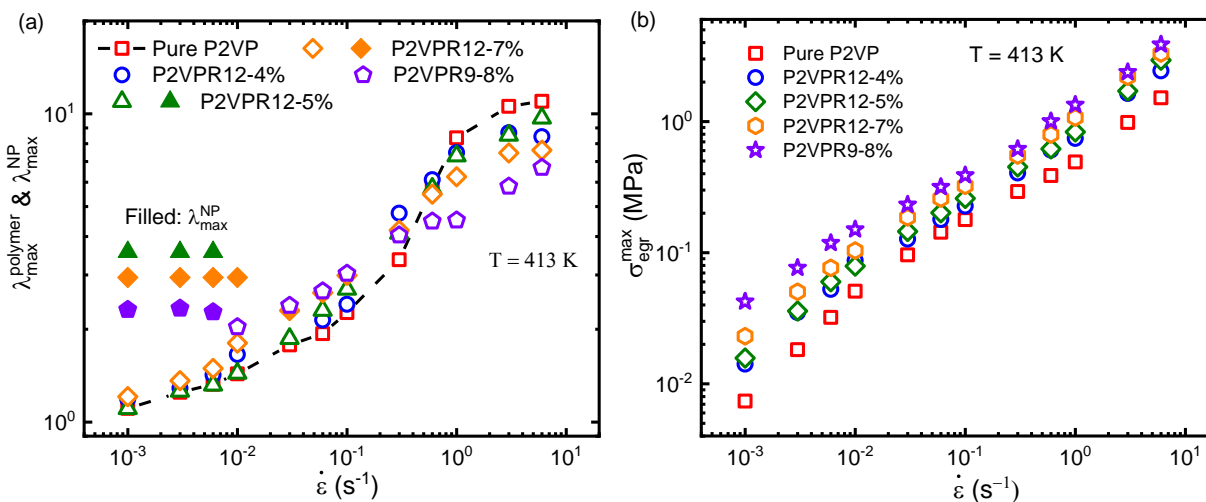


Figure 3.6 (a) The strain at the engineering stress overshoots for all samples at different rates, where the $\lambda_{max}^{polymer}$ is associated with the polymer disentanglement and λ_{max}^{NP} is related to the yield of the nanoparticle network. (b) The engineering stress overshoot associated with the polymer $\sigma_{max}^{polymer}$ is plotted across different strain rates. A factor is multiplied to each sample to normalize their $\sigma_{max}^{polymer}$ to those of the P2VPR9-8%. A good match has been found at the high-rate regime.

To further support that the $\sigma_{max}^{polymer}$ and $\lambda_{max}^{polymer}$ of the PNCs come from the polymer, we shall first discuss the effect of NP on the entanglement network. In the current system, the radius of gyration of polymers is slightly smaller than the nanoparticle radius, and thus such additional entanglement cannot be easily formed. Our SAOS data also shows the plateau modulus is consistent with the Guth-Gold prediction. If additional entanglement is present, the entanglement length will decrease, leading to an increase in the plateau modulus and shifting of ω_e to larger frequency, where ω_e is the crossover of G' and G'' between the transition and the rubbery plateau. However, this phenomenon is not observed in **Fig. 3.1b**.

Fig. 3.6a shows the $\lambda_{max}^{polymer}$ and λ_{max}^{NP} at different loadings. For $\dot{\epsilon} < 0.01$, $\lambda_{max}^{polymer}$ of PNC fall on to the envelope of the neat polymer. Between $0.1 \geq \dot{\epsilon} \geq 0.01$, the position of the $\lambda_{max}^{polymer}$ is influenced by the λ_{max}^{NP} and is thus above the neat polymer envelope. At higher rates $\dot{\epsilon} > 0.1 \text{ s}^{-1}$, the $\lambda_{max}^{polymer}$ sits below the neat polymer envelope. At the same rate, $\lambda_{max}^{polymer}$ decreases as the NP loading increases. The increased elasticity in PNC introduces more effective deformation of the entanglement network, resulting the disentanglement happen earlier in the PNCs than in the pure polymers. In **Fig. 3.6b**, similar scaling between PNC and neat polymer has been observed, suggesting no significant effect on the entanglement network.

3.4 Conclusions

The quantitative analysis of the small-angle x-ray scattering (SAXS) results of pre-deformed PNCs demonstrates the evolution of the nanoparticle rearrangement. NPs can separate along the stretching direction and come close in the transverse to the stretching direction to form a transient percolating network. The NP network resists matrix deformation to provide mechanical reinforcement, but it can be destroyed by either increased deformation or deformation rate. The nonlinear reinforcement can be categorized into two regimes. In $Wi \ll 1$ regime, the reinforcement is due to the deformation-induced NP agglomeration. In higher Wi regime, the NP microstructure change is uncorrelated with the mechanical reinforcement in the PNCs. Overall, the polymer entanglement network is not affected by the presence of NPs in both linear and nonlinear regimes, although the disentanglement process can be accelerated by the high strain rate.

CHAPTER 4 MOLECULAR ORIGIN OF MECHANICAL REINFORCEMENT IN POLYMER NANOCOMPOSITES

The content of this chapter on the poly (methyl methacrylate) (PMMA)/SiO₂ is modified from a published work (Phys. Rev. Lett. **126**, 117801). The authors for this part of the work are Ruikun Sun, Matthew Melton, Niloofar Safaie, Robert C. Ferrier, Jr., Shiwang Cheng, Yun Liu, Xiaobing Zuo, and Yangyang Wang.

The other part of this chapter on polystyrene (PS)/SiO₂ is modified from work submitted to Macromolecules. The authors for this part are Ruikun Sun, Jie Yang, Matthew Melton, Niloofar Safaie, Robert C. Ferrier, Jr., Shiwang Cheng, Yun Liu, Xiaobing Zuo, and Yangyang Wang.

4.1 Introduction

In the investigation of the mechanical reinforcement in polymer nanocomposites (PNCs), the polymer deformation is also an indispensable part, in addition to the nanoparticle microstructure rearrangement discussed in Chapters 2 and 3. While the traditional rheological investigation can only provide a mechanical response of the overall sample, SAXS can provide information on nanoparticles motions. To decouple the polymer deformation contribution from the overall mechanical reinforcement in the polymer nanocomposites, this chapter utilizes the small-angle neutron scattering (SANS) to probe the polymer deformation. More specifically, how polymer deformation is affected by the presence of the nanoparticles and contributes to the mechanical reinforcement in PNCs. Recently, the spherical harmonic expansion (SHE) was used to analyze the 2D SANS spectra on neat polymers to unambiguously quantify the polymer anisotropy under deformation. By tuning the compositions of the deuterated and hydrogenous polymers, the zero average contrast (ZAC) point was reached where the scattering length density

(SLD) of the polymer phase is matched with that of the nanoparticle phase. At the ZAC condition, the single-chain structure factor $S(\mathbf{Q})$ can be extracted from the SANS spectra without the interference from the scattering of the nanoparticles. The $S(\mathbf{Q})$ was then analyzed by SHE analysis to obtain the s_0^2 term which is the leading order anisotropy term in the expansion. The first part of this work investigates the polymer anisotropy change under uniaxial extension and stress relaxation in a PMMA/SiO₂ system with well-dispersed spherical silica nanoparticles. The second part of the chapter extends to the PS/SiO₂ system with aggregated spherical silica nanoparticles to investigate the polymer anisotropy evolution under stress relaxation processes.

4.2 Materials and Methods

Materials: Hydrogenous poly (methyl methacrylate) (H⁸-PMMA) with weight average molecular weight (M_w) of 194 kg/mol and polydispersity index, PDI = 1.08, and protonated polystyrene (H⁸-PS) were purchased from Scientific Polymer Products. Deuterated PMMA (D⁸-PMMA) and polystyrene (D⁸-PS) were purchased from Polymer Source, Inc. All polymers were used as received. **Table 4.1** summarizes the weight average molecular weight (M_w), polydispersity index (PDI), and degree of deuteration of deuterated polymers.

Table 4.1 Characteristics of polymers used in the study

Polymer Name	M_w (kg/mol)	PDI	Degree of Deuteration
H ⁸ -PMMA	194	1.08	0%
D ⁸ -PMMA	217	1.27	91%
H ⁸ -PS	310	1.05	0%
D ⁸ -PS	304	1.08	97%

Characterizations of polymers: The molecular weights of the polymers were characterized by size exclusion chromatography (SEC, Malvern OMNISEC) at 35 °C with triple detectors (light scattering, viscometer, and refractive index). The degree of the deuteration of the D⁸-PMMA and D⁸-PS was determined by a 500 MHz Varian ¹H-NMR spectrometer at room temperature. Specifically, 0.01 mmol/mL solution of Ph₃CH (internal standard) in CDCl₃ was

first prepared. Subsequently, about 50 mg of the deuterated polymer was dissolved in 0.15 mL of the internal standard solution and further diluted to 3 mL by CDCl_3 . From the relative area of the CH peak of Ph_3CH and the CH peak of deuterated polymer, the total amount of hydrogen present in the deuterated polymer can be quantified.

Preparation of nanocomposites: Silica nanoparticles/methyl ether ketone (MEK) suspensions with particle radius $R_{NP} = 8 \pm 2$ nm were obtained from Nissan Chemical America Corporation (MEK-AC-2014Z). The SiO_2 nanoparticles were first precipitated in hexane and then re-disperse into n,n-dimethylformamide (DMF, ACS grade) and tetrahydrofuran (THF, ACS grade), respectively, at a concentration of 0.15 g/mL. A parent polymer solution (PMMA/DMF or PS/THF) of 0.005 g/mL was prepared with the addition of Irganox® 1010 antioxidant (0.01 wt% with respect to the mass of the polymer). The parent solution was then passed through a poly(tetrafluoroethylene) (PTFE) filter with a pore size of 20 μm to remove impurities and dusts. Different amounts of SiO_2 suspension were added into the parent polymer solution in a glass flask under constant mixing. SiO_2 /DMF was combined with the PMMA/DMF and SiO_2 /THF was added to PS/THF. The polymer nanocomposite/solvent mixtures were dried in a Rotavap. The PNCs were further dried at 413 K under vacuum (10^{-2} torr) for 48 hours before further characterization.

In order to only observe only the polymer scattering, the nanoparticle scattering length density has to be matched by the polymer mixture. The molar ratio of hydrogen to deuterium was varied to prepare different polymer nanocomposites to find the zero-contrast matching point between the nanoparticles and the polymers. At the zero-contrast matching point, the molar ratio of hydrogen to deuterium of 0.59:0.41 was determined for the PMMA mixture, and that of 0.57:0.43 was used for the PS mixture. With this specific ratio, PMMA/ SiO_2 was prepared with a

nanoparticle volume fraction ϕ_{NP} of 8%, and three PS/SiO₂ PNCs were prepared with ϕ_{NP} of 8.7%, 18%, and 24%, respectively.

Transmission electron microscope (TEM): The dispersion state of the silica nanoparticle in the PNC sample was determined in a JEOL 100CX transmission electron microscope with accelerating voltage and beam current of 120 kV and 100 mA, respectively. The PNC was microtomed to slices of thin films of 100–150 nm thickness with a glass knife on RMC Boeckeler PowerTome XL at room temperature.

Rheology: Small amplitude oscillatory shear (SAOS) measurements were conducted on an Anton Paar MCR302 rheometer with a pair of parallel plates of 8 mm in diameter. The PNC disks with 8 mm in diameter and 1 mm in thickness were hot-press molded at 453 K on a hydraulic press (Carver, Inc). The applied strain amplitude varied from 0.1% to 1%, depending on the testing temperature. The testing temperature varied from 383 K to 453 K at an interval of 10 K. At each temperature, dynamic mechanical properties of PNCs at angular frequencies of $10^2 - 10^{-2} \text{ rad/s}$ were collected. Linear viscoelastic master curves of PNCs were constructed through the time-temperature superposition principle.

For the nonlinear rheological measurements of pristine PMMA and PMMA/SiO₂, samples were molded into rectangular sheets in a Carver press at 453 K and subsequently cut into rectangular stripes of dimensions 25 mm × 12 mm × 0.33 mm (length × width × thickness). Uniaxial extension experiments were carried out on an RSA-III solid analyzer (TA instruments) at 423 K with a constant Hencky strain rate of $\dot{\epsilon} = 0.01 \text{ s}^{-1}$. To track the molecular deformation during stretching, the experiment was stopped at different elongation ratios of $\lambda = 1.2, 1.5, 1.8,$ and 2.1 followed by a fast quench to below the glass transition temperature of the PMMA. To monitor the time evolution of the structural anisotropy, stress relaxation was performed at $\lambda =$

1.8 with different elapsed times of $t = 0\tau, 0.01\tau, 0.03\tau, 0.1\tau, 0.3\tau,$ and 1τ (τ is the terminal relaxation time of the pristine PMMA), followed by the same quenching procedure to preserve the molecular anisotropy. The glassy pristine PMMA and PMMA/SiO₂ nanocomposites were investigated by SANS.

Stress relaxation of the neat PS and PS/SiO₂ at an elongation ratio $\lambda = 1.8$ (Hencky strain of $\varepsilon = 0.6$) was carried out on RSA-III at $T = 393\text{ K}$. The initial sample size before stretching is $25\text{ mm} \times 12\text{ mm} \times 0.80\text{ mm}$ (Length \times width \times thickness). A constant Hencky strain rate of $\dot{\varepsilon} = 0.01\text{ s}^{-1}$ was applied in the stretching. The stress relaxation was then manually terminated through fast quenching below their glass temperature at different stages of $t = 0\tau, 0.01\tau, 0.03\tau, 0.1\tau, 0.3\tau,$ and 1.0τ to preserve the molecular anisotropy. The structural anisotropy of the glassy PS and PS/SiO₂ nanocomposites were then investigated by both SAXS and SANS.

Small-angle x-ray scattering (SAXS): SAXS measurements were conducted at the 12-ID-B beamline of the Advanced Photon Source at Argonne National Laboratory. The wavelength of the x-ray is $\lambda_x = 0.9347\text{ \AA}$ with an incident energy of 13.3 keV . In all measurements, the sample to detector distance was 2 m and a two-dimensional (2D) Pilatus 2M detector was used. The scattering wave vector, $|\mathbf{Q}| = \frac{4\pi\sin(\theta/2)}{\lambda_x}$, was calibrated with silver behenate with θ the scattering angle. The absolute scattering intensity, $I(\mathbf{Q})$, of the x-ray was calibrated by glassy carbon. The scattering of neat polymer was collected serving as the background scattering for detailed analysis.

Small-angle neutron scattering (SANS): SANS measurements were performed on the NGB30 SANS beamline at the Center for Neutron Research (NCNR) at NIST. The wavelength of the incident neutron was $\lambda_n = 6\text{ \AA}$. The sample to detector distances were $13\text{ m}, 4\text{ m},$ and $1\text{ m},$ covering the $|\mathbf{Q}| = \frac{4\pi\sin(\theta/2)}{\lambda_n}$ of $0.004 - 0.3\text{ \AA}^{-1}$. The measured scattering intensity was

corrected for detector background and sensitivity. Direct beam measurements were performed for the determination of the absolute intensity.

4.3 Results and Discussion

4.3.1 Poly (methyl methacrylate)/SiO₂ with Well-dispersed Nanoparticles

4.3.1.1 Zero Contrast Matching

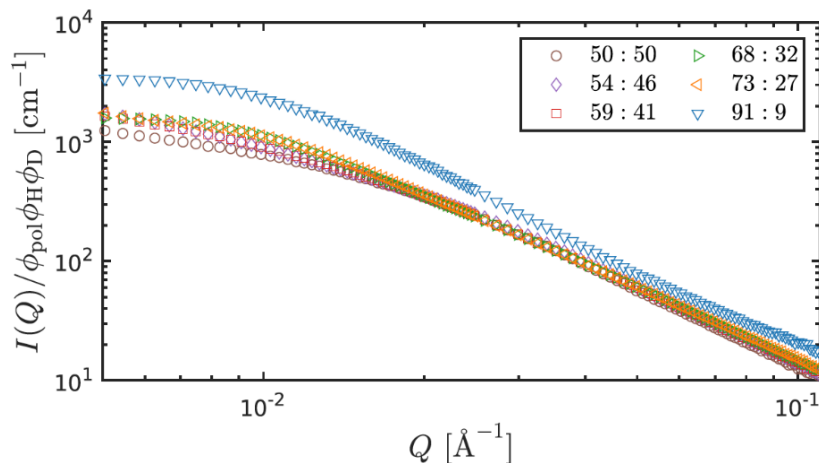


Figure 4.1 Normalized scattering intensity $I(Q)/\phi_{poly}\phi_H\phi_D$ of mixtures of H⁸-PMMA and D⁸-PMMA at different H/D ratios. Here, $\phi_{poly} = 1 - \phi_{NP}$ is the volume fraction of the polymer, and ϕ_H and ϕ_D are the volume fractions of the hydrogenous and deuterated PMMAs, respectively.

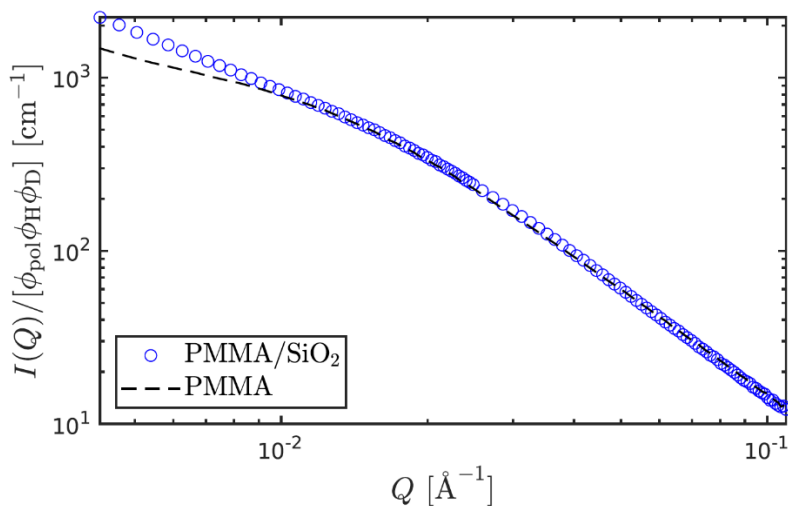


Figure 4.2 Comparison of the normalized intensities of PMMA/SiO₂ and pristine PMMA with H/D = 0.59:0.41.

We apply the zero average contrast (ZAC) method⁹⁶ to characterize the molecular deformation of the polymer matrix on different length scales by SANS, which is a key for clarifying the microscopic consequences of hydrodynamic reinforcement. A set of PMMA/SiO₂ samples was prepared with a fixed particle volume fraction $\phi_{NP} = 8\%$ and different volume fractions of D⁸-PMMA in the polymer matrix for identification of the zero average contrast (ZAC) condition. **Fig. 4.1** shows the normalized scattering intensity for this set of PNCs with different H/D ratios. In **Fig. 4.2**, the scattering intensities of pristine PMMA (H8-PMMA/D8-PMMA blend with H/D = 0.59:0.41) and corresponding PNC ($\phi_{NP} = 8\%$) overlap nicely. The ZAC point is thus confirmed at H/D = 0.59:0.41 which agrees with the theoretical calculation as well as the previous literature report⁴⁹.

4.3.1.2 Rheology and Small-angle X-ray Scattering

The H⁸/D⁸-PMMA mixture with 8 vol% 8-nm-radius silica nanoparticles was prepared and used in this study. The leveling off of the scattering intensity at low Q ($Q < 0.006 \text{ \AA}^{-1}$) in the small-angle x-ray scattering (SAXS) spectrum and transmission electron microscopy (TEM) image in **Fig. 4.3a** indicate an absence of an extensive nanoparticle network in the PNC. This conclusion is further supported by the linear viscoelastic spectra of the pristine PMMA and PMMA/SiO₂ in **Fig. 4.3b**, where the two samples exhibit almost identical loss factors, $\tan \delta \equiv G''/G'$, in the entire rubbery plateau region (**Fig. 4.3b** inset). On the other hand, the presence of NPs in PMMA/SiO₂ leads to a threefold increase of plateau modulus, compared to the pristine PMMA. These rheological and structural properties clearly show that the mechanical reinforcement in PMMA/SiO₂ is dominated by the hydrodynamic effect, rather than a network due to percolation of nanoparticles. This makes PMMA/SiO₂ an ideal candidate for SANS investigations of the influence of NPs on the molecular deformation of the matrix polymer.

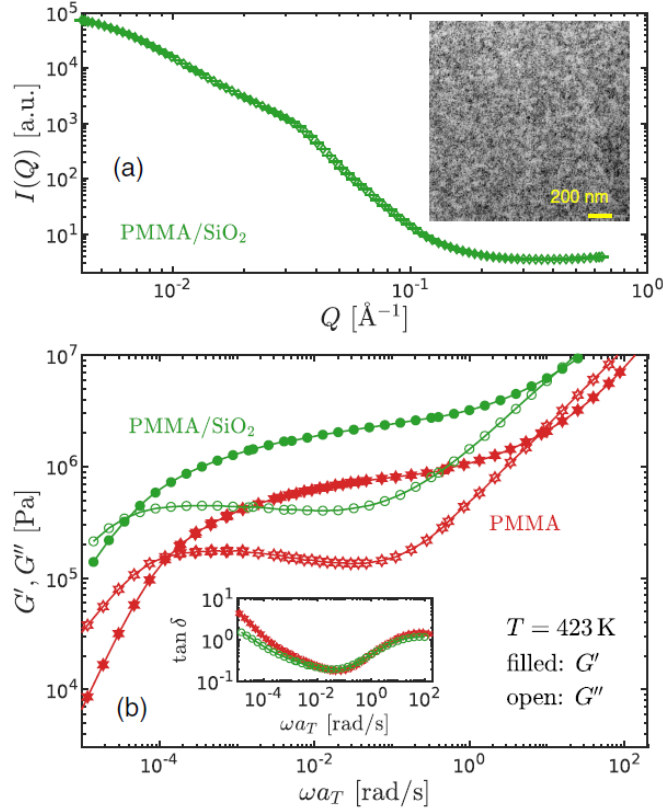


Figure 4.3 (a) Small-angle x-ray scattering spectrum of PMMA/SiO₂. Inset: TEM image of the same sample. (b) Linear viscoelastic spectra of PMMA and PMMA/SiO₂ at 423 K. These master curves are constructed using the time-temperature superposition principle⁷². Here, ω is the angular frequency and a_T is the shift factor. Stars: PMMA. Circles: PMMA/SiO₂. Inset: loss factor $\tan\delta(\omega) \equiv G''(\omega)/G'(\omega)$.

4.3.1.3 Polymer Anisotropy under Uniaxial Extension

Fig. 4.4 presents the stress-strain curves of PMMA and PMMA-SiO₂, along with the 2D SANS spectra at $\lambda = 1.2, 1.5, 1.8,$ and 2.1 . While the presence of NPs significantly enhances the mechanical stress (green circles), there is no appreciable difference between the SANS spectra of the two samples. We employ the spherical harmonic expansion analysis to further quantify the structural anisotropy from the 2D SANS spectra³⁴. This technique decomposes the SANS spectra into contributions from different symmetries and allows a clear separation of isotropic and anisotropic spectral components.

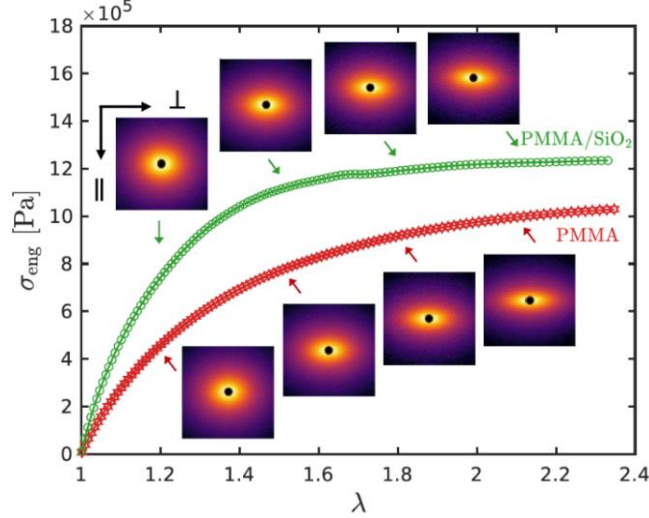


Figure 4.4 Stress-strain curves of PMMA and PMMA-SiO₂ at a constant Hencky strain rate of $\dot{\epsilon} = 0.01 \text{ s}^{-1}$ at $T=423 \text{ K}$, along with the SANS spectra taken at stretching ratios of 1.2, 1.5, 1.8, and 2.1. We point out that the stress enhancement at large strains, ca. 23%, is consistent with the hydrodynamic effect of nanoparticles from the Padé approximation.

Under the ideal ZAC condition, the coherent scattering intensity $I_{coh}(\mathbf{Q})$ of PMMA/SiO₂ should be proportional to the single-chain structure factor $S(\mathbf{Q})$ of PMMA⁹⁷: $I(\mathbf{Q}) \approx I_{coh}(\mathbf{Q}) = \varphi_{poly}\varphi_H\varphi_D n_{seg}(b_D - b_H)^2 NS(\mathbf{Q})$, where φ_{poly} is the polymer volume fraction, φ_H and φ_D are, respectively, the volume fractions of hydrogenous and deuterated chain segments, n_{seg} is the polymer segment number density, b_D and b_H are, respectively, the coherent scattering lengths of the deuterated and hydrogenous chain segments, N is the degree of polymerization (number of segments per chain). For uniaxial extension, $S(\mathbf{Q})$ can be expressed as a linear combination of even degree spherical harmonic functions $Y_l^0(\theta, \varphi)$, with Q -dependent expansion coefficients $S_l^0(Q)$, $S(\mathbf{Q}) = \sum_{l:even} S_l^0(Q) Y_l^0(\theta, \varphi)$, with θ being the polar angle and φ the azimuthal angle. Experimentally, the coefficients $S_l^0(Q)$ can be obtained from weighted angular integrals of the SANS spectra, $S_l^0(Q) = \frac{1}{2} \int_0^\pi I_{xz}(Q, \theta) Y_l^0(\theta) \sin\theta d\theta / \lim_{Q \rightarrow 0} I_{iso}(Q)$. Here, $I_{xz}(Q, \theta)$ is the intensity measured on the two-dimensional (2D) detector plane (xz plane) and $\lim_{Q \rightarrow 0} I_{iso}(Q)$ is the zero-angle scattering of the isotropic sample. The previous analysis by Lam et al.⁹⁸ demonstrates

that the tensile stress ($\sigma_{zz} - \sigma_{xx}$) of Gaussian chains is determined by the twopoint spatial correlations associated with only the spherical harmonic function $Y_2^0(\theta, \varphi)$: ($\sigma_{zz} - \sigma_{xx}$) = $2\nu\beta^2 k_B T [\frac{1}{\sqrt{5}} \int_0^\infty 4\pi r^2 \psi_2^0(r) r^2 dr]$, where ν is the number density of “load-bearing strands,” $\beta^2 \equiv 3/2sb^2$, with s being the number of beads in the strand and b the bead size, and $\psi_2^0(r) = \frac{1}{4\pi} \int \psi(\mathbf{r}) Y_2^0(\theta, \varphi) d\theta d\varphi$ is the leading anisotropic expansion coefficient of the strand configuration distribution function $\psi(\mathbf{r})$. While a direct connection between $S_2^0(Q)$ and stress is yet to be established, in the small-strain limit, it can be shown with the affine deformation model that the molecular strain is approximately proportional to the peak amplitude of the $S_2^0(Q)$. In other words, the structural anisotropy determined from the ZAC SANS experiments should reflect the contribution of the polymer matrix to the total stress.

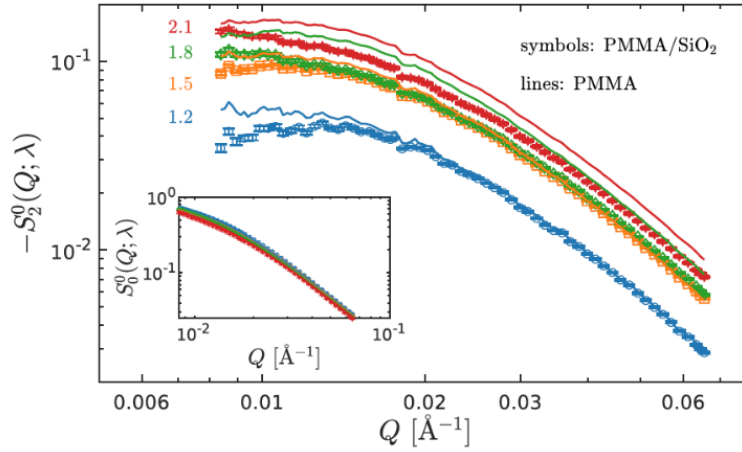


Figure 4.5 Spherical harmonic expansion coefficients. Here, $S_0^0(Q)$ and $S_2^0(Q)$ are, respectively, the isotropic and leading anisotropic expansion coefficients of the structure factor $S(Q)$. Symbols: PMMA/SiO₂. Lines: PMMA.

Fig. 4.5 shows the spherical harmonic expansion analysis of the PNC (symbols) and the pristine polymer (lines). On the one hand, the leading anisotropic terms $S_2^0(Q; \lambda)$ of both the pristine polymer and the PNC increase with the stretching ratio λ in the Q range of 0.008– 0.065 \AA^{-1} . On the other hand, the isotropic coefficients $S_0^0(Q; \lambda)$ of the pristine polymer

and the PNC (inset of **Fig. 4.5**) exhibit no discernible difference across all Q s. This observation underscores the advantage of the spherical harmonic expansion technique over the traditional analysis of scattering intensities in parallel and perpendicular directions, where the contributions from isotropic and anisotropic coefficients are not isolated. Note that the previous SANS experiment⁶⁰ relied heavily on model assumptions to characterize polymer microscopic deformation, producing large uncertainties especially under imperfect ZAC condition. From this perspective, the separation of isotropic and anisotropic spectral components by the SHE analysis permits a quantitative examination of the molecular overstraining idea. Remarkably, the $S_2^0(Q; \lambda)$ of the PMMA/SiO₂ is almost identical to that of the pristine PMMA across the whole Q range at $\lambda = 1.2$ and 1.5 . Moreover, at larger deformation of $\lambda = 1.8$ and 2.1 , the magnitude of $S_2^0(Q; \lambda)$ of the PNC appears to be slightly smaller than the pristine polymer, implying the presence of NPs reduces the average deformation of the polymer matrix rather than amplifying it. By contrast, the stress in PMMA/SiO₂ is approximately 100% (at $\lambda \rightarrow 1.2$) to 23% (at $\lambda = 2.1$) higher than that in the PMMA. In other words, a naïve application of the strain amplification concept should predict significantly higher structural anisotropy, which we clearly do not observe in the SANS experiments.

The lack of increased structural anisotropy from the SANS measurements and the significant mechanical enhancement in both the linear and nonlinear rheological regimes beg an explanation: where does the extra stress come from? It was previously suggested that direct filler-filler interactions are the main cause for such a phenomenon^{29, 48}. To critically test this hypothesis, we proceeded to perform stress relaxation experiments. Because of the slow nature of particle Brownian motions⁸⁹, PNCs with an extended particle network should exhibit a two-step relaxation with a long tail in the relaxation modulus⁹⁹. Nevertheless, a quantitative

prediction is not possible at this moment, due to the lack of information on particle distribution as well as a feasible theoretical model.

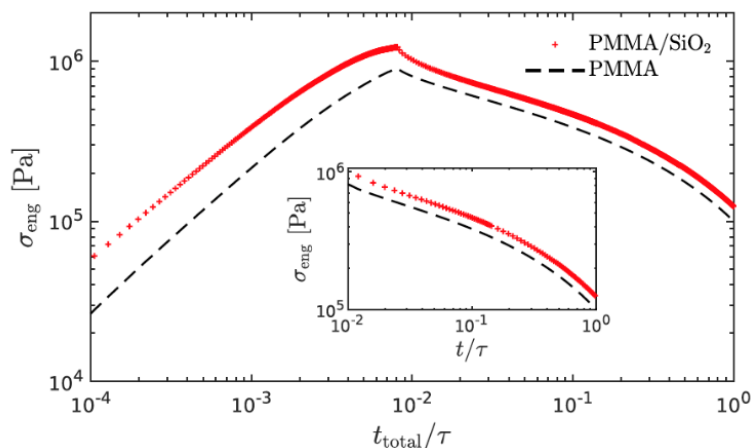


Figure 4.6 Evolution of engineering stress σ_{eng} of PMMA (lines) and PMMA-SiO₂ (symbols) during a step uniaxial extension performed with $\dot{\epsilon} = 0.01 \text{ s}^{-1}$ at T=423 K and the subsequent stress relaxation at $\lambda = 1.8$. The time t is normalized by the terminal relaxation time τ of the pristine PMMA. Inset: engineering stress during relaxation.

Fig. 4.6 shows the evolution of engineering stress in PMMA (dashed line) and PMMA/SiO₂ (red crosses) during and after a step deformation of $\lambda = 1.8$. Because of the presence of nanoparticles, the stress of PMMA/SiO₂ is about 30% higher than that of PMMA. However, contrary to the phenomenology of a two-step relaxation in PNCs with nanoparticle network, there is no sharp drop of stress in PMMA/SiO₂ during the initial phase of relaxation (inset of **Fig. 4.6**) or a slowly decaying tail in the long-time limit. In fact, as shown by the inset of **Fig. 4.6**, the stress relaxation curves of PMMA and PMMA/SiO₂ are parallel to each other. These features indicate an absence of noticeable stress contribution from the nanoparticle-nanoparticle interactions in the PMMA/SiO₂—a conclusion that is consistent with the SAXS and linear viscoelastic measurements, where no signs of a nanoparticle network are found.

4.3.1.4 Polymer Anisotropy under Stress Relaxation

What about the polymer structural anisotropy during stress relaxation? We further performed SANS measurements and analyzed the spectra at different elapsed time, $t =$

$0\tau, 0.01\tau, 0.03\tau, 0.1\tau, 0.3\tau,$ and 1τ during the stress relaxation at $\lambda = 1.8$, where τ is the terminal relaxation time of the pristine PMMA estimated from the low-frequency crossover of the storage and loss moduli. The inset of **Fig. 4.7** presents the normalized anisotropic coefficients $S_2^0(Q; t)/S_2^0(Q; 0)$ of the PNCs (symbols) and the pristine polymer (lines) during the relaxation. Similar to the results of continuous extension, the normalized structural anisotropy of the two samples is almost identical over a length scale from $Q = 0.008 \text{ \AA}^{-1} = 1/(125 \text{ \AA}) \sim R_g^{-1}$ (inverse of radius of gyration) to $Q = 0.065 \text{ \AA}^{-1} = 1/(15.4 \text{ \AA}) \sim l_K^{-1}$ (inverse of Kuhn length) and a time scale up to $\sim\tau$. Furthermore, the previous reported scaling relation for anisotropy relaxation (based on polystyrene and coarse-grain MD simulations) holds true for both the pristine PMMA and PMMA/SiO₂ (**Fig. 4.7**)⁹⁸, $S_2^0(Q; t)/S_2^0(Q; 0) \approx \exp[-(\Gamma t)^{1/2}]$, where the characteristic decay rate $\Gamma \propto QR_g/\tau$. Evidently, the inclusion of NPs does not affect the slow relaxation dynamics of the deformed polymer matrix.

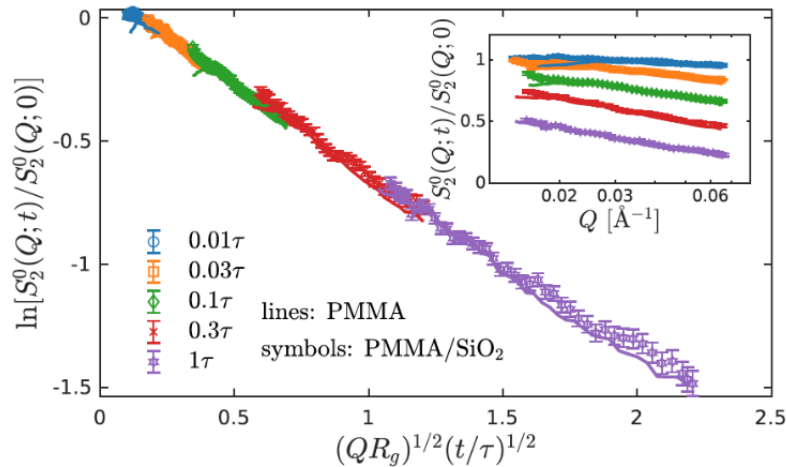


Figure 4.7 PMMA and PMMA/SiO₂ exhibit identical scaling behavior for anisotropy relaxation. $S_2^0(Q; 0)$ is the expansion coefficient immediately after the step deformation, whereas $S_2^0(Q; t)$ is the coefficient during the stress relaxation. Inset: spatial dependence of the normalized expansion coefficient $S_2^0(Q; t)/S_2^0(Q; 0)$ during the relaxation.

To recap the preceding analysis, our SANS and rheological measurements unambiguously reveal substantial mechanical reinforcement with no enhanced polymer structural

anisotropy during both uniaxial extension and subsequent relaxation. The absence of strain amplification in the matrix polymer is especially intriguing, given the prevailing viewpoint that the matrix polymer should undergo larger deformation to fulfill the macroscopic deformation due to the presence of nondeformable inorganic particles¹⁰⁰. Moreover, the rheological signatures of the relaxation experiments rule out NP-NP interactions as the mechanism for reinforcement. These observations significantly challenge the current molecular understanding of the mechanical reinforcement of PNCs and call for a different explanation of the role of NPs in modifying the deformation of the matrix polymer.

4.3.1.5 Hydrodynamic Effect in Polymer Nanocomposites

According to the classical hydrodynamic theory for dilute particle suspensions^{38, 101-104}, the particle distorts the strain field surrounding the nanoparticles, and such an effect propagates far into the bulk, over a distance of a few times of the size of the particle. More importantly, the net disturbance of the particle to the strain of the matrix polymer is zero across the matrix. In other words, the hydrodynamic reinforcement theory implies an enhanced mechanical response from the resistance of particles to the straining field with zero average disturbance of the velocity gradient or strain field in the bulk. Our experiments, on the other hand, show enhanced stress governed by polymer matrix but no increase of polymer structural anisotropy, in excellent agreement with this picture. Thus, the classical hydrodynamic theory, at the leading order, explains the molecular mechanism of mechanical reinforcement in PNCs—a redistribution of the stress and strain field over a large area surrounding the nanoparticles rather than strain amplification of the entire matrix polymer. The particle-induced redistribution of the stress and strain also leads to an enhancement in the mechanical properties. Nevertheless, a rigorous calculation on the influence of nanoparticles to the stress and strain field in concentrated PNCs is

challenging, due to the complex geometry and the multiscale coupling^{105, 106} of the polymer-nanoparticle and nanoparticle-nanoparticle interactions, such as the interplay between polymer adsorption, interfacial entanglement, and hydrodynamic force. The detail of strain field distribution requires further investigation.

As far as the scattering problem is concerned, a precise calculation appears to be difficult even for this simple case. However, for a homogeneous system in the small strain limit, the influence of an elastic deformation on the pair distribution function $g(\mathbf{r})$ can be formally described by a multipole expansion^{107, 108} as $g(\mathbf{r}) - g(r) = \{ -[(\mathbf{E} - \mathbf{I}) \cdot \mathbf{r}] \cdot \nabla \} g(r) + \frac{1}{2} \{ -[(\mathbf{E} - \mathbf{I}) \cdot \mathbf{r}] \cdot \nabla \}^2 g(r) + \dots$, where \mathbf{E} is the deformation gradient tensor and \mathbf{I} is the isotropic tensor. Suppose the particle size is relatively large and we are probing the structure at relatively high Q , it can be argued that in this limit the anisotropic pair correlation functions can be averaged in different fluid elements. Truncating the expansion at the first order, it is straightforward to show that the average deformed single-chain structure is indeed not affected by the presence of particles. While our PNC system cannot be regarded as a dilute suspension of silica particles, the results from SANS and rheological experiments suggest that the underlying physical picture is strikingly similar. It is worth noting that the evolutions of both the mechanical signal and structural anisotropy parallel those of the pristine polymer during stress relaxation, which is consistent with the current interpretation. Lastly, we point out that our explanation does not necessarily exclude potentially highly localized responses from interfacial polymers in the vicinity of the nanoparticles^{23, 109, 110}.

4.3.2 Polystyrene/SiO₂ System with Aggregated Nanoparticles

4.3.2.1 Zero Contrast Matching

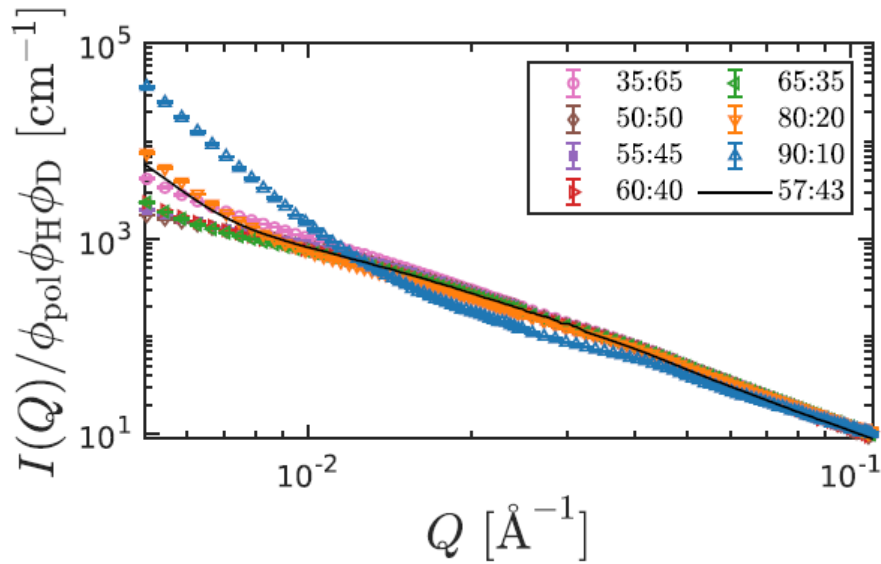


Figure 4.8 Normalized scattering intensity $I(Q)/\phi_{pol}\phi_H\phi_D$ of mixtures of H⁸-PS and D⁸-PS at different H/D ratios. Here, $\phi_{pol} = 1 - \phi_{NP}$ is the volume fraction of the polymer, and ϕ_H and ϕ_D are the volume fractions of the hydrogenous and deuterated PSs, respectively.

To identify the zero average contrast (ZAC) point, we measured the scattering of PNCs with a fixed NP loading and varying H/D ratios in the polymer phase. **Fig. 4.8** shows the SANS measurements of isotropic PS/SiO₂ nanocomposites with H/D ratios from 0.35/0.65 to 0.90/0.10 and their comparison to the neat polymer. Note that the H/D ratio from 0.35/0.65 to 0.90/0.10 covers an average SLD, $\rho_{<P>} = \phi_D\rho_D + \phi_H\rho_H$, from $4.48 \times 10^{-6} \text{ \AA}^{-2}$ to $1.83 \times 10^{-6} \text{ \AA}^{-2}$, while the $\rho_{NP} \sim 3.48 \times 10^{-6} \text{ \AA}^{-2}$ according to previous publications. Thus, an ideal ZAC condition should be identified. On the other hand, all PS/SiO₂ show clear upturn at $q < 0.01 \text{ \AA}^{-1}$, deviating from the scattering of the neat polymer, highlighting the challenge of achieving an ideal zero average contrast condition for PNCs. According to Pyckhout-Hintzen and co-workers¹¹¹, the NP phase in PNCs should be modelled with a two-component system (instead of one) if NP has fractal structure or the PNC has a distinct surface polymer packing from the bulk. Consequently,

simultaneous compositional matching and phase matching should be fulfilled in order to obtain the ZAC, which is not possible through adjusting the H/D ratio of the matrix polymer. As a result, the scattering from the NP phase cannot be fully screened as observed in PS/SiO₂ nanocomposites. Experimentally, contrast matching between PS/SiO₂ and neat PS can only be partially achieved at high q ($q > 0.01 \text{ \AA}^{-1}$) at H/D = 0.55/0.45 and 0.57/0.43.

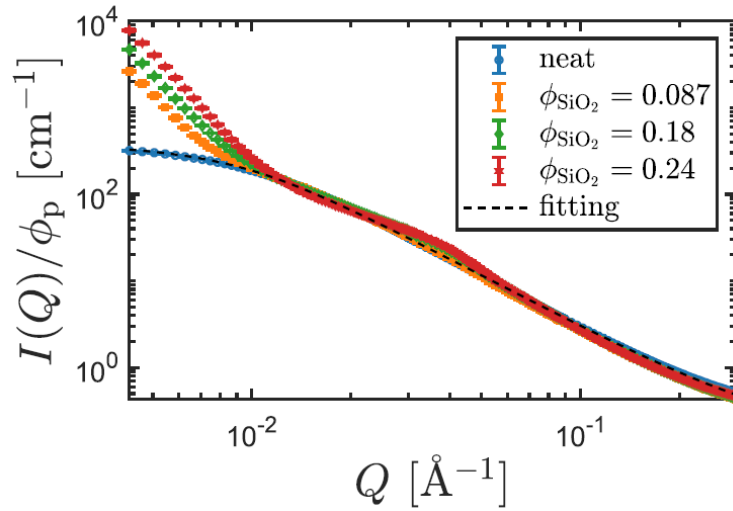


Figure 4.9 Polymer fraction normalized intensities of neat polymer and PNCs by SANS measurement

Fig. 4.9 presents $I_{tot}(q)/(\phi_p)$ of PS8.7, PS18, PS24, and the matrix polymer ($\phi_p = 1.0$) with H/D ratio of 0.57/0.43 in the polymer phase. The scattering of PS8.7 overlaps nicely with the neat matrix polymer at $q > 0.01 \text{ \AA}^{-1}$, implying negligible scattering contribution from the NP phase at intermediate and high q . The strong upturn at $q < 0.01 \text{ \AA}^{-1}$ implies the presence of excess scattering of the NP phase at low q , even though the average SLD of the polymer phase matches with the SiO₂. Interestingly, a shoulder peak appears at $q \sim 0.04 \text{ \AA}^{-1}$ in PS18 and PS24 but not in PS8.7. The higher the NP loading, the more pronounced the shoulder peak, implying a NP origin of the shoulder peak.

4.3.2.2 Small-angle X-ray Scattering, Linear Rheology and Stress Relaxation

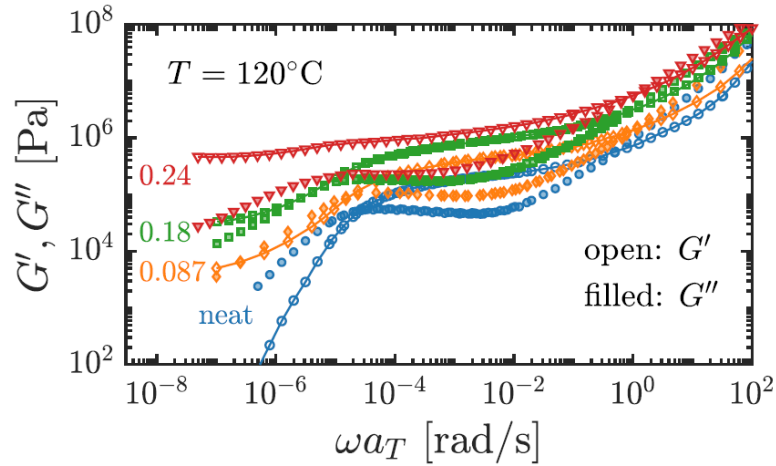


Figure 4.10 Master curves of neat polymer, PS8.7, PS18 and PS24 with a reference temperature of 120 °C

Fig 4.10 presents the linear viscoelastic master curves of PNCs as well as the neat matrix polymer at a reference temperature $T = 120$ °C, where $G'(\omega)$ is the storage modulus and $G''(\omega)$ is the loss modulus with ω being the angular frequency and a_T being the shift factor. Two important features are worth noting: (i) PNCs exhibit a significantly higher plateau modulus, $G_p(\phi_{NP})$, than the neat matrix polymer. The plateau modulus is defined by the storage modulus at the frequency where the loss factor, $\tan\delta = G''(\omega)/G'(\omega)$, shows a minimum. (ii) No terminal regions are observed for PNCs. A second modulus plateau at the low-frequency region, G_{lp} , are well resolved for all PNCs. Thus, strong mechanical reinforcement is found in PNCs at all frequencies. For PS/SiO₂ nanocomposites in **Fig. 4.10**, the values of $\tan\delta$ of all PNCs remain almost identical with the neat matrix polymer in the intermediate frequency region, supporting the hydrodynamic effect of NPs to the mechanical reinforcement of PNCs at the rubbery plateau region. Both the Einstein-Smallwood and Guth-Gold equations fall short to account for the mechanical reinforcement of PNCs at high ϕ_{NP} , implying the presence of NP clusters or NP networks that

promote the effective loading of NPs. On the other hand, the emergence of low-frequency plateau has often been attributed to the NP network or polymer bridge network.

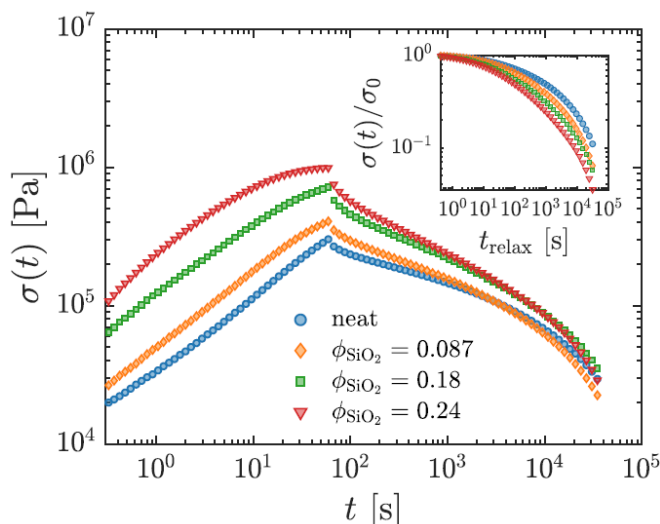


Figure 4.11 Stress relaxation curves of neat polymer, PS8.7, PS18 and PS24 at $\lambda = 1.8$ for a relaxation time of 1τ

Fig. 4.11 shows the stress-time curves of PNCs and the neat matrix polymer as well as the subsequent stress relaxation at an elongation ratio $\lambda = 1.8$ (Hencky strain $\varepsilon = 0.6$). During deformation, all PNCs show much higher stress than the neat polymer. The higher the NP loading, the larger the tensile stress. This is consistent with the observations from the linear viscoelastic measurements, where $G_p(\phi_{NP})$ increases strongly with ϕ_{NP} . Interestingly, the deformed neat polymer can retain the stress to a much longer time than the PNCs during stress relaxation, indicating a much faster stress relaxation of PNCs. The speedup in relaxation dynamics of deformed PNCs can be better visualized after normalization, $\sigma_{eng}(t_{relax})/\sigma_0$, as shown in the inset of Fig. 3 with σ_0 being the engineering stress at the onset of stress relaxation and t_{relax} the time elapsed during stress relaxation. Another important observation in Fig. 3 is the almost complete relaxation within 1τ for all deformed PNCs, suggesting the absence of long-lived relaxation modes of these PS/SiO₂ nanocomposites. Given the emergence of the second modulus plateau emerges at long time scale (low frequency region) of these PNCs in the linear viscoelastic

measurements, the absence of long-lived relaxation mode implies the large deformation breaks up of the NP network. Thus, the rheological measurements suggest the NP network contribute negligibly to the overall stress of the PNCs under large deformation and the stress relaxation of these deformed PNCs is dominated by polymer dynamics.

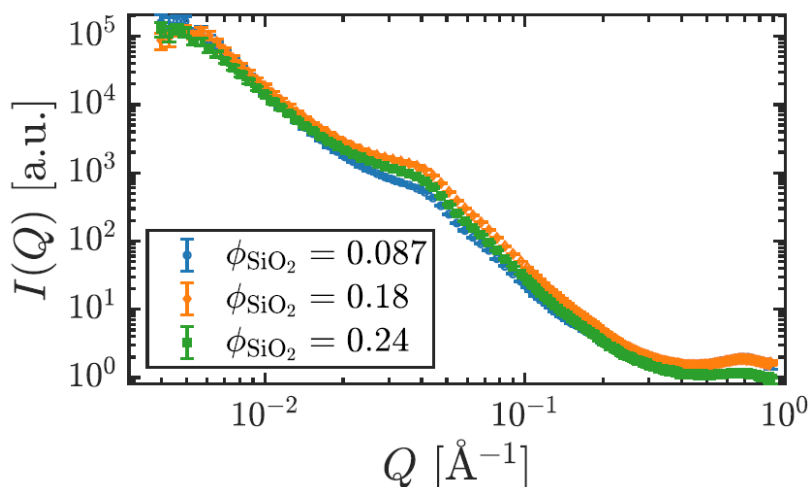


Figure 4.12 Scattering intensities of PS8.7, PS18, and PS24 by small-angle x-ray scattering

Figure 4.12 shows the scattering intensity, $I(q)$, from SAXS measurements of PS8.7, PS18, and PS24. A strong upturn in the scattering at $q < 0.02 \text{ \AA}^{-1}$ region indicates the presence of NP aggregates, consistent with the weak polymer-nanoparticle interactions in PS/SiO₂ nanocomposites and the emergence of the low-frequency modulus plateau in the linear viscoelastic measurements. Thus, the PS/SiO₂ nanocomposites can serve as model systems to unravel the influence of NPs to the structure and dynamics of PNCs with NP networks, which is an important characteristic of industrial relevant PNCs.

Upon external deformation, the structural anisotropy of NP phase builds up. SAXS can well resolve the structural anisotropy of NPs in deformed PNCs. **Fig. 4.13** presents the SAXS pattern of PNCs before and after deformation at $\lambda = 1.8$ as well as the evolution of the microstructure during stress relaxation. The scattering pattern remain almost identical during stress relaxation from $t_{relax} = 0$ to $t_{relax} = 1 \tau$, suggesting negligible changes in the structural

anisotropy of NP phases. The observation of the strong stress relaxation and the negligible structural anisotropy of the NP phases indicates the polymer deformation dominates the macroscopic stress of PNCs.

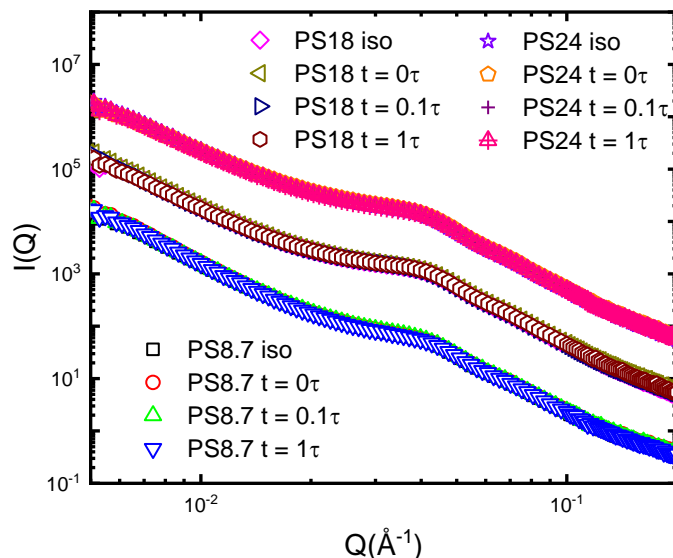


Figure 4.13 X-ray scattering intensities of PS8.7, PS18, and PS24 with isotropic state (iso), and stretched at an elongation ratio of $\lambda = 1.8$ followed with different time after relaxation ($t = 0\tau$, 0.1τ , 1τ where τ is the relaxation time of the neat polymers).

4.3.2.3 Neutron Scattering of Deformed Polymer Nanocomposites

SANS is by far one of the best techniques that enable a quantification of polymer conformation in PNCs. In deformed PNCs, the structural anisotropy of the matrix polymer can be obtained from analyzing the structural anisotropy of the single chain structure factor. **Fig. 4.14** presents the 2D SANS patterns of deformed PS0 (matrix polymer), PS8.7, PS18, and PS24 during stress relaxation at $t_{relax} = 0\tau$, 0.1τ , and 1.0τ . Important features are worth noting from the 2D SANS spectra: (i) Strong structural anisotropy builds up in all samples upon deformation. (ii) The structural anisotropy reduces significantly with t_{relax} , consistent with the large drop of tensile stress upon stress relaxation. (iii) For a given t_{relax} such as $t_{relax} = 0\tau$ and 0.1τ , all PNCs exhibit slightly similar structural anisotropy than the neat matrix polymer, despite the much larger macroscopic stress of the PNCs than the neat polymer. We note that a similar structural anisotropy

between deformed PS/SiO₂ nanocomposites and deformed neat matrix polymer has been observed before. However, none of those work focus on the stress relaxation dynamics. Moreover, the present investigation relies on SHE analysis to quantify the spatial-temporal behavior of the structural anisotropy during stress relaxation of highly filled PNCs with NP networks that distinguish the current study from previous SANS measurements.

4.3.2.4 The Molecular Mechanism of the High Stress of PNCs at Large Deformation

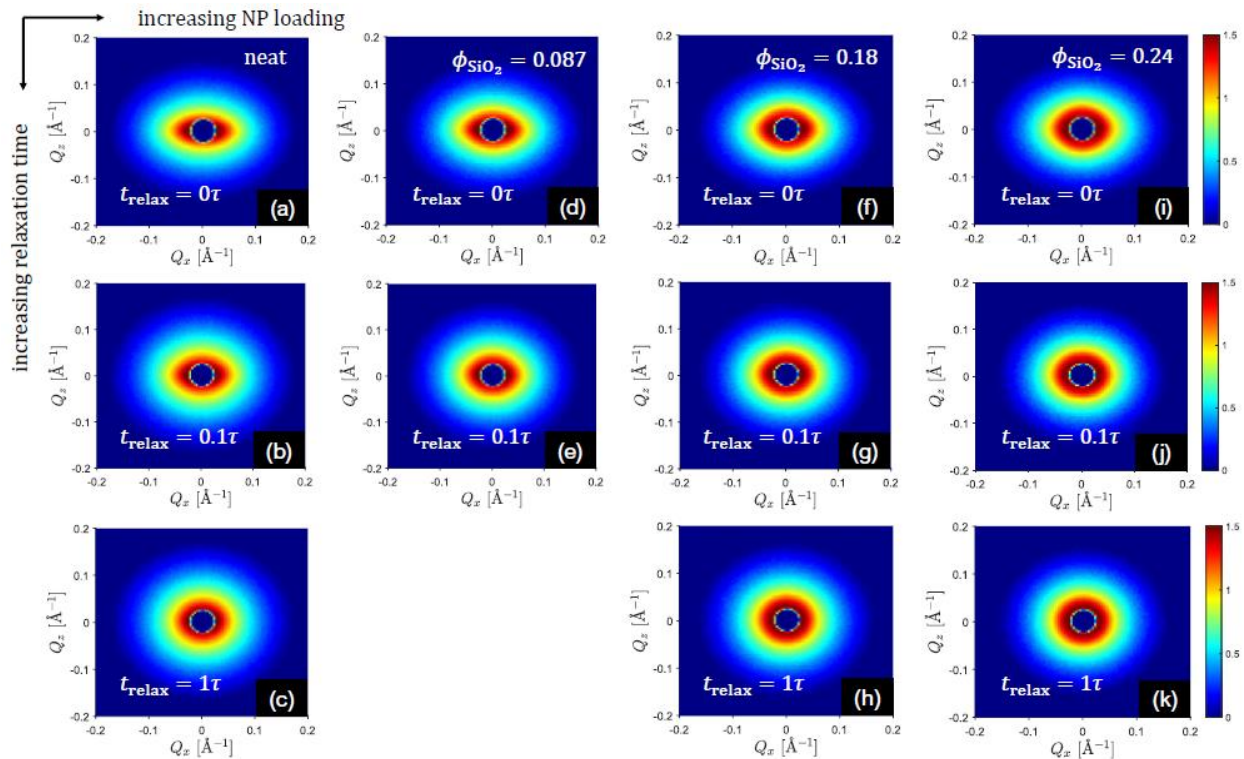


Figure 4.14 The 2D SANS spectra of PS8.7, PS18, and PS24 at different stages of stress relaxation.

Strong mechanical enhancement was observed in PNCs both in the linear response region and at large deformation, as shown in **Fig. 4.10** and **Fig. 4.11**. Two types of contributions are typically considered for the high mechanical strength of PNCs: the molecular overstraining and the elastic deformation of the NP-NP network, both of which can be analyzed through the small-angle scattering.

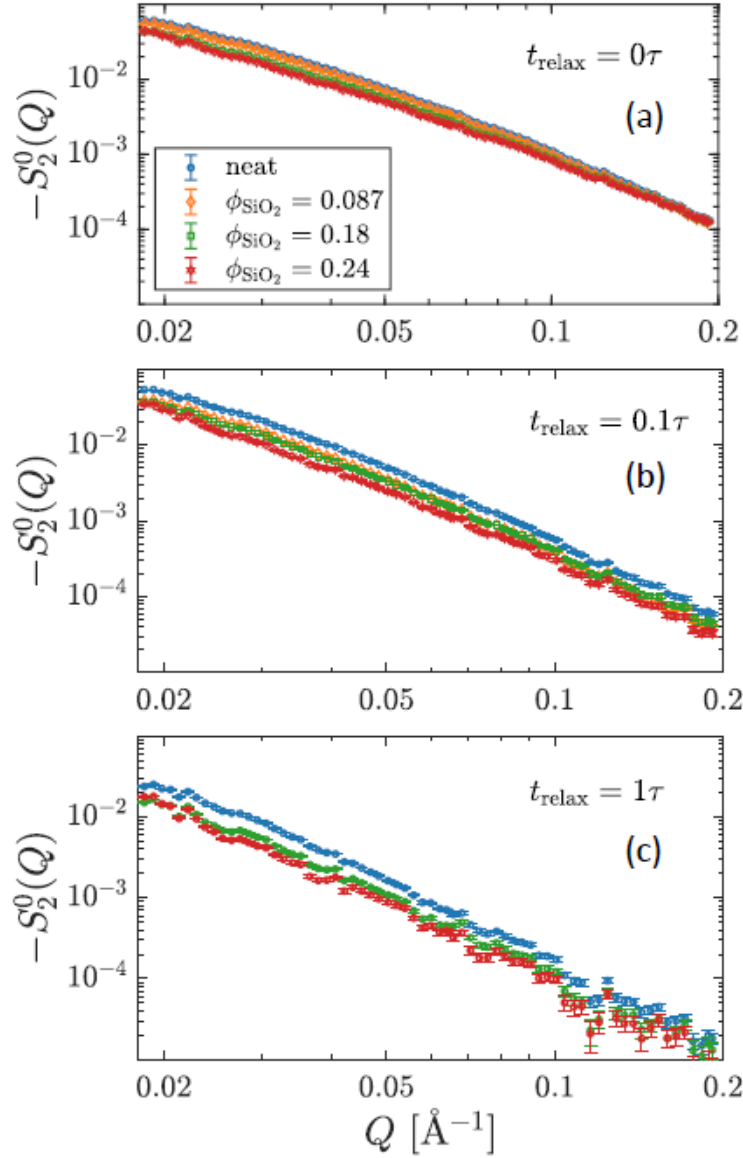


Figure 4.15 $-S_2^0(q)$ values of PNCs of different loading at different stages of relaxation: **(a)** $t_{relax} = 0 \tau$, **(b)** $t_{relax} = 0.1 \tau$ and **(c)** $t_{relax} = 1 \tau$

Fig. 4.15 shows the $-S_2^0(q)$ of PS0, PS8.7, PS18, and PS24 from SANS during stress relaxation at $t_{relax} = 0 \tau$, 0.1τ , and 1.0τ . An important observation is that PNCs exhibit significant smaller $-S_2^0(q)$ than the neat polymer at all qs . Remarkably, the $-S_2^0(Q)$ of PS24 is $\sim 30\%$ less than the neat polymer, implying a strong hindering of the polymer deformation due to the presence of NPs. The strong reduction in the $-S_2^0(Q)$ values is intriguing and has not been

observed before, especially for PNCs with high NP loadings. For instance, the tensile stresses of PS0, PS8.7, PS18, and PS24 at $\lambda = 1.8$ & $t_{relax} = 0 \tau$ are 1.27, 2.5, and 3.3 times higher than the neat polymer, respectively. Thus, one should anticipate a much stronger structural anisotropy from PNCs than the neat matrix polymer. According to the classical viewpoint of the strain amplification of PNCs, an average of at least $1 + 2.5\phi_{NP}$ time enhancement in polymer deformation is anticipated. For $\phi_{NP} = 18\%$ and 24% , the structural anisotropy should be enhanced by a factor of $X = 1.45$ and $X = 1.6$. Hence, the observations of similar or smaller molecular overstraining in PNCs than the neat polymer clearly rule out the molecular overstraining as a major mechanism of the mechanical reinforcement of PNCs.

The concurrence of the absence of molecular overstraining and the strong enhancement in the macroscopic stress imposes a big puzzle on the role of NPs to the mechanical reinforcement of PNCs. In PMMA/SiO₂ systems, we discussed that hydrodynamic effect of NPs plays a crucial role for the high mechanical strength of PNCs for PNCs without NP networks. The hydrodynamic effect of NPs should make its contribution to the mechanical enhancement of PNCs at high loadings and might partially explain the origin of the high stress with no enhanced polymer anisotropy. However, for PS nanocomposites with strong NP network, one also need to quantify the stress contribution from the NP network before a clear understanding can be achieved in terms of the hydrodynamic effect to the mechanical reinforcement of highly filled PNCs.

To unravel the contributions of the matrix polymer and the NP network to the high mechanical strength of PNCs, we turn to detailed analyses of the SANS and SAXS spectra of PNCs at different stages of relaxation. **Fig. 4.16** presents the normalized $S_2^0(q; t_{relax})/S_2^0(q; 0)$, of PS18 and PS24 and the neat matrix polymer at $t_{relax} = 0.1 \tau$ and 1.0τ . Compared with the

neat matrix polymer, the PNC exhibits a much faster reduction in $S_2^0(q; t_{relax})/S_2^0(q; 0)$ at all q s. Given the strong correlation between the structural anisotropy and the macroscopic stress of polymers, the stronger relaxation of structural anisotropy in the PNC partial explains the faster stress relaxation of PNCs than the matrix polymer.

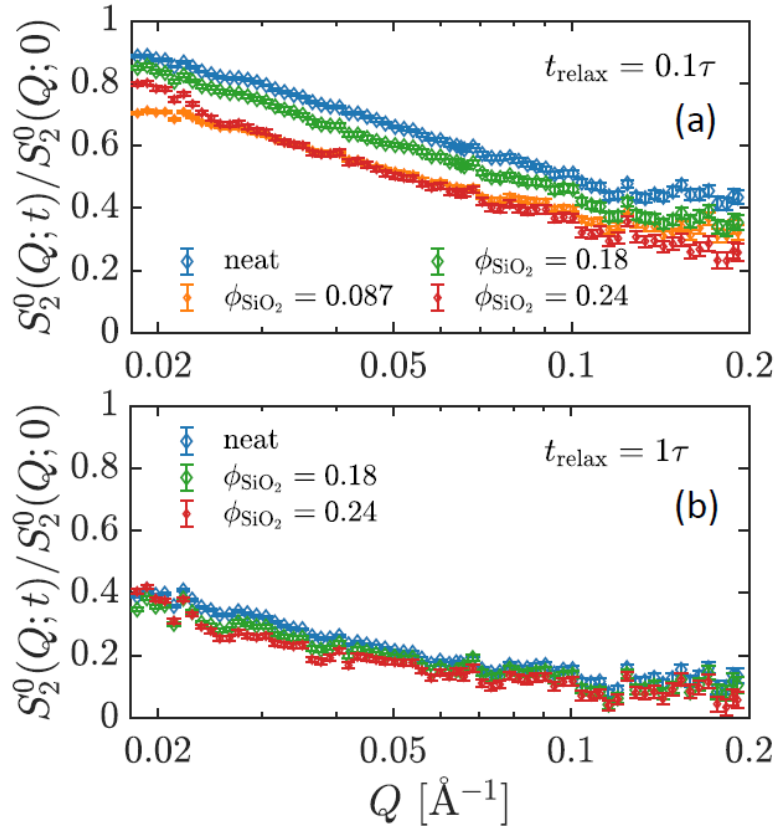


Figure 4.16 Normalized $S_2^0(q; t_{relax})/S_2^0(q; 0)$ of neat polymer, PS18 and PS24 at **(a)** $t_{relax} = 0.1 \tau$ and **(b)** $t_{relax} = 1.0 \tau$

On the other hand, **Fig. 4.13** already demonstrates that the nanoparticle microstructure remains almost no changes during the whole stress relaxation process regardless of the loadings of NPs, indicating almost identical contributions of NP network during the whole stress relaxation process. Experimentally, less than 10% of the tensile stress remains at $t_{relax} = 1.0 \tau$ for all PNCs, further confirming a negligible stress contribution of the NP network at large deformation. The SAXS analyses are consistent with the rheological analysis that concludes a breakup of the NP network at large deformation in highly filled PNCs. It is worth emphasizing

that the deformation of the NP network and the contributions of the NP-NP interactions have been previously attributed to the high mechanical strength of PNCs⁵². However, the stress relaxation experiments and the SAXS analyses suggest a negligible effect of the NP network to the high mechanical stress of the PS/SiO₂. Therefore, through the combination of SANS, SAXS, and rheology, we can conclude that the NP network alters the deformation field in the matrix polymer phase, i.e., the hydrodynamic effect of NPs, leading to the high mechanical strength of PNCs at large deformation.

4.4 Conclusions

The microscopic origin of mechanical reinforcement in deformed polymer nanocomposite melts is investigated through a combination of small-angle neutron scattering and rheology. In contrast to the prevailing viewpoint of molecular overstraining, strain amplification is not observed by SANS. Similar to the classical picture of Einstein and Smallwood for dilute suspensions, the enhanced mechanical response originates from the resistance of particles to the straining field, whereas the average disturbance of the deformation gradient in bulk is nearly zero. In the PNC systems with aggregated nanoparticles, polymer anisotropy in the PNCs shows a smaller magnitude and relaxes faster than that in the PNCs. This result further proves the absence of molecular strain amplification. Possible causes for lower polymer anisotropy are the presence of the occluded polymers in the nanoparticle aggregates and/or the hindered polymer deformation in the interfacial region. The strong nonlinear deformation induced by the hydrodynamic effect can account for the faster relaxation in the PNCs.

CHAPTER 5 THE ROLE OF INTERFACIAL POLYMERS FOR MECHANICAL REINFORCEMENT OF POLYMER NANOCOMPOSITES AT LARGE DEFORMATION

5.1 Introduction

In the previous chapters, we have investigated the roles of nanoparticle (NPs) rearrangement and polymer deformation for mechanical reinforcement of polymer nanocomposites (PNCs) at large deformation. The contribution from the nanoparticles to the reinforcement is negligible except in the flow regime where $Wi \ll 1$. We also recognize the importance of the hydrodynamic effect of the nanoparticles on polymer deformation and thus mechanical reinforcement. In this chapter, we go beyond the hydrodynamic effect to systematically characterize the influence of NPs to the nonlinear stress-strain responses of PNCs at large deformation. Furthermore, we evaluate the roles of interfacial and bridge polymers, which are often regarded as important ingredients in the mechanical reinforcement of PNCs.

5.2 Materials and Methods

In this chapter, we address the salient features of stress-strain response of PNCs with well-dispersed nanoparticles, with special focus on the contribution of bound polymers to the mechanical enhancement of PNCs. To suppress the influence of strong NP-NP interaction while maintaining the contributions of bound polymers, we focus on PNCs with intermediate nanoparticle loadings. With varying polymer molecular weights (M_w) and the nanoparticle sizes, our experimental design covers PNCs with different surface conditions from negligible amount of bound polymer to heavily bridging. Three types of poly(2-vinyl pyridine) (P2VP, Scientific Polymer Products, Inc., polydispersity ≤ 1.1) with weight-average M_w of 100, 200, and 400 kg/mol and three types of silica nanoparticles of radius of $R_{NP} = 12 \text{ nm}$, 9.5 nm , and 23 nm

synthesized either by Stöber method at MSU lab or provided by Nissan Chemical America Corporation. Details of the nanoparticle synthesis, PNCs preparation, and their characterizations are presented in the Materials and Methods section in Chapter 2. A summary of the prepared samples is presented in **Table 5.1**, where the sample name is an abbreviation and represents the matrix polymer, polymer molecular weight, the nanoparticle loading, and the size of nanoparticles. For instance, P2VP100k-4v%R12 represents P2VP/SiO₂ with polymer Mw of 100 kg/mol, R_{NP} of 12 nm, and nanoparticle loading of 4 vol%.

Table 5.1 Polymer and nanoparticle information of PNC samples

Sample Name	M_w (kg/mol)	φ_{NP}	R_g (nm)	R_{NP} (nm)	d_{cc} (nm) (SAXS)	d_{IPS} (nm) (SAXS)	d_{IPS}/R_g
P2VP100k-4v%D24	100	4%	8.70	12	36.2	12.2	1.40
P2VP100k-7v%D24	100	7%	8.70	12	33.9	9.90	1.14
P2VP200k-3v%D19	200	3%	12.3	9.5	33.9	14.9	1.21
P2VP200k-7v%D19	200	7%	12.3	9.5	32.5	13.5	1.10
P2VP200k-9v%D45	200	9%	12.3	23	99.0	53.0	4.31
P2VP400k-3v%D24	400	3%	17.4	12	32.5	8.50	0.489
P2VP400k-8v%D24	400	8%	17.4	12	34.6	10.6	0.609

5.3 Results and Discussion

5.3.1 Small-angle X-ray Scattering

Fig. 5.1a shows the small-angle x-ray scattering (SAXS) of P2VP200k-3v%R9.5, P2VP200k-7v%R9.5, and P2VP200k-9v%R23. A clear level-off in scattering intensity is observed, indicating the NPs well-dispersed in matrix polymer in these PNCs and being consistent with previous literature reports. Kratky plot, $Q^2I(Q)$ vs Q , is employed to estimate the interparticle center-to-center distance, $d_{cc} = 2\pi/Q^*$ with Q^* being the characteristic wavevector associated with the low Q peak indicated in the inset of **Fig. 5.1a**. The interparticle surface-to-surface distance, d_{IPS} , can then be quantified as $d_{IPS} = d_{cc} - 2R_{NP}$. Similar observations are found for P2VP100k-4v%R12, P2VP100k-7v%R12, P2VP400k-3v%R9.5 and P2VP400k-

8v%R9.5 (**Fig. 5.1b**). **Table 1** summarizes the d_{cc} , d_{IPS} , and d_{IPS}/R_g for all the PNCs. According to previous studies, the d_{IPS}/R_g can serve as a good indicator for polymer bridging. The experiments cover a wide range d_{IPS}/R_g from 0.489 to 4.31, and thus include various polymer bridging conditions that are also supported by the linear rheology measurements.

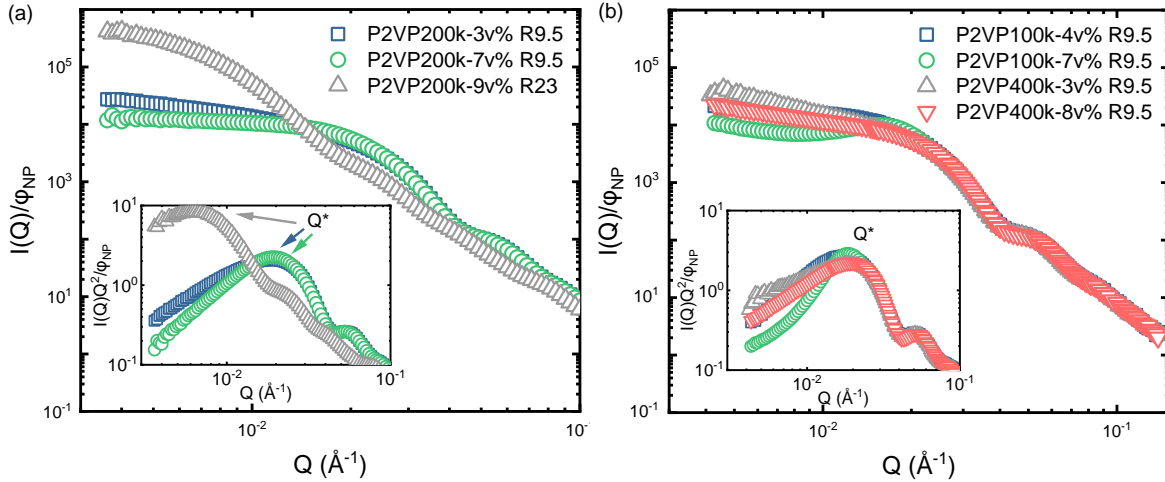


Figure 5.1 The scattering intensity $I(Q)$ normalized by silica volume fraction ϕ_{NP} of (a) P2VP200k/SiO₂ and (b) P2VP100k/SiO₂ and P2VP400k/SiO₂ samples obtained from small-angle x-ray scattering measurements. The insets show Kratky plots for the representative samples.

5.3.2 Small-amplitude Oscillatory Shear

Fig. 5.2a presents the linear viscoelastic spectra master curves of P2VP200K/SiO₂ nanocomposites (symbols) at a reference temperature $T_{ref} = 413\text{ K}$. Comparison with the viscoelastic spectra of the neat matrix polymer P2VP200K (lines, **Fig. 5.2a**), the PNCs all show moderate enhancement in the rubbery plateau at the intermediate frequency region, where the plateau modulus, $G(\phi_{NP})$, of PNCs determined through the storage modulus, $G'(\omega)$, at the minimum of the loss factor, $\tan\delta = \frac{G''(\omega)}{G'(\omega)}$. The inset of **Fig. 5.2a** presents the experiments and their comparison with the Guth-Gold equation, $G(\phi_{NP}) = G(0)X$ with $X = (1 + 2.5\phi_{NP} + 14.1\phi_{NP}^2)$ being the hydrodynamic reinforcement factor. An excellent agreement is found that is consistent with the well-dispersion of NPs in matrix polymers from SAXS measurements and

indicates the hydrodynamic effect of NPs for the mechanical reinforcement at linear response region.

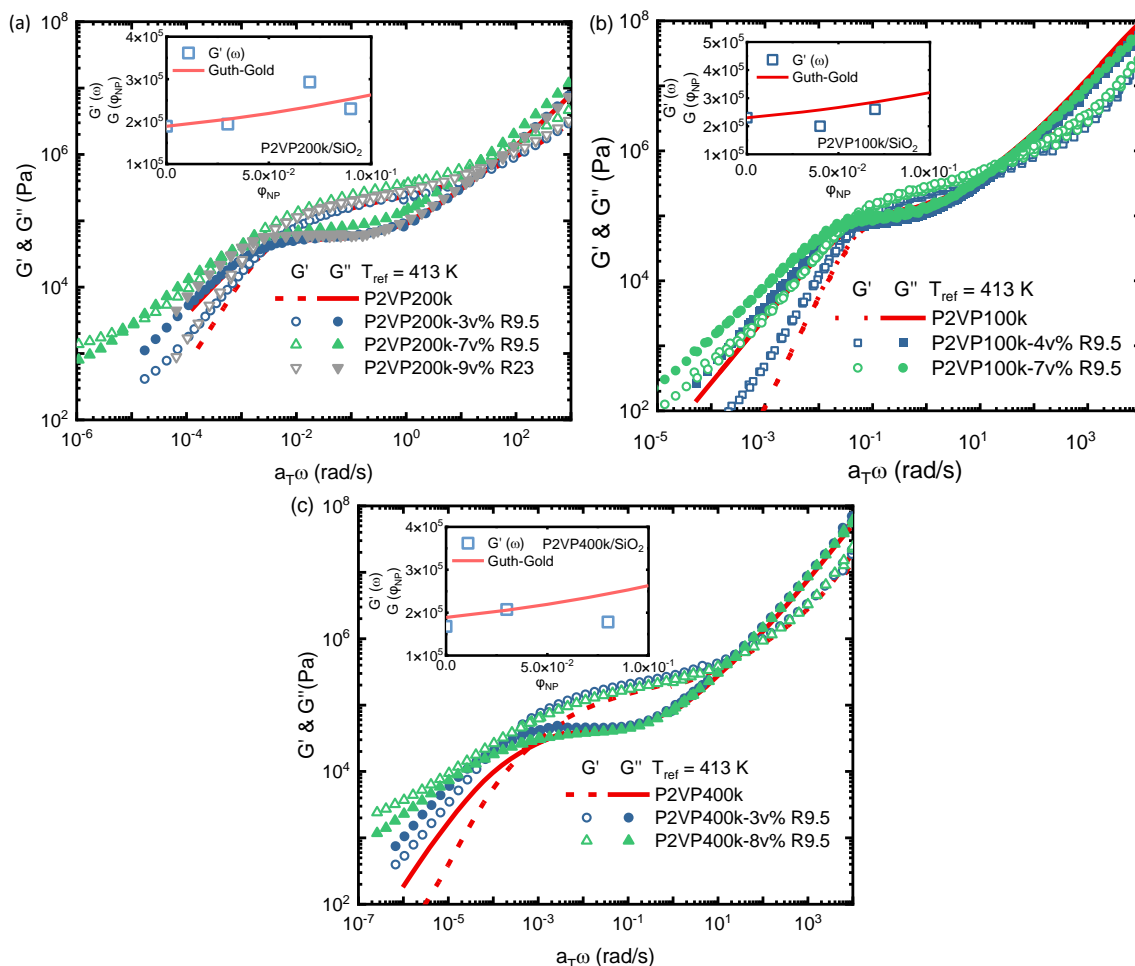


Figure 5.2 Master curves of (a) P2VP200k/SiO₂ (b) P2VP100k/SiO₂ and (c) P2VP400k/SiO₂ samples constructed from the small-amplitude oscillatory shear results by the time-temperature superposition principle (TTSP). The insets show comparisons between plateau moduli and quantifications of hydrodynamic effect by Guth-Gold equation.

Additionally, obvious deviations from $G'(\omega) \sim \omega^2$ and $G''(\omega) \sim \omega^1$ have been observed at the low-frequency region of the viscoelastic spectra, implying the emergence of slow dynamics of PNCs. $G''(\omega) \sim \omega^x$ with $x > 2/3$ is observed for both P2VP200K-3v%R9.5 and P2VP200K-9v%R23, indicating the absence of the NP network through polymer bridging. For P2VP200K-7v%R9.5, a low-frequency plateau is clearly visible, implying the presence of a strong polymer bridging network. These results are consistent with the empirical rule for a lack of polymer

bridging for $d_{IPS}/R_g > 2$ (P2VP200K-3v%R9.5 and P2VP200K-9v%R23) and the emergence of polymer bridging for $d_{IPS}/R_g < 2$ (P2VP200K-7v%R9.5).

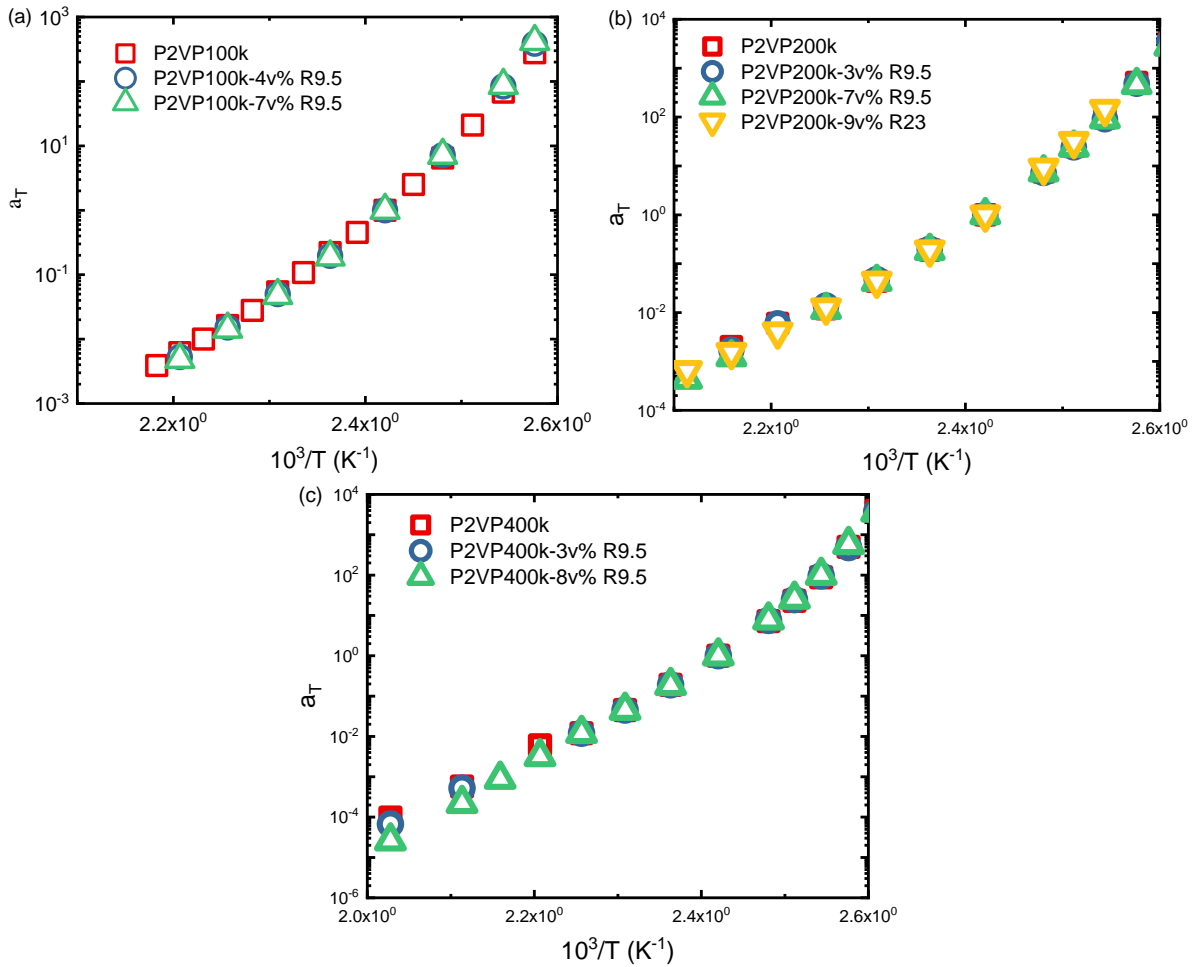


Figure 5.3 Shift factors used to construct the master curves of (a) P2VP100k/SiO₂, (b) P2VP100k/SiO₂, and (c) P2VP100k/SiO₂.

Similar results have been observed for P2VP100K/SiO₂ (**Fig. 5.2b**) and P2VP400K/SiO₂ (**Fig. 5.2c**) PNCs with the former mostly covering the cases of no polymer bridge network or weak polymer bridges, and the latter having much stronger polymer network than P2VP200K-7v%R9.5. In addition, the shift factors presented in **Fig. 5.3** between neat polymers and PNCs are very similar for the same polymer matrix. Thus, the combination of SAXS and linear viscoelastic measurements suggests the current experimental design covers a wide range of bound polymer fractions and forms and should serve as model system for a further study of the

role of bound polymer for the molecular origins of the mechanical enhancement of PNCs at large deformation.

5.3.3 Uniaxial Extension

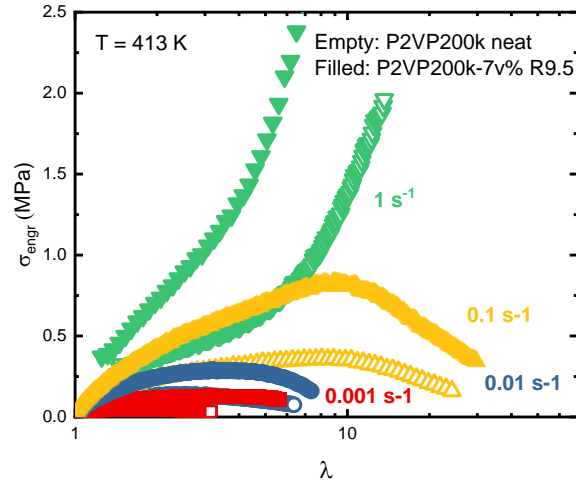


Figure 5.4 Engineering stress σ_{eng} versus elongation ratio λ curves of P2VP200k-7v%R9.5 (filled) with those of neat P2VP100k (empty) as reference.

Uniaxial extension tests at constant Hencky strain rate, $\dot{\epsilon}$, have been performed to study the influence of bound polymer to the mechanical properties of PNCs at large deformation. **Fig. 5.4** presents the engineering stress, σ_{eng} , vs elongation ratio, λ , of P2VP200K-7v%R9.5 and their comparison with neat P2VP200K at $T = 413 K$ at deformation rates from $\dot{\epsilon} = 0.001 s^{-1}$ to $1 s^{-1}$. The σ_{eng} vs λ curves of other PNCs and their comparison with the corresponding neat matrix polymer are presented in **Figs. 5.5a-d**. The presence of NPs leads to several interesting changes to the mechanical properties of PNCs at large deformation. First, the stress-elongation ratio relationship of PNCs of different nanoparticle loadings, different nanoparticle sizes, and different polymer molecular weights are qualitative similar with the neat polymer with an initial elastic-like deformation followed by a stress overshoot, σ_s , at intermediate strain region and failure at high elongation ratios. These features indicate the polymer deformation as the leading mechanism to the mechanical response of PNCs, which is expected due to the low NP loading of

all PNCs. Secondly, all PNCs exhibit higher tensile stress than the neat polymer at the same $\dot{\epsilon}$, highlighting an apparent mechanical reinforcement of PNCs.

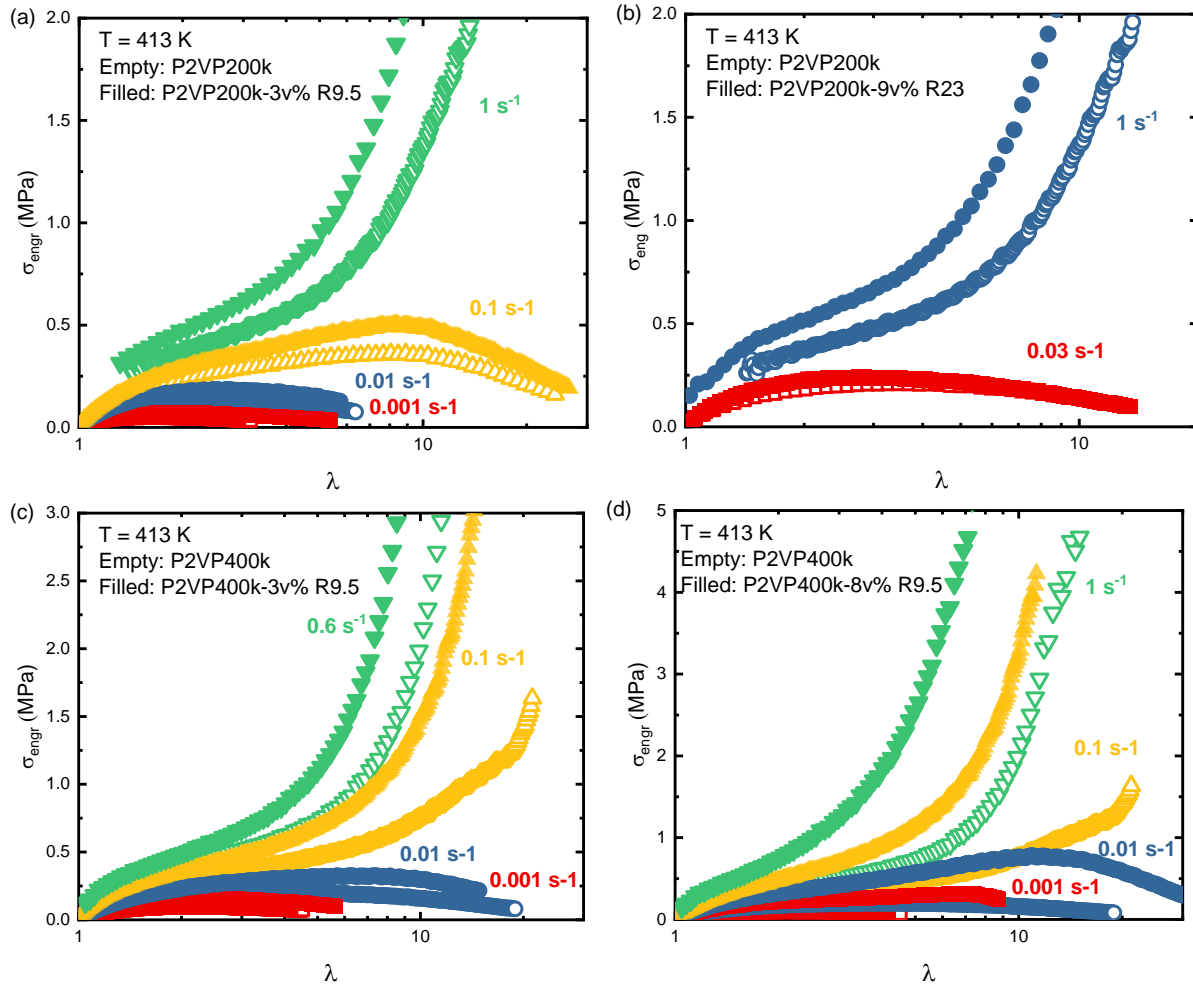


Figure 5.5 Engineering stress σ_{eng} versus elongation ratio λ curves of (a) P2VP200k-3v%R9.5, (b) P2VP200k-9v%R23, (c) P2VP400k-3v%R9.5, and (d) P2VP400k-8v%R9.5 with their neat matrices as references.

Fig. 5.6 highlights the stress-elongation ratios of P2VP200K/SiO₂ nanocomposites of different NP loadings and different NP sizes at $\dot{\epsilon} = 0.03 \text{ s}^{-1}$ (main frame, $Wi_d \approx 1$) and $\dot{\epsilon} = 1 \text{ s}^{-1}$ (inset, $Wi_d \approx 30$). For PNCs with identical NP sizes, P2VP200K-3v%R9.5 and P2VP200K-7v%R9.5, a higher NP loading results in a high stress for both $\dot{\epsilon} = 0.03 \text{ s}^{-1}$ and $\dot{\epsilon} = 1 \text{ s}^{-1}$ over all λ s, highlighting a stronger influence of NPs to the polymer dynamics for PNCs with higher NP loadings. Similar results have also been observed for P2VP100K/SiO₂

nanocomposites and P2VP400K/SiO₂ nanocomposites. The stress enhancement is way higher than the predictions from the hydrodynamic effect, especially at the intermediate strain region. Thus, the hydrodynamic effect alone cannot explain the observed high mechanical enhancement of PNCs at large deformation. Interestingly, for PNCs with similar nanoparticle surface area, such as P2VP200K-3v%R9.5 and P2VP200K-9v%R23, distinct mechanical responses are observed despite their very similar linear viscoelastic spectra (**Fig. 5.2a**). An interestingly observation is that their stress-strain response overlaps nicely only before the stress overshoot. Beyond the stress overshoot, P2VP200K-9v%R23 exhibits a noticeably lower tensile stress than the P2VP200K-3v%R9.5 that gradually approaching the tensile behavior of the neat polymer, implying the weak contribution of the bound polymers to the nonlinear mechanical response beyond the stress overshoot.

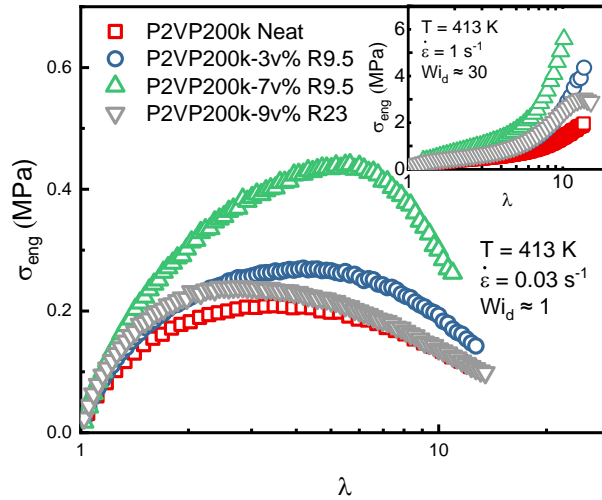


Figure 5.6 Engineering stress σ_{eng} versus elongation ratio λ curves of P2VP200k and P2VP200k/SiO₂ samples at two different Hencky rate $\dot{\epsilon}$ (main figure and inset), respectively.

5.3.4 Engineering Stress Overshoot

To be more quantitative, we analyze the characteristics of stress overshoot of PNCs and compare them with the neat polymer. In neat polymers, the overshoot stress, σ_s , and the corresponding Hencky strain, ϵ_s , scales universally with Wi_d as $\sigma_s \sim Wi_d^{1/3}$ and $\epsilon_s \sim Wi_d^{1/3}$, that

has been attributed to the disentanglement polymer dynamics recently. Thus, a clear characterization of the stress overshoot of PNCs can help elucidate the influence of NPs to nonlinear polymer dynamics. **Fig. 5.7** presents σ_s of P2VP200K/SiO₂ nanocomposites and the neat polymer at different $\dot{\epsilon}$. Although PNCs show a systematic higher σ_s at a given $\dot{\epsilon}$, a scaling of $\sigma_s \sim \dot{\epsilon}^{1/3}$ has been observed for all samples over an exceptional wide range of $Wi_d \sim 0.1 - 10$, indicating a negligible influence of NPs to the scaling of disentanglement dynamics. According to recent theoretical development, the stress overshoot physic is very sensitive to the equilibrium chain packing and the tube diameter, the identical scaling of the stress overshoot between the neat polymer and the PNCs highlights a weak influence of the bound polymer to the tube diameter of the matrix polymer. Remarkably, an excellent master curve of σ_s vs $a(\varphi_{NP})\dot{\epsilon}$ with $a(\varphi_{NP})$ a constant can be observed over the entire rate region for all PNCs (inset of the **Fig. 5.7** and **Figs. 5.8a-b**).

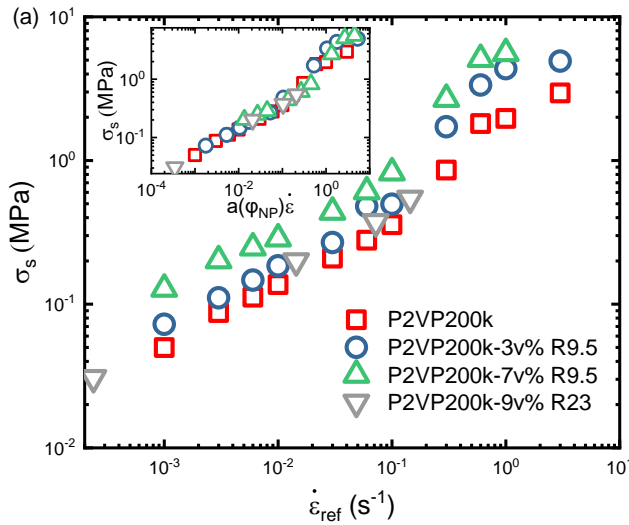


Figure 5.7 The stress overshoot σ_s of P2VP200K/SiO₂ nanocomposites and the neat polymer at different $\dot{\epsilon}$ at a reference temperature of 413K. A master curve is observed after a sample-dependent constant $a(\varphi_{NP})$ is multiplied to the $\dot{\epsilon}$ in the x-axis.

The observed master curve of σ_s vs $a(\varphi_{NP})\dot{\epsilon}$ for PNCs with different NP loadings, NP sizes, and polymer molecular weights are intriguing and suggest universal physics for nonlinear

mechanical reinforcement of PNCs with weak NP-NP interactions. In addition, the non-strain and non-strain rate dependence of $a(\varphi_{NP})$ indicate clearly a strong NP-induced modifications to the matrix polymer dynamic rather than the bound polymer governing the nonlinear polymer dynamics. Note that the master curves apply for PNCs with strong polymer bridging network (P2VP200K-7v%R9.5, P2VP400K-3v%R9.5, and P2VP400K-8v%R9.5), in sharp contrast to recent constitutive modeling on the dominant role of the polymer bridging network for the high mechanical strength of PNCs at large deformation.

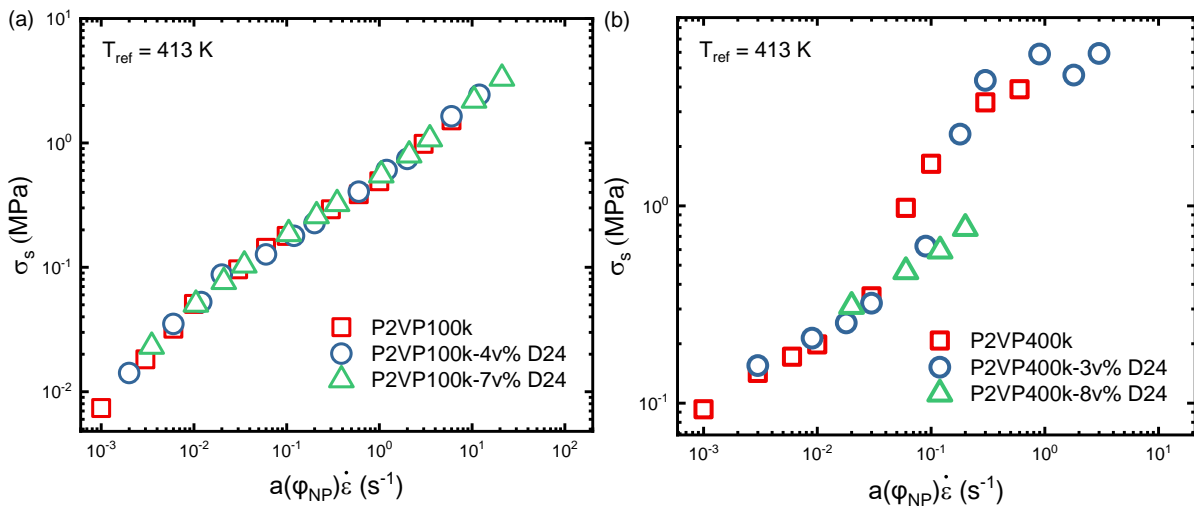


Figure 5.8 The stress overshoot σ_s of (a) P2VP200K/SiO₂ and (b) P2VP400k/SiO₂ samples and the neat polymer at different $\dot{\epsilon}$ at a reference temperature of 413K.

5.3.5 Quantitative Understanding of Stress-strain Curves with the Parameter $a(\varphi_{NP})$

The scaling analyses on the stress overshoot suggest a pure bulk dynamic effect rather than the interfacial effects governing the mechanical enhancement of PNCs at large deformation. If this is true, one would anticipate a quantitative understanding of the mechanical properties of PNCs by taking into account the NP-induced changes in the bulk polymer dynamics, $a(\varphi_{NP})$.

Fig. 5.9 presents the comparison of tensile stress-elongation ratio curves of P2VP200K/SiO₂ nanocomposites with $\dot{\epsilon}a(\varphi_{NP}) = 0.021$ and 0.90. Remarkably, a nice overlap of the stress-strain curves over a wide range of elongation ratios (up to the stress overshoot) can be observed

between the neat matrix polymer and the PNCs, confirming the NP-induced bulk dynamics effect for the nonlinear mechanical properties of PNCs. Note that the dynamic correction applies for PNCs with various NP loading, NP sizes, and $\dot{\epsilon}a(\varphi_{NP})$ values, highlighting the universality of the observation. Note that noticeable deviations in the tensile stress beyond the stress overshoot is still observed, suggesting the emergence of additional mechanisms for the mechanical properties of PNCs beyond the stress overshoot that depends on the strain rate, NP loading, and NP sizes. For instance, the stress of P2VP200K-7v%R9.5 is significantly higher than the neat polymer beyond the stress overshoot at $\dot{\epsilon}a(\varphi_{NP}) = 0.021$ that does not show up at higher strain rates.

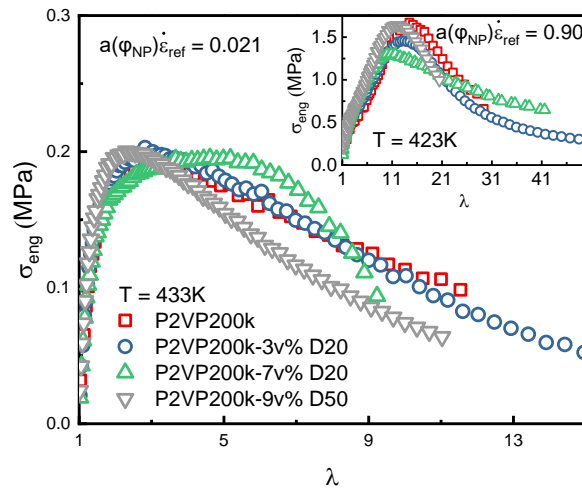


Figure 5.9 Engineering strain-elongation ratio curves for P2VP200k/SiO₂ samples with two $\dot{\epsilon}a(\varphi_{NP})$ values of 0.021 and 0.90 in the main figure and inset, respectively.

On the other hand, PNC of a higher NP loading has a slightly smaller λ_s and σ_s than the neat polymer at high $\dot{\epsilon}a(\varphi_{NP})$ values. The study in Chapter 2 suggests a dominant role of the deformation-induced microstructure rearrangement for the mechanical reinforcement in this region. However, the detailed molecular mechanisms, in addition to the dynamic effect, remains further investigation that governs the mechanical response of PNCs beyond the stress overshoot.

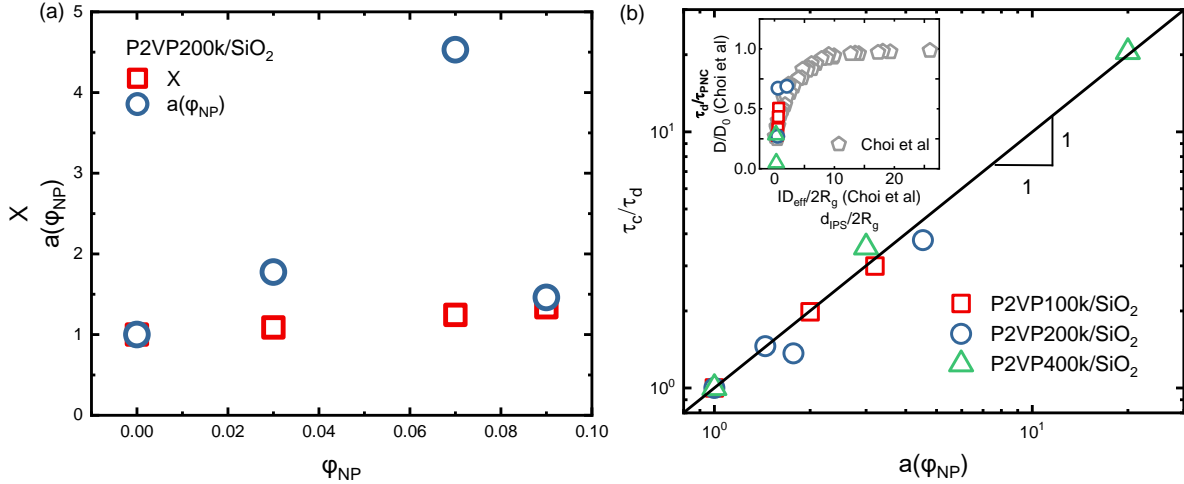


Figure 5.10 (a) A comparison between $a(\varphi_{NP})$ and hydrodynamic reinforcing factor X for P2VP200k/SiO₂ samples. **(b)** A comparison between $a(\varphi_{NP})$ and τ_{PNC}/τ_d of all P2VP/SiO₂ samples where τ_{PNC} is the apparent terminal relaxation time of a PNC and τ_d is the terminal relaxation time of polymer. The inset shows a comparison between τ_d/τ_{PNC} and the experimental data in Choi et al.'s work⁷⁵.

The above observations clearly point out a crucial parameter, $a(\varphi_{NP})$, that plays a leading order effect for the tensile deformation of PNCs. In the following section, we would like to understand molecular parameters controlling $a(\varphi_{NP})$. As discussed previously, $a(\varphi_{NP})$ does not exhibit any strain or strain rate dependence and must be controlled by materials parameters. **Fig. 5.10a** shows the $a(\varphi_{NP})$ vs φ_{NP} and their comparison with the hydrodynamic reinforcement factor, X , (the lines). Obviously, the values of $a(\varphi_{NP})$ are much higher than hydrodynamic reinforcement factor, indicating the non-hydrodynamic nature of the dynamic effects. With the ruling out of the roles of bound polymers, we turn to the NP-induced dynamics slowing down of the bulk polymer. For PNCs with well-separated NPs, the characteristic frequency of the loss peak at the low-frequency region, ω_c , in the linear viscoelastic spectra provides a good estimate of the apparent relaxation time of the non-adsorbed chains, $\tau_c \approx \frac{1}{\omega_c}$. **Fig. 5.10b** presents the normalized apparent relaxation chain time, $\tau_c(\varphi_{NP})/\tau_d$, with $a(\varphi_{NP})$ for all PNCs, where τ_d is the terminal relaxation time of the neat polymer that is determined from the crossover between

the storage moduli, $G'(\omega)$, and loss moduli, $G''(\omega)$, at the low frequency region. Remarkably, $\frac{\tau_c(\varphi_{NP})}{\tau_d} \cong a(\varphi_{NP})$ is observed for PNCs with all NP loadings and NP sizes, regardless of the matrix polymer molecular weight and the status of bound polymers (bridge or not), highlighting the crucial role of the dynamics slowing down of *non-adsorbed* polymers for the nonlinear mechanical enhancement of PNCs. Moreover, the observed $a(\varphi_{NP})$ agrees excellently well with previously observed universal slowing down of the center-of-mass diffusion of matrix polymers in PNCs as shown in the inset of **Fig. 5.10b**, which has been attributed to the nanoconfinement effect due to the presence of NPs. Our experiments seem to echo the nanoconfinement origin for the slowing down in non-adsorbed polymer dynamics.

5.4 Conclusions

With rigorous experimental design of P2VP/SiO₂ samples with different molecular weight and nanoparticle loadings, this chapter systematically studies how the presence of nanoparticle on the nonlinear rheology of PNCs at large deformation. It was found the slowing down of the chain relaxation dynamics controls the mechanical reinforcement of PNCs at large deformation. In sharp contrast to the recent proposal of constitutive modeling¹¹², our work shows bound polymers and bridge polymer contribute negligible to the mechanical reinforcement of polymer nanocomposites. In addition, the presence of NPs does not affect the scaling of the stress overshoot (disentanglement dynamics) of matrix polymer.

CHAPTER 6 CONCLUSIONS AND FUTURE OUTLOOK

6.1 Conclusions

This work investigates the origin of mechanical reinforcement in polymer nanocomposites (PNCs) with spherical nanoparticles at the dilute and semi-dilute limits. Linear and nonlinear rheology are utilized to probe the mechanical reinforcement in the PNCs. The contributions from the nanoparticle rearrangement and the polymer deformation are decoupled through the utilization of small-angle scattering techniques. At $Wi = \dot{\epsilon}\tau_d \ll 1$, a nanoparticle network can be induced, where $\dot{\epsilon}$ is the Hencky strain rate and τ_d is the terminal relaxation time of the polymer. Importantly, the elastic yielding of this nanoparticle network contributes significantly to the stress and causes strain hardening in the PNCs. At higher Wi , it was found that the deformation-induced nanoparticle rearrangement does not correlate with the stress in the PNCs at large deformation. The small-angle x-ray scattering (SAXS) reveals the structural anisotropy of nanoparticles remains little changed at large deformation, in sharp contrast to strong rise in the reinforcement factor (stress of PNC normalized by that of neat polymer) with deformation.

To further decouple the polymer contribution to the macroscopic stress, we selectively investigate the nonlinear polymer structure and dynamics through the small-angle neutron scattering (SANS). The polymer anisotropy unambiguously determined by the spherical harmonic expansion analysis suggests almost identical magnitudes between the neat polymer and the PNCs. The stress relaxation of the polymers anisotropy in PNCs also follows that of the deformed polymers. Further analysis in PNC systems with aggregated nanoparticles shows similar observations. The SANS results clearly demonstrate the absence of strain amplification in the PNCs and support the hydrodynamic effect of nanoparticles as the origin of the mechanical reinforcement in the PNCs, akin to the classical hydrodynamic effect of nanoparticles. According

to classical hydrodynamic theory by Einstein and Smallwood, strain redistributes surrounding nanoparticles leading to strong mechanical reinforcement, while average zero net deformation takes place in the matrix in the PNC.

We further quantified the nanoconfinement effect to the mechanical reinforcement in the PNCs. PNCs with different polymer molecular weights and nanoparticle sizes were prepared and studied by nonlinear rheology. It was found that a master curve can be established between the engineering stress maximum point and the strain at the maximum point with a constant $a(\varphi_{NP})$ within the same molecular weight. The $a(\varphi_{NP})$ was directly proportional apparent terminal relaxation time of the PNCs normalized by the terminal relaxation time of the polymer matrix, suggesting bulk polymer origin of the mechanical reinforcement. Further uniaxial extension experiments were performed for different PNCs at the same $a(\varphi_{NP})\dot{\epsilon}$ value, and the stress-strain curves were found to overlap up to the stress maximum point across all the PNCs with the same molecular weight. We found out the ratio between the terminal relaxation time of polymers and that of the PNCs follows the delayed diffusion of the polymers in the PNCs under the nanoconfinement effect presented in the literature. Thus, the linear rheology can be used to quantify the nanoconfinement effect, which is an important parameter in the mechanical reinforcement in the PNCs. In addition, our work suggests interfacial polymers contribute negligibly to the mechanical reinforcement of polymer nanocomposites, and the disentanglement dynamics is hardly affected by the presence of NPs.

6.2 Future Outlook

By decoupling the contributions from the nanoparticles and polymer matrix in the mechanical reinforcement of PNCs, this work provides an experimental foundation for a molecular constitutive model of PNCs under large deformation. At small $Wi \ll 1$, the polymer deformation

controls the yielding behavior. However, nanoparticle contribution dominates the macroscopic stress at a late stage of the deformation and the contributions from strain-induced nanoparticle networks cannot be ignored. At large $Wi > 1$, polymer dynamics play a dominant role and the problem becomes to model the delayed polymer response. The comprehensive results of the nanoparticle rearrangement at large deformation at different Wi inspires new materials designed with controlled nanoparticle structures. The applications of the SHE on SANS analysis of the PNCs encourage the reanalysis of previous SANS data and future SANS studies on the multi-phase systems.

In this work, several questions still need to be addressed. The yielding of the nanoparticle network at $Wi \ll 1$ is proven to provide significant mechanical reinforcement. However, the quantification of this reinforcement is yet to be fully understood, although we have proven that the stress from this process is proportional to the surface area of the nanoparticles. Further considerations need to consider the hydrodynamic effect between nanoparticles and other nanoparticle-nanoparticle interactions, which would require modeling. At the same effective Wi , we have observed the overlapping polymer, and PNC stress-strain curves up to the stress maximum point. However, the stress magnitudes and shapes have no systematic behaviors between neat polymer and PNCs, which is another important direction to pursue in terms of the polymer dynamics after disentanglement.

Several limitations of this work exist. Due to the significant contributions from the nanoparticles at $Wi \ll 1$, different nanoparticle sizes and nanoparticle-nanoparticle interactions need to be studied for a comprehensive understanding of the nanoparticle contributions to the mechanical reinforcement. Additionally, only uniaxial extension is investigated in this work. However, other modes of deformation are also important and can yield different types of

nanoparticle microstructure rearrangement and corresponding mechanical reinforcement, such as shear and biaxial extension.

BIBLIOGRAPHY

BIBLIOGRAPHY

1. Kumar, S. K.; Benicewicz, B. C.; Vaia, R. A.; Winey, K. I., 50th Anniversary Perspective: Are Polymer Nanocomposites Practical for Applications? *Macromolecules* **2017**, *50* (3), 714-731.
2. Cheng, S.; Xie, S. J.; Carrillo, J. Y.; Carroll, B.; Martin, H.; Cao, P. F.; Dadmun, M. D.; Sumpter, B. G.; Novikov, V. N.; Schweizer, K. S.; Sokolov, A. P., Big Effect of Small Nanoparticles: A Shift in Paradigm for Polymer Nanocomposites. *ACS Nano* **2017**, *11* (1), 752-759.
3. Vilgis, T. A.; Heinrich, G.; Klüppel, M., *Reinforcement of Polymer Nano-Composites: Theory, Experiments and Applications*. Cambridge University Press: Cambridge, 2009.
4. Merkel, T. C.; Freeman, B. D.; Spontak, R. J.; He, Z.; Pinnau, I.; Meakin, P.; Hill, A. J., Ultrapermeable, Reverse-Selective Nanocomposite Membranes. *Science* **2002**, *296* (5567), 519-522.
5. Jancar, J.; Douglas, J. F.; Starr, F. W.; Kumar, S. K.; Cassagnau, P.; Lesser, A. J.; Sternstein, S. S.; Buehler, M. J., Current issues in research on structure-property relationships in polymer nanocomposites. *Polymer* **2010**, *51* (15), 3321-3343.
6. Punetha, V. D.; Rana, S.; Yoo, H. J.; Chaurasia, A.; McLeskey Jr, J. T.; Ramasamy, M. S.; Sahoo, N. G.; Cho, J. W., Functionalization of carbon nanomaterials for advanced polymer nanocomposites: A comparison study between CNT and graphene. *Prog. Polym. Sci.* **2017**, *67*, 1-47.
7. Okada, A.; Usuki, A., Twenty Years of Polymer-Clay Nanocomposites. *Macromolecular Materials and Engineering* **2006**, *291* (12), 1449-1476.
8. Garcés, J. M.; Moll, D. J.; Bicerano, J.; Fibiger, R.; McLeod, D. G., Polymeric Nanocomposites for Automotive Applications. *Advanced Materials* **2000**, *12* (23), 1835-1839.
9. Rahman, A.; Ali, I.; Al Zahrani, S. M.; Eleithy, R. H., A REVIEW OF THE APPLICATIONS OF NANOCARBON POLYMER COMPOSITES. *Nano* **2011**, *06* (03), 185-203.
10. Chandra, A. K.; Kumar, N. R., Polymer Nanocomposites for Automobile Engineering Applications. In *Properties and Applications of Polymer Nanocomposites: Clay and Carbon Based Polymer Nanocomposites*, Tripathy, D. K.; Sahoo, B. P., Eds. Springer Berlin Heidelberg: Berlin, Heidelberg, **2017**; pp 139-172.
11. De, D.; Panda, P. K.; Roy, M.; Bhunia, S.; Jaman, A. I., Reinforcing effect of nanosilica on the properties of natural rubber/reclaimed ground rubber tire vulcanizates. *Polymer Engineering & Science* **2013**, *53* (2), 227-237.

12. Mao, Y.; Tian, Q.; Zhang, C.; Tang, Y.; Wang, Y.; Li, X.; Ding, T., Vulcanization accelerator functionalized nanosilica: Effect on the reinforcement behavior of SSBR/BR. *Polymer Engineering & Science* **2019**, *59* (6), 1270-1278.
13. Saha, N. R.; Sarkar, G.; Roy, I.; Bhattacharyya, A.; Rana, D.; Dhanarajan, G.; Banerjee, R.; Sen, R.; Mishra, R.; Chattopadhyay, D., Nanocomposite films based on cellulose acetate/polyethylene glycol/modified montmorillonite as nontoxic active packaging material. *RSC Advances* **2016**, *6* (95), 92569-92578.
14. Bratovčić, A.; Odošić, A.; Čatić, S.; Šestan, I., Application of polymer nanocomposite materials in food packaging. *Croatian journal of food science and technology* **2015**, *7* (2), 86-94.
15. Yampolskii, Y., Polymeric Gas Separation Membranes. *Macromolecules* **2012**, *45* (8), 3298-3311.
16. Chung, T.-S.; Jiang, L. Y.; Li, Y.; Kulprathipanja, S., Mixed matrix membranes (MMMs) comprising organic polymers with dispersed inorganic fillers for gas separation. **2007**.
17. Prateek; Thakur, V. K.; Gupta, R. K., Recent Progress on Ferroelectric Polymer-Based Nanocomposites for High Energy Density Capacitors: Synthesis, Dielectric Properties, and Future Aspects. *Chemical Reviews* **2016**, *116* (7), 4260-4317.
18. Tchoul, M. N.; Fillery, S. P.; Koerner, H.; Drummy, L. F.; Oyerokun, F. T.; Mirau, P. A.; Durstock, M. F.; Vaia, R. A., Assemblies of Titanium Dioxide-Polystyrene Hybrid Nanoparticles for Dielectric Applications. *Chemistry of Materials* **2010**, *22* (5), 1749-1759.
19. Naskar, A. K.; Keum, J. K.; Boeman, R. G., Polymer matrix nanocomposites for automotive structural components. *Nat Nanotechnol* **2016**, *11* (12), 1026-1030.
20. Müller, K.; Bugnicourt, E.; Latorre, M.; Jorda, M.; Echegoyen Sanz, Y.; Lagaron, J. M.; Miesbauer, O.; Bianchin, A.; Hankin, S.; Bölz, U.; Pérez, G.; Jesdinszki, M.; Lindner, M.; Scheuerer, Z.; Castelló, S.; Schmid, M., Review on the Processing and Properties of Polymer Nanocomposites and Nanocoatings and Their Applications in the Packaging, Automotive and Solar Energy Fields. *Nanomaterials (Basel, Switzerland)* **2017**, *7* (4), 74.
21. Leung, S. N., Thermally conductive polymer composites and nanocomposites: Processing-structure-property relationships. *Composites Part B: Engineering* **2018**, *150*, 78-92.
22. Carroll, B.; Cheng, S.; Sokolov, A. P., Analyzing the Interfacial Layer Properties in Polymer Nanocomposites by Broadband Dielectric Spectroscopy. *Macromolecules* **2017**, *50* (16), 6149-6163.
23. Cheng, S.; Carroll, B.; Lu, W.; Fan, F.; Carrillo, J.-M. Y.; Martin, H.; Holt, A. P.; Kang, N.-G.; Bocharova, V.; Mays, J. W.; Sumpster, B. G.; Dadmun, M.; Sokolov, A. P., Interfacial Properties of Polymer Nanocomposites: Role of Chain Rigidity and Dynamic Heterogeneity Length Scale. *Macromolecules* **2017**, *50* (6), 2397-2406.
24. Tadmor, Z.; Gogos, C. G., *Principles of polymer processing*. John Wiley & Sons: **2013**.

25. Park, J. U.; Kim, J. L.; Kim, D. H.; Ahn, K. H.; Lee, S. J.; Cho, K. S., Rheological behavior of polymer/layered silicate nanocomposites under uniaxial extensional flow. *Macromolecular Research* **2006**, *14* (3), 318-323.
26. Petrie, C., Elongational Flows: Aspects of the Behavior of Model Viscoelastic Fluid. *Journal of Fluid Mechanics* **1979**, *95* (04).
27. Malkin, A. Y.; Arinstein, A.; Kulichikhin, V. G., Polymer extension flows and instabilities. *Progress in Polymer Science* **2014**, *39* (5), 959-978.
28. Jouault, N.; Dalmas, F.; Boué, F.; Jestin, J., Nanoparticles reorganizations in polymer nanocomposites under large deformation. *Polymer* **2014**, *55* (10), 2523-2534.
29. Botti, A.; Pyckhout-Hintzen, W.; Richter, D.; Urban, V.; Straube, E., A microscopic look at the reinforcement of silica-filled rubbers. *J Chem Phys* **2006**, *124* (17), 174908.
30. Rharbi, Y.; Cabane, B.; Vacher, A.; Joanicot, M.; Boué, F., Modes of deformation in a soft/hard nanocomposite: A SANS study. *Europhys. Lett.* **1999**, *46* (4), 472-478.
31. Hershey, C.; Jayaraman, K., Dynamics of entangled polymer chains with nanoparticle attachment under large amplitude oscillatory shear. *Journal of Polymer Science Part B: Polymer Physics* **2019**, *57* (1), 62-76.
32. Sarvestani, A. S.; Picu, C. R., A frictional molecular model for the viscoelasticity of entangled polymer nanocomposites. *Rheologica Acta* **2005**, *45* (2), 132-141.
33. Sarvestani, A. S.; Picu, C. R., Network model for the viscoelastic behavior of polymer nanocomposites. *Polymer* **2004**, *45* (22), 7779-7790.
34. Wang, Z.; Lam, C. N.; Chen, W.-R.; Wang, W.; Liu, J.; Liu, Y.; Porcar, L.; Stanley, C. B.; Zhao, Z.; Hong, K.; Wang, Y., Fingerprinting Molecular Relaxation in Deformed Polymers. *Physical Review X* **2017**, *7* (3).
35. Zhao, J.; Morgan, A. B.; Harris, J. D., Rheological characterization of polystyrene–clay nanocomposites to compare the degree of exfoliation and dispersion. *Polymer* **2005**, *46* (20), 8641-8660.
36. Drozdov, A. D.; Jensen, E. A.; Christiansen, J. d. C., Nonlinear time-dependent response of polypropylene/nanoclay melts: Experiments and modeling. *Computational Materials Science* **2010**, *47* (3), 807-816.
37. Rubinstein, M.; Colby, R. H., *Polymer physics*. Oxford University Press: Oxford ;, 2007.
38. Smallwood, H. M., Limiting Law of the Reinforcement of Rubber. *Journal of Applied Physics* **1944**, *15* (11), 758-766.
39. Song, Y.; Zheng, Q., Concepts and conflicts in nanoparticles reinforcement to polymers beyond hydrodynamics. *Progress in Materials Science* **2016**, *84*, 1-58.

40. Baeza, G. P.; Dessi, C.; Costanzo, S.; Zhao, D.; Gong, S.; Alegria, A.; Colby, R. H.; Rubinstein, M.; Vlassopoulos, D.; Kumar, S. K., Network dynamics in nanofilled polymers. *Nat Commun* **2016**, *7*, 11368.
41. Rothstein, J. P.; McKinley, G. H., Inhomogeneous transient uniaxial extensional rheometry. *Journal of Rheology* **2002**, *46* (6), 1419-1443.
42. Rothstein, J. P., Transient extensional rheology of wormlike micelle solutions. *Journal of Rheology* **2003**, *47* (5), 1227-1247.
43. Meissner, J., Development of a Universal Extensional Rheometer for the Uniaxial Extension of Polymer Melts. *Transactions of the Society of Rheology* **1972**, *16* (3), 405-420.
44. Sentmanat, M. L., Miniature universal testing platform: from extensional melt rheology to solid-state deformation behavior. *Rheologica acta* **2004**, *43* (6), 657-669.
45. Oberdisse, J.; Pyckhout-Hintzen, W.; Straube, E., Structure Determination of Polymer Nanocomposites by Small Angle Scattering. In *Recent Advances in Polymer Nanocomposites*, Thomas, S.; Zaikov, G. E.; Valsaraj, S. V., Eds. **2009**.
46. Roe, R. J., *Methods of X-ray and neutron scattering in polymer science*. Oxford University Press: New York, **2000**.
47. Musino, D.; Genix, A. C.; Chauveau, E.; Bizien, T.; Oberdisse, J., Structural identification of percolation of nanoparticles. *Nanoscale* **2020**, *12* (6), 3907-3915.
48. Jouault, N.; Dalmas, F.; Said, S.; Di Cola, E.; Schweins, R.; Jestin, J.; Boué, F., Direct Measurement of Polymer Chain Conformation in Well-Controlled Model Nanocomposites by Combining SANS and SAXS. *Macromolecules* **2010**, *43* (23), 9881-9891.
49. Jancar, J.; Douglas, J. F.; Starr, F. W.; Kumar, S. K.; Cassagnau, P.; Lesser, A. J.; Sternstein, S. S.; Buehler, M. J., Current issues in research on structure–property relationships in polymer nanocomposites. *Polymer* **2010**, *51* (15), 3321-3343.
50. Baeza, G. P.; Genix, A.-C.; Degrandcourt, C.; Petitjean, L.; Gummel, J.; Couty, M.; Oberdisse, J., Multiscale Filler Structure in Simplified Industrial Nanocomposite Silica/SBR Systems Studied by SAXS and TEM. *Macromolecules* **2013**, *46* (1), 317-329.
51. Benmouna, M.; Hammouda, B., The zero average contrast condition: Theoretical predictions and experimental examples. *Progress in Polymer Science* **1997**, *22* (1), 49-92.
52. Jouault, N.; Dalmas, F.; Said, S.; Di Cola, E.; Schweins, R.; Jestin, J.; Boué, F., Direct small-angle-neutron-scattering observation of stretched chain conformation in nanocomposites: More insight on polymer contributions in mechanical reinforcement. *Physical Review E* **2010**, *82* (3), 031801.

53. Donnet, J.-B.; Custodero, E., Chapter 8 - Reinforcement of Elastomers by Particulate Fillers. In *The Science and Technology of Rubber (Fourth Edition)*, Mark, J. E.; Erman, B.; Roland, C. M., Eds. Academic Press: Boston, **2013**; pp 383-416.
54. Einstein, A., Eine neue Bestimmung der Moleküldimensionen. *Annalen der Physik* **1906**, *324* (2), 289-306.
55. Einstein, A., Berichtigung zu meiner Arbeit: „Eine neue Bestimmung der Moleküldimensionen“. *Annalen der Physik* **1911**, *339* (3), 591-592.
56. Domurath, J.; Saphiannikova, M.; Heinrich, G., The concept of hydrodynamic amplification infilled elastomers. *Kautsch. Gummi, Kunstst.* **2017**, *70* (40).
57. Mullins, L.; Tobin, N. R., Stress softening in rubber vulcanizates. Part I. Use of a strain amplification factor to describe the elastic behavior of filler-reinforced vulcanized rubber. *Journal of Applied Polymer Science* **1965**, *9* (9), 2993-3009.
58. Domurath, J.; Saphiannikova, M.; Ausias, G.; Heinrich, G., Modelling of stress and strain amplification effects in filled polymer melts. *Journal of Non-Newtonian Fluid Mechanics* **2012**, *171-172*, 8-16.
59. Pérez-Aparicio, R.; Schiewek, M.; Valentín, J. L.; Schneider, H.; Long, D. R.; Saphiannikova, M.; Sotta, P.; Saalwächter, K.; Ott, M., Local Chain Deformation and Overstrain in Reinforced Elastomers: An NMR Study. *Macromolecules* **2013**, *46* (14), 5549-5560.
60. Westermann, S.; Kreitschmann, M.; Pyckhout-Hintzen, W.; Richter, D.; Straube, E.; Farago, B.; Goerigk, G., Matrix Chain Deformation in Reinforced Networks: a SANS Approach. *Macromolecules* **1999**, *32* (18), 5793-5802.
61. Gupta, R. K.; Pasanovic-Zujo, V.; Bhattacharya, S. N., Shear and extensional rheology of EVA/layered silicate-nanocomposites. *Journal of Non-Newtonian Fluid Mechanics* **2005**, *128* (2-3), 116-125.
62. Okamoto, M.; Nam, P. H.; Maiti, P.; Kotaka, T.; Hasegawa, N.; Usuki, A., A House of Cards Structure in Polypropylene/Clay Nanocomposites under Elongational Flow. *Nano Letters* **2001**, *1* (6), 295-298.
63. Shen, Y.; Harkin-Jones, E.; Hornsby, P.; McNally, T.; Abu-Zurayk, R., The effect of temperature and strain rate on the deformation behaviour, structure development and properties of biaxially stretched PET-clay nanocomposites. *Composites Science and Technology* **2011**, *71* (5), 758-764.
64. Kamiya, H.; Suzuki, H.; Kato, D.; Jimbo, G., Densification of Alkoxide-Derived Fine Silica Powder Compact by Ultra-High-Pressure Cold Isostatic Pressing. *Journal of the American Ceramic Society* **1993**, *76* (1), 54-64.

65. Iijima, M.; Kamiya, H., Layer-by-Layer Surface Modification of Functional Nanoparticles for Dispersion in Organic Solvents. *Langmuir* **2010**, *26* (23), 17943-17948.
66. Cheng, S.; Holt, A. P.; Wang, H.; Fan, F.; Bocharova, V.; Martin, H.; Etampawala, T.; White, B. T.; Saito, T.; Kang, N.-G.; Dadmun, M. D.; Mays, J. W.; Sokolov, A. P., Unexpected Molecular Weight Effect in Polymer Nanocomposites. *Phys. Rev. Lett.* **2016**, *116* (3), 038302.
67. Oberdisse, J.; Pyckhout-Hintzen, W.; Straube, E., *Structure Determination of Polymer Nanocomposites by Small Angle Scattering*. HAL: Brill, **2009**.
68. Genix, A.-C.; Oberdisse, J., Nanoparticle self-assembly: from interactions in suspension to polymer nanocomposites. *Soft Matter* **2018**, *14* (25), 5161-5179.
69. Chen, Q.; Gong, S.; Moll, J.; Zhao, D.; Kumar, S. K.; Colby, R. H., Mechanical Reinforcement of Polymer Nanocomposites from Percolation of a Nanoparticle Network. *ACS Macro Letters* **2015**, *4* (4), 398-402.
70. Holt, A. P.; Bocharova, V.; Cheng, S.; Kisliuk, A. M.; White, B. T.; Saito, T.; Uhrig, D.; Mahalik, J. P.; Kumar, R.; Imel, A. E.; Etampawala, T.; Martin, H.; Sikes, N.; Sumpter, B. G.; Dadmun, M. D.; Sokolov, A. P., Controlling Interfacial Dynamics: Covalent Bonding versus Physical Adsorption in Polymer Nanocomposites. *ACS Nano* **2016**, *10* (7), 6843-6852.
71. Moro, S.; Parneix, C.; Cabane, B.; Sanson, N.; d'Espinose de Lacaillerie, J.-B., Hydrophobization of Silica Nanoparticles in Water: Nanostructure and Response to Drying Stress. *Langmuir* **2017**, *33* (19), 4709-4719.
72. Yang, J.; Melton, M.; Sun, R.; Yang, W.; Cheng, S., Decoupling the Polymer Dynamics and the Nanoparticle Network Dynamics of Polymer Nanocomposites through Dielectric Spectroscopy and Rheology. *Macromolecules* **2020**, *53* (1), 302-311.
73. Domurath, J.; Saphiannikova, M.; Heinrich, G., The concept of hydrodynamic amplification in filled elastomers. *Kautschuk und Gummi Kunststoffe* **2017**, *70*, 40-43.
74. Lin, C.-C.; Gam, S.; Meth, J. S.; Clarke, N.; Winey, K. I.; Composto, R. J., Do Attractive Polymer–Nanoparticle Interactions Retard Polymer Diffusion in Nanocomposites? *Macromolecules* **2013**, *46* (11), 4502-4509.
75. Choi, J.; Hore, M. J. A.; Meth, J. S.; Clarke, N.; Winey, K. I.; Composto, R. J., Universal Scaling of Polymer Diffusion in Nanocomposites. *ACS Macro Letters* **2013**, *2* (6), 485-490.
76. Laun, H. M.; Munstedt, H., Elongational behavior of a low-density polyethylene melt .1. Strain rate and stress dependence of viscosity and recoverable strain in steady-state - comparison with shear data - influence of interfacial-tension. *Rheol. Acta* **1978**, *17* (4), 415-425.
77. Meissner, J., Development of a universal extensional rheometer for uniaxial extension of polymer melts. *T. Soc. Rheol.* **1972**, *16* (3), 405-&.

78. Hwan Lee, S.; Cho, E.; Ryoun Youn, J., Rheological behavior of polypropylene/layered silicate nanocomposites prepared by melt compounding in shear and elongational flows. *J. Appl. Polym. Sci.* **2007**, *103* (6), 3506-3515.
79. Gupta, R. K.; Pasanovic-Zujo, V.; Bhattacharya, S. N., Shear and extensional rheology of EVA/layered silicate-nanocomposites. *J. Non-Newtonian Fluid Mech.* **2005**, *128* (2), 116-125.
80. Wang, Y.; Boukany, P.; Wang, S. Q.; Wang, X., Elastic Breakup in Uniaxial Extension of Entangled Polymer Melts. *Phys. Rev. Lett.* **2007**, *99* (23), 237801.
81. Wang, S. Q.; Ravindranath, S.; Wang, Y.; Boukany, P., New theoretical considerations in polymer rheology: Elastic breakdown of chain entanglement network. *J. Chem. Phys.* **2007**, *127* (6), 064903.
82. Schweizer, K. S.; Xie, S.-J., Physics of the Stress Overshoot and Chain Stretch Dynamics of Entangled Polymer Liquids Under Continuous Startup Nonlinear Shear. *ACS Macro Letters* **2018**, 218-222.
83. Graham, R. S.; Likhtman, A. E.; McLeish, T. C. B.; Milner, S. T., Microscopic theory of linear, entangled polymer chains under rapid deformation including chain stretch and convective constraint release. *J. Rheol.* **2003**, *47* (5), 1171-1200.
84. Xie, S.-J.; Schweizer, K. S., Consequences of Delayed Chain Retraction on the Rheology and Stretch Dynamics of Entangled Polymer Liquids under Continuous Nonlinear Shear Deformation. *Macromolecules* **2018**, *51* (11), 4185-4200.
85. Sollich, P.; Lequeux, F.; Hébraud, P.; Cates, M. E., Rheology of Soft Glassy Materials. *Phys. Rev. Lett.* **1997**, *78* (10), 2020-2023.
86. Sollich, P., Rheological constitutive equation for a model of soft glassy materials. *Phys. Rev. E* **1998**, *58* (1), 738-759.
87. Okamoto, M., Chapter 5. Rheology and Processing of Polymer/Layered Silicate Nanocomposites. In *Rheology and Processing of Polymer Nanocomposites*, Thomas, S.; Muller, R.; Abraham, J., Eds. **2016**; pp 187-234.
88. Yamamoto, U.; Schweizer, K. S., Microscopic Theory of the Long-Time Diffusivity and Intermediate-Time Anomalous Transport of a Nanoparticle in Polymer Melts. *Macromolecules* **2015**, *48* (1), 152-163.
89. Griffin, P. J.; Bocharova, V.; Middleton, L. R.; Composto, R. J.; Clarke, N.; Schweizer, K. S.; Winey, K. I., Influence of the Bound Polymer Layer on Nanoparticle Diffusion in Polymer Melts. *ACS Macro Letters* **2016**, *5* (10), 1141-1145.
90. Gin, P.; Jiang, N.; Liang, C.; Taniguchi, T.; Akgun, B.; Satija, S. K.; Endoh, M. K.; Koga, T., Revealed Architectures of Adsorbed Polymer Chains at Solid-Polymer Melt Interfaces. *Phys. Rev. Lett.* **2012**, *109* (26), 265501.

91. Oberdisse, J.; Rharbi, Y.; Boué, F., Simulation of aggregate structure and SANS-spectra in filled elastomers. *Comput. Theor. Polym. Sci.* **2000**, *10* (1), 207-217.
92. Sun, R.; Melton, M.; Zuo, X.; Cheng, S., Nonmonotonic Strain Rate Dependence on the Strain Hardening of Polymer Nanocomposites. *ACS Macro Letters* **2020**, *9* (9), 1224-1229.
93. Wang, S. Q.; Ravindranath, S.; Wang, Y.; Boukany, P., New theoretical considerations in polymer rheology: elastic breakdown of chain entanglement network. *J Chem Phys* **2007**, *127* (6), 064903.
94. Wang, Y.; Boukany, P.; Wang, S. Q.; Wang, X., Elastic breakup in uniaxial extension of entangled polymer melts. *Phys Rev Lett* **2007**, *99* (23), 237801.
95. Schweizer, K. S.; Xie, S.-J., Physics of the Stress Overshoot and Chain Stretch Dynamics of Entangled Polymer Liquids Under Continuous Startup Nonlinear Shear. *ACS Macro Letters* **2018**, *7* (2), 218-222.
96. Jouault, N.; Crawford, M. K.; Chi, C.; Smalley, R. J.; Wood, B.; Jestin, J.; Melnichenko, Y. B.; He, L.; Guise, W. E.; Kumar, S. K., Polymer Chain Behavior in Polymer Nanocomposites with Attractive Interactions. *ACS Macro Letters* **2016**, *5* (4), 523-527.
97. Wang, Y.; Wang, W.; Hong, K.; Do, C.; Chen, W.-R., Quantitative examination of a fundamental assumption in small-angle neutron scattering studies of deformed polymer melts. *Polymer* **2020**, *204*, 122698.
98. Lam, C. N.; Xu, W.-S.; Chen, W.-R.; Wang, Z.; Stanley, C. B.; Carrillo, J.-M. Y.; Uhrig, D.; Wang, W.; Hong, K.; Liu, Y.; Porcar, L.; Do, C.; Smith, G. S.; Sumpter, B. G.; Wang, Y., Scaling Behavior of Anisotropy Relaxation in Deformed Polymers. *Physical Review Letters* **2018**, *121* (11), 117801.
99. Zhu, Z.; Thompson, T.; Wang, S.-Q.; von Meerwall, E. D.; Halasa, A., Investigating Linear and Nonlinear Viscoelastic Behavior Using Model Silica-Particle-Filled Polybutadiene. *Macromolecules* **2005**, *38* (21), 8816-8824.
100. Wang, J.; Guo, Y.; Yu, W.; Zhou, C.; Steeman, P., Linear and nonlinear viscoelasticity of polymer/silica nanocomposites: an understanding from modulus decomposition. *Rheologica Acta* **2016**, *55* (1), 37-50.
101. Hasimoto, H., A Sphere Theorem on the Stokes Equation for Axisymmetric Viscous Flow. *Journal of the Physical Society of Japan* **1956**, *11* (7), 793-797.
102. Batchelor, G. K., The stress system in a suspension of force-free particles. *Journal of Fluid Mechanics* **1970**, *41* (3), 545-570.
103. Chwang, A. T.; Wu, T. Y.-T., Hydromechanics of low-Reynolds-number flow. Part 2. Singularity method for Stokes flows. *Journal of Fluid Mechanics* **1975**, *67* (4), 787-815.

104. Jeffrey, D. J.; Acrivos, A., The rheological properties of suspensions of rigid particles. *AIChE Journal* **1976**, *22* (3), 417-432.
105. Zeng, Q. H.; Yu, A. B.; Lu, G. Q., Multiscale modeling and simulation of polymer nanocomposites. *Progress in Polymer Science* **2008**, *33* (2), 191-269.
106. Vogiatzis, G. G.; Theodorou, D. N., Structure of Polymer Layers Grafted to Nanoparticles in Silica–Polystyrene Nanocomposites. *Macromolecules* **2013**, *46* (11), 4670-4683.
107. Irving, J. H.; Kirkwood, J. G., The Statistical Mechanical Theory of Transport Processes. IV. The Equations of Hydrodynamics. *The Journal of Chemical Physics* **1950**, *18* (6), 817-829.
108. Huang, G.-R.; Wu, B.; Wang, Y.; Chen, W.-R., Characterization of microscopic deformation through two-point spatial correlation functions. *Physical Review E* **2018**, *97* (1), 012605.
109. Cheng, S.; Bocharova, V.; Belianinov, A.; Xiong, S.; Kisliuk, A.; Somnath, S.; Holt, A. P.; Ovchinnikova, O. S.; Jesse, S.; Martin, H.; Etampawala, T.; Dadmun, M.; Sokolov, A. P., Unraveling the Mechanism of Nanoscale Mechanical Reinforcement in Glassy Polymer Nanocomposites. *Nano Letters* **2016**, *16* (6), 3630-3637.
110. Vogt, B. D., Mechanical and viscoelastic properties of confined amorphous polymers. *Journal of Polymer Science Part B: Polymer Physics* **2018**, *56* (1), 9-30.
111. Oberdisse, J.; Hine, P.; Pyckhout-Hintzen, W., Structure of interacting aggregates of silica nanoparticles in a polymer matrix: small-angle scattering and reverse Monte Carlo simulations. *Soft Matter* **2007**, *3* (4), 476-485.
112. Genix, A. C.; Bocharova, V.; Carroll, B.; Lehmann, M.; Saito, T.; Krueger, S.; He, L.; Dieudonne-George, P.; Sokolov, A. P.; Oberdisse, J., Understanding the Static Interfacial Polymer Layer by Exploring the Dispersion States of Nanocomposites. *ACS Appl Mater Interfaces* **2019**, *11* (19), 17863-17872.